The Distribution of Star Formation in the SAMI Galaxy Survey: The Implications for Quenching Mechanisms and Galaxy Evolution

By

Gregory Goldstein

A thesis submitted to Macquarie University
for the degree of Doctor of Philosophy
Department of Physics and Astronomy
January 2021

MACQUARIE
University
SYDNEY · AUSTRALIA

Typeset in $\LaTeX\,2_\varepsilon$.

STATEMENT OF CANDIDATURE

This thesis is my own work. The thesis is submitted in fulfilment of the requirements of the Degree of Doctor of Philosophy at Macquarie University. Except where acknowledged in the customary manner, the material presented in this thesis is, to the best of my knowledge, original and has not been submitted in whole or part for a degree in any university.

Gregory Goldstein

Contents

Contents v

ABSTRACT ix

1 INTRODUCTION 1

1.1 Galaxy Evolution . . . 2

1.1.1 The Early Universe . . . 3

1.1.2 Peak Star Formation . . . 7

1.1.3 The Local Universe . . . 9

1.1.4 Inside-Out Growth and Quenching of Galaxies . . . 11

1.1.5 Bimodality . . . 13

1.1.6 The Star Formation Main Sequence . . . 14

1.1.7 Confinement of Star-forming Galaxies into a Main Sequence: The Compaction Model . . . 17

1.2 Quenching Mechanisms and Models . . . 18

1.2.1 Compaction Model and Quenching . . . 19

1.2.2 Bar-driven Quenching . . . 19

1.2.3 Bulge Growth and Morphological Quenching . . . 21

1.2.4 Strangulation . . . 23

1.2.5 The Role of the Cosmic Web in Star Formation and Quenching . . . 24

1.2.6 The Cosmic Web Detachment model of Quenching . . . 27

1.2.7 Halo Quenching . . . 29

1.2.8 AGN Feedback . . . 30

1.2.9 AGN Feedback that triggers SF . . . 32

1.2.10 Galaxy Environment and Quenching . . . 34

1.3 Addressing Quenching via Integral Field Spectroscopy . . . 36

1.3.1 The SAMI Galaxy Survey: Introduction . . . 37

1.4 Questions Addressed in This Thesis 39
1.4.1 Layout of the Thesis 40

2 METHODS AND DERIVED QUANTITIES 41
2.1 Introduction 41
2.2 SAMI Survey Sample Selection 42
2.3 Measuring Emission Line Fluxes 43
2.4 Adaptive Binning 44
2.5 Calculation of Star Formation Rate and Dust Corrections 45
2.6 Photometric Properties 46
2.6.1 Galaxy Stellar Mass 46
2.6.2 Bulge-disk decompositions 47
2.6.3 Environmental Surface Density 48
2.6.4 Galaxy Color and Sérsic *n* 49
2.7 Galaxy Classification as SF, AGN/LINER and AGN_Composite 49
2.8 Statistical Tests 51
2.8.1 Spearman Correlation 51
2.8.2 Kolmogorov-Smirnov Test 51

3 SAMPLE DEFINITION AND GLOBAL PROPERTIES 53
3.1 Introduction 53
3.2 Star-Forming Galaxy Sample Selection 53
3.3 Defining the Star Formation Main Sequence 54
3.4 Defining Groups of Galaxies Around the SFR Main Sequence 57
3.5 Global Properties of Galaxies in Groups 58
3.5.1 Visual Morphology 59
3.5.2 $g - i$ Color 60
3.5.3 Sérsic Index 60
3.5.4 Bulge-to-total Flux Ratio 61
3.5.5 Environmental Surface Density (ESD) 62
3.6 Galaxy Characteristics: Discussion and Conclusions 64

4 Radial Profiles of Star Formation Surface Density 67
4.1 Introduction 67
4.2 Constructing Radial Profiles 68

4.3 Radial Profiles of Above-MS, MS and Below-MS groups in 3 mass subgroups 73
4.4 Measurement of Slope Values of Profiles in Galaxy Groups 75
4.4.1 Errors on Slope Measurement 78
4.4.2 Slope Values of Radial Profiles in Galaxy Groups 80
4.4.3 Slope of Profiles over 0.5 - 1.5 R_e 83
4.4.4 Galaxies with Central Suppression 85
4.5 Properties of Galaxies with Rising or Falling Central Slope Values 86
4.6 Summary and Discussion 92

5 DISCUSSION AND CONCLUSIONS 95

5.1 Does star formation vary coherently within galaxies across the SFR-Mass plane? 95
5.2 Rising radial profile of star formation surface density over 0-0.5R_e 97
5.3 Bulge-to-total Flux Ratio 100
5.4 Environmental Surface Density 102
5.5 Hα as a Star Formation Indicator in AGN/LINERS 103
5.6 Conclusions and Future Work 106
5.6.1 Future Work 107

6 REFERENCES 109

7 APPENDIX 119

7.1 PUBLICATIONS IN ASTROPHYSICS 119

ABSTRACT

The distribution of the star formation across galaxy disks is examined with integral field spectroscopy to determine if the distribution varies according to the so-called 'main sequence' locus of galaxies on the plane of integrated star-formation rate and galaxy mass. Integral field spectroscopy allows the construction of radial profiles of star formation in the disks of star forming galaxies. The profiles are here used in the testing of various mechanisms that have been proposed for galaxy quenching and evolution. A goal is to determine whether processes local to each galaxy (such as a central process) or global environmental factors such as strangulation are the prime drivers of quenching. A sample of star forming galaxies from the SAMI Galaxy Survey is used, noting that only galaxies with a majority of spaxels in the central area that are star forming are suitable for construction of a radial profile. Galaxies have been classified as main sequence, above-, and below-main sequence based on their location in relation to the star formation main sequence ridgeline.

The radial profiles of star formation indicate that central suppression of star formation occurs in 16-20 percent of galaxies on, above or below the main sequence. The radial profiles are generally consistent with coherent star formation, whereby whatever the quenching process is that drives reduced SFR, it acts in such a way that SF remains largely coherent across the galaxy body. Coherent star formation favors several proposed quenching mechanisms including strangulation or cosmic web detachment. Central suppression is not a signature of a quenching process, but is consistent with a central process such as the compaction scenario, and cyclic central star formation. This study has been unable to distinguish between quenching from the inside out such as the 'compaction' scenario, and strangulation as a primary quenching mechanism. A weak positive correlation between bulge size and central SF radial profile slope has been detected, however the results do not support a major role of bulges in the initiation of central suppression of star formation.

Chapter 1

INTRODUCTION

The main themes addressed in this introduction are the star formation (SF) distribution in galaxies - the study of which has become greatly enhanced through integral field spectroscopy - and what the distribution indicates in relation to galaxy evolution. The thesis attempts to examine whether the SF distribution may vary according to the roles of different quenching mechanisms such as stellar feedback, bulge growth or galaxy strangulation.

Many quenching mechanisms act Locally on a galaxy, for examples: SF may be suppressed at the galaxy centre (inside-out quenching) by bulge growth (Mosleh et al. 2017), morphological quenching (Martig et al. 2013), and active galactic nuclei feedback (Taylor & Kobayashi 2017); while in dense environments mechanisms such as ram pressure stripping may act on the galaxy periphery (Schaefer et al. 2017, 2019; Finn et al. 2018; Medling et al. 2018), causing outside-in quenching. It is suggested that both inside-out and outside-in quenching may co-exist in different environments (Lin et al. 2019). AGN feedback may Locally suppress SF at the galaxy centre, and also create galaxy outflows that enhance SF at the periphery (Zubovas & King, 2016). Other proposed quenching mechanisms may act in a galaxy-wide manner, for example strangulation (Peng et al. 2015) or cosmic web detachment (Aragon-Calvi et al. 2019). An examination of SF distribution as galaxies quench and move off the star formation main sequence can reveal changing star formation rates (SFRs) in different parts of the galaxy, thereby favoring one or other quenching mechanism.

This chapter provides a review of background context to the study of galaxy evolution, and the role of galaxy star formation properties as a key indicator of the physical processes at work. The SAMI (Sydney- AAO Multi-object Integral field spectrograph) galaxy survey is also introduced, and the key questions of the thesis are presented.

1.1 Galaxy Evolution

This section reviews how galaxies change over cosmic time, addressed in discussions of the early Universe, peak star formation, and the Local Universe, using the ΛCDM cosmological model. SAMI galaxies lie in the Local Universe within the redshift range z = 0.004 - 0.095, however I briefly discuss recent advances in knowledge from the early Universe and peak star formation epochs as theories of evolution and quenching have been influenced strongly by observations of these epochs. Key properties of galaxies established from observations are the existence of a star formation main sequence, bimodality, inside-out growth of galaxies, mass scaling relations, and in some cases inside-out quenching. Bimodality refers to a split of galaxies into star-forming and quiescent populations based on the bimodality observed in their colours and derived SFRs (Brennan et al. 2017). Evolutionary theories that account for these observational findings are discussed in more detail.

The ΛCDM model is generally considered the 'standard model' of cosmology (Weinberg et al. 2015), and the dominant structure-formation model. It may be argued all galaxy studies address galaxy evolution and consider and test the hierarchical CDM model in various ways. In support of this assertion here are some goals of 2 recent galaxy surveys, the GAMA (Driver et al. 2009) and SAMI (Croom et al. 2012) galaxy surveys.

The recent GAMA galaxy survey was specifically designed to test the CDM model in three ways (Driver et al. 2009): to measure the dark matter (DM) halo mass function by estimating halo mass from the relative orbital velocities of the galaxies in the group; to measure the baryonic systematics of galaxy formation such as the global galaxy stellar mass function, star-formation efficiency and feedback; and to infer the galaxy merger rates over 5 Gyr via the observed number of close pairs and via structurally asymmetric systems.

In the SAMI Galaxy Survey, the science goals discussed in Croom et al. (2012) include understanding how did the galaxy population observed today come about; galaxy properties such as bimodality and morphology; and physical processes that occur as galaxies form and evolve, including the build up of angular momentum, stellar feedback and the distribution of star formation.

1.1.1 The Early Universe

The cosmic microwave background radiation (Gawiser & Silk 2000) reveals the Universe when it was only about 400,000 years old following the so-called 'Big Bang', and helps confirm theoretical ideas about the ubiquitous presence of dark matter (DM) and cosmic inflation (Springel et al. 2006). In cosmic inflation the Universe grows exponentially for many doubling times perhaps $\sim 10^{-35}$ seconds after the Big Bang, and quantum fluctuations in this 'inflation' field are blown up to macroscopic scales and converted into ripples in the cosmic energy density (Guth 1981, Springel et al. 2006). Initial weak seed fluctuations grow via gravitational instability, with dark matter collapsing into clumps or 'haloes' and undergoing hierarchical aggregation into ever more massive systems (Cattaneo et al. 2009). Galaxies form at the centres of these dark matter haloes by the cooling and condensation of gas which fragments into stars once it becomes sufficiently dense (White & Rees 1978, Cattaneo et al. 2009).

During the first few billion years after the Big Bang there was the formation of the first stars, the rapid formation of galaxy stellar populations, the reionization of the predominantly neutral intergalactic medium, the production and dissemination of heavy elements, and the formation of the first black holes (Papovich et al. 2019). The birth and adolescent phases of galaxies can be investigated through the astrophysical properties of their massive stars because their light dominates the direct rest-frame UV continuum($\sim$ 1500 Å) from their photospheres, the nebular continuum and emission lines from HII regions they ionize, the rest optical/near-IR (0.4-2μm) emission from their post-main sequence supergiants, and their far-IR ($\sim$100μm) reradiated emission from dust (Papovich et al. 2019).

Protons, electrons and neutrons compose gas and stars and are generally considered to interact with DM purely through gravity, which determines the evolution of the Universe on large scales (Cattaneo et al. 2009). A filamentary network- the cosmic web - is created as groups and clusters of galaxies aggregate into larger systems. The cosmic web is composed of geometrically distinct components termed voids, sheets, filaments, and knots, and is the most striking manifestation of gravitational collapse on the scales of a few megaparsecs and above (Bond, Kofman & Pogosyan 1996, Metuki et al. 2015). On the sub-megaparsec scale, DM collapses into virialized structures called haloes. DM may act as a site of galaxy formation if a DM halo's potential well is deep enough, enabling the efficient cooling of gas (Figure 1.1) and the formation of stars. Structure in ΛCDM cosmology forms from the bottom up - the first objects to appear at high redshift condense out of small perturbations in the initial density field to form small sub-galactic units (Figure 1.1). The pervasive presence of DM is supported by compelling evidence including galactic rotation curves, the structure of galaxy groups and clusters, large-scale cosmic flows and gravitational lensing whereby the distorted images of background galaxies as their light travels near mass concentrations reveal the presence of DM in the outer haloes of galaxies and in galaxy clusters (Springel et al. 2006).

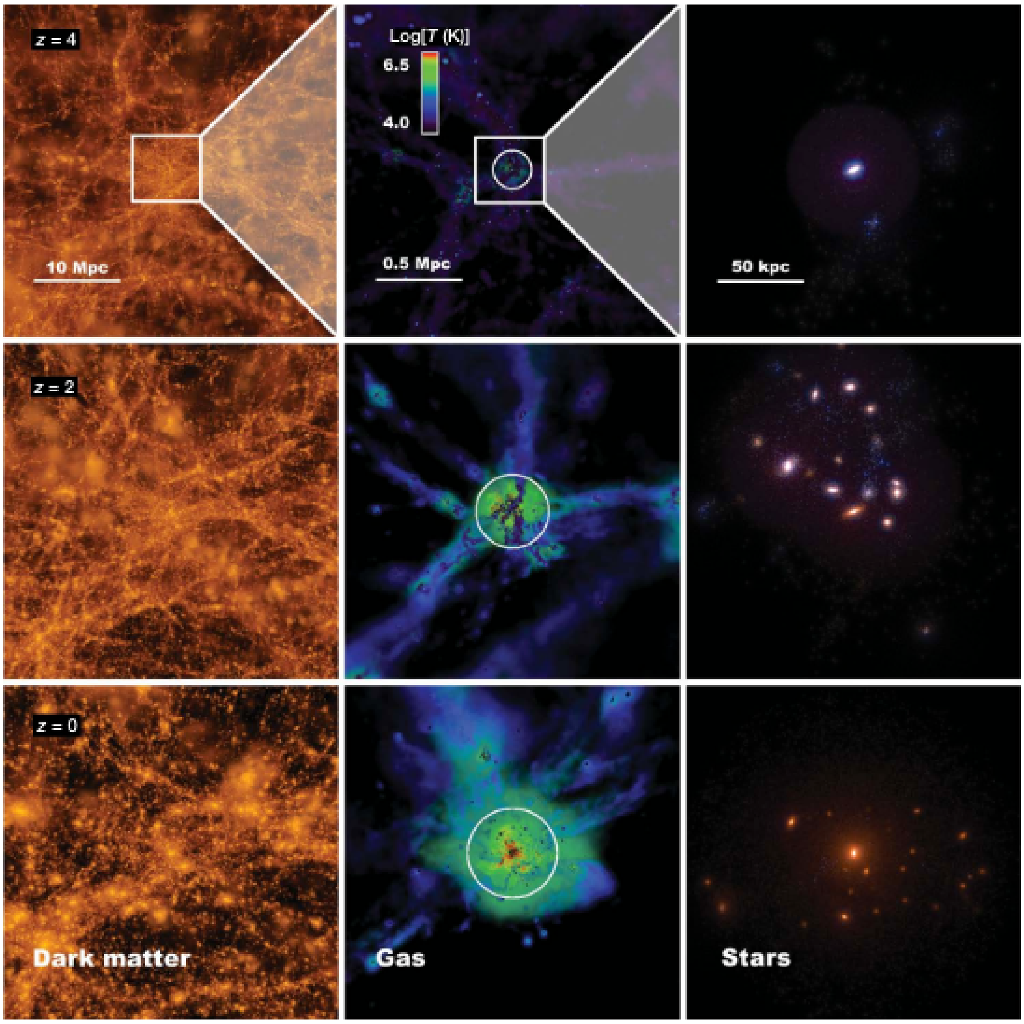

Figure 1.1: *The cosmic web, and galaxy evolution taken from Cattaneo et al. 2009. The figure illustrates the formation of an elliptical galaxy, showing the dark matter (Column 1), the gas (Column 2) and the stars (Column 3) at three epochs in the expansion of the Universe, at 1/5 of its current size (redshift $z = 4$), at 1/3 of its current size ($z = 2$), and today ($z = 0$). The gravity of the dark matter dominates the evolution on large scales (Column 1). Over time the Universe becomes lumpier as the dark matter clumps into haloes (bright orange spots in Column 1). Column 2 zooms into the region around and inside a halo to display the gas. The halo radius is shown as a white circle, and the gas is colour-coded to show its temperature: blue is cold, green (and red) is hot. At z=4 the halo is small, and the gas streams into the halo down to its centre in cold flows. When the halo reaches the critical mass $M_{crit} < 10^{12} M_{\odot}$ ($z = 2$), the gas begins to form a hot atmosphere (green); eventually, all the gas within the halo is hot ($z = 0$). Column 3 zooms in further to show the visible galaxy formed by the gas fallen to the centre. At z=4 the galaxy is a blue spiral. The galaxy reddens when the halo gas heats up ($z = 2$), and its halo has merged with neighbouring haloes to form a galaxy group. Mergers with companions eventually transform the galaxy into an elliptical ($z = 0$).*

Some of the strongest observational evidence supporting the hydrodynamical simulation predictions of large-scale structure formation comes from the statistics of absorption lines evident in the spectra of distant quasars (Fig 1.2, from Springel et al. 2006). There is a forest of absorption lines of differing strength that arise from Lyman α absorption by the smoothly varying distribution of foreground intergalactic neutral hydrogen along the line of sight, in effect from the filaments, sheets and haloes of cosmic structure as displayed in Figure 1.2.

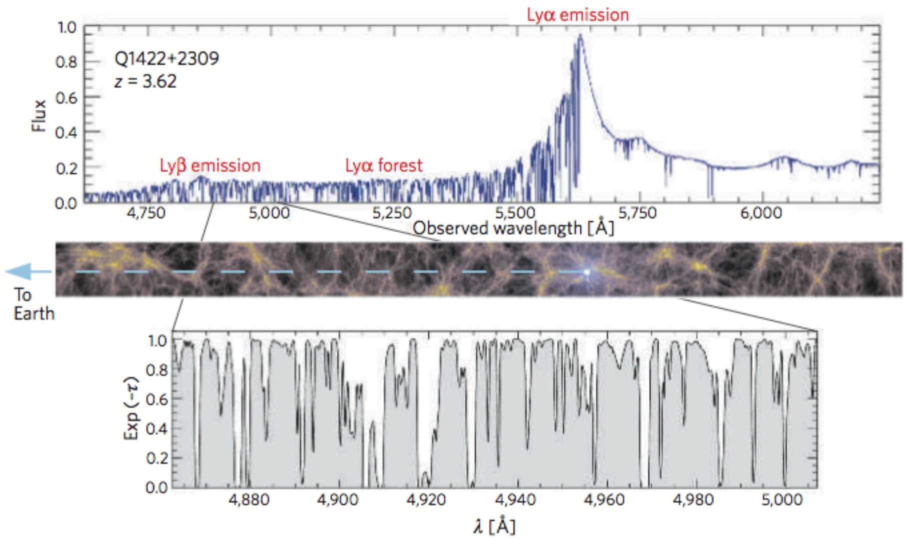

Figure 1.2: *An example of the Lyman α forest taken from Springel et al. (2006). The spectrum of the quasar Q1422+2309 at z=3.62 shows a forest of absorption lines of different strength produced by intervening neutral hydrogen gas along the line-of-sight from the quasar. The Lyman α forest constitutes a strong confirmation of the CDM paradigm, when hydrodynamical simulations produce filaments, sheets and haloes of cosmic structure that explain the absorption lines seen in the spectra of distant quasars.*

The cosmic web evolves with time, becoming more defined as the Universe evolves, via gravitational collapse. This large-scale evolution can also significantly influence the galaxies which form and live within those haloes and certain galaxy properties (such as luminosity, colour, morphology, etc.) correlate with the mass of their host halo (Metuki et al. 2015).

Overall, the ΛCDM theory has so far been very successful in describing the Universe and its evolution on a variety of scales. The associated parameters describing the key components, e.g. Ω_M (total matter density, comprising the combination of Ω_B and Ω_{DM}, representing baryons and dark matter, respectively), Ω_Λ (dark energy density), and H_0 (the Hubble constant), have been determined from a large variety of independent studies using orthogonal observational indicators over the past several decades, and show remarkable agreement (Croton et al. 2006, Springel et al. 2006). However, some important discrepancies remain (e.g. small-scale mass clustering, Chang et al. 2019), and tension between Local and cosmic microwave background (CMB) determinations of the Hubble constant (Reiss et al. 2016, Planck+18 (Aghanim et al. 2018)), motivating future observational projects like the Large Synoptic Survey Telescope (Ivezic et al. 2019), Euclid (Knabenhans et al. 2019), and WFIRST (Akeson et al. 2019).

1.1.2 Peak Star Formation

One key metric for quantifying how galaxies change over time is measuring the rate at which they form stars. The star formation rate (SFR) can be estimated through a variety of observational indicators, usually chosen for observational reasons depending on e.g. the redshift range being studied. A large number of systematic studies have consistently shown that there has been a rise and fall in cosmic star formation rate from high redshifts to the present time with a peak between 1< z <3 (Madau & Dickinson 2014). To identify peak star formation, studies in ultraviolet (UV) are of particular value as UV light is a tracer of recent star formation in galaxies, and the UV luminosity function can help determine the total star formation rate density at all epochs using current telescopes (Alavi et al. 2016).

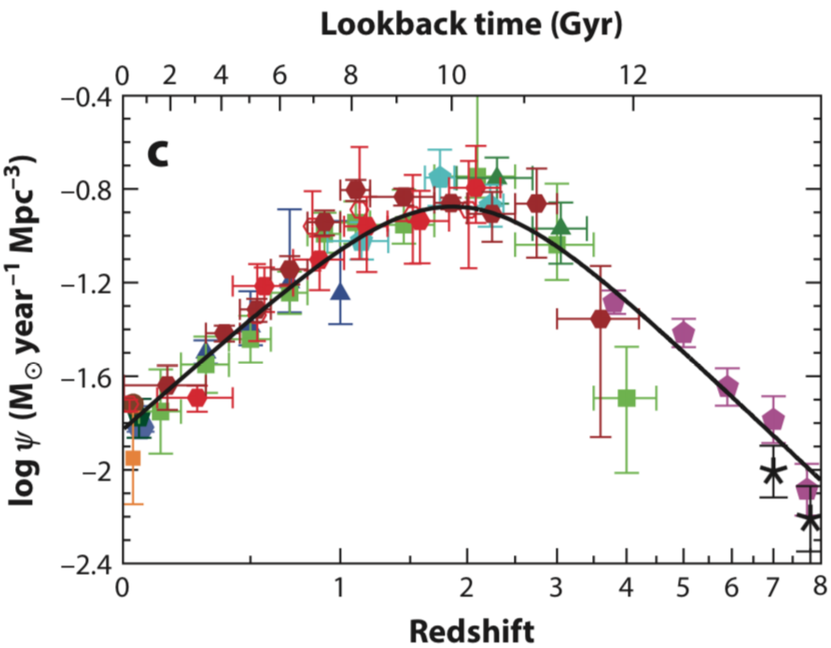

Figure 1.3: *Madau and Dickinson 2014. The history of cosmic star formation from FUV+IR rest-frame measurements. The solid curve plots the best-fit SFR density*

Figure 1.3 displays a rising phase of star formation rate density, scaling as $\psi(z) \propto (1+z)^{-2.9}$ at $3 \leq z \leq 8$, slowing and peaking at some point probably between z = 2 and 1.5, when the Universe was ~3.5 Gyr old, followed by a gradual decline to the present day, roughly as $\psi(z) \propto (1+z)^{2.7}$ (Madau & Dickinson 2014). Half of the stellar mass observed today was formed before a redshift z = 1.3. About 25% formed before the peak of the cosmic star-formation rate density, and another 25% formed after z = 0.7 that represents the last half of the Universe's age. Less than ∼1% of today's stars formed during the epoch of reionization, which ended around 1 billion years after the Big Bang, corresponding to a redshift of about 6.5.

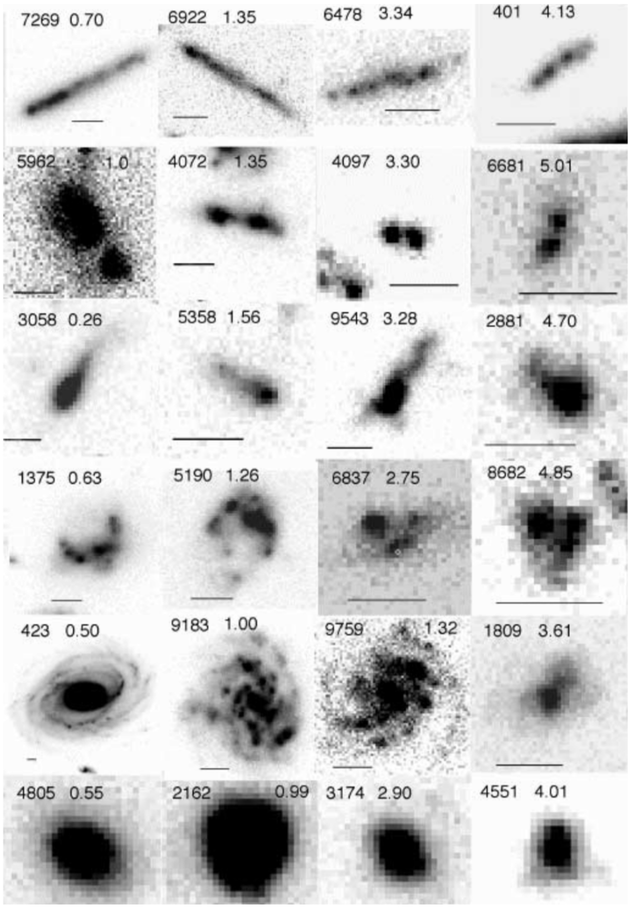

Figure 1.4: *Galaxy Morphology in Peak Star Formation, from Elmegreen et al. (2007). Examples of galaxies at z=1 and higher are observed with the Advanced Camera for Surveys (ACS) on the Hubble Space Telescope. There are morphologies that are non-existent or rare in the Local Universe: chains (row 1), doubles (row 2), tadpoles (row 3), and clump clusters (row 4). Also there are spirals (row 5) and ellipticals (row 6) that are common in the Local Universe. The Hubble Ultra Deep Field Catalog (UDF) number is in the top left of each image, along with the redshift, which increases from left to right.*

In the era of peak star formation (sometimes referred to as 'Cosmic High Noon') galaxies not only formed stars at a much greater rate, they displayed different galaxy morphologies. Elmegreen et al. (2007) find high-redshift galaxies typically include peculiar clumpy types that are not found Locally, as shown in Figure 1.4. Thus, the Hubble class and other standard systems have limited value at high redshift. Galaxies observed with the Advanced Camera for Surveys (ACS) on the Hubble Space Telescope become increasingly clumpy and irregular beyond redshift z = 1, partly because star-forming regions get intrinsically more massive at higher redshifts, partly because of bandshifting of UV-bright regions into the optical bands, and partly because of an increased importance of galaxy interactions in the young Universe (Elmegreen et al. 2007). Clumpy star forming regions are present in all galaxy types, including ellipticals. The most irregular systems are clump clusters, which are oval collections of bright clumps, and chain galaxies which are linear alignments of bright clumps. The distribution of the ratio of axes among clump cluster and chain galaxies suggests that the chains are edge-on clump clusters (Elmegreen et al. 2007).

1.1.3 The Local Universe

Large, systematic studies of galaxies spanning the epoch from the "Cosmic High Noon" to today have allowed the star forming galaxy population to be considered as a function of mass at different epochs. They have further shown that there is a tight locus of galaxies on the SFR-Stellar Mass plane that dominate the population. This locus is termed the SFR main sequence (Noeske et al. 2007, Renzini & Peng 2015). Delgado et al. (2016) report the tight correlation between the galaxy stellar mass (M_*) and the SFR for galaxies in the blue cloud defined by a color-magnitude diagram, with only 0.2 - 0.3 dex dispersion in star formation rate for a fixed stellar mass (M_*). Between $0 < z < 2$ most star-forming galaxies follow a tight relation between SFR and M_*. The reduction in integrated SFR in that period happens to galaxies of all masses. The average SFR at fixed stellar mass has decreased at a steady rate by a factor of $\sim$ 20 from z $\sim$ 2 to z =0 (Speagle et al. 2014). There is a strong evolution in the normalization of the main sequence with redshift whereby the normalization (e.g., the mean SFR at some fiducial mass) decreases steadily with cosmic time or decreasing redshift at least from z = 2 to the present (Noeske et al. 2007; Madau & Dickinson 2014; Tacchella et al. 2016).

High/low redshift comparisons show the number of red galaxies has at least doubled since z $\sim$ 1 while the number of blue galaxies has remained relatively constant (Faber et al. 2007; Cheung et al. 2012). The finding implies galaxies evolve from blue to red with time, i.e., from star forming to ‘quenched’ (Cheung et al. 2012; Pan et al. 2013; Brennan et al. 2017). The evolution is reflected in the near-constant stellar mass contained in objects in the blue cloud, while there is increasing stellar mass represented by galaxies on the red sequence (Brennan et al. 2015). There is evidence the transition from blue to red is rapid, ~1 Gyr (Bell et al. 2004; Blanton 2006).

Over cosmic time the fraction of star-forming discs declines steadily, while the fraction of quiescent spheroids increases (Bell et al. 2012; Tomczak et al. 2014; Brennan et al. 2015). Brennan et al. (2015) use color bimodality as a tracer of galaxy evolution since z ~3 to study the evolution with redshift of the quiescent and spheroid-dominated fractions of galaxies from the CANDELS (Cosmic Assembly Near-infrared Deep Extragalactic Legacy Survey) and GAMA (Galaxy and Mass Assembly) surveys (Figure 1.5). In this figure evolution is demonstrated by dividing galaxies into four sub-populations, star-forming discs (SFD), quiescent spheroids (QS), and also quiescent discs (QD) and star-forming spheroids (SFS). Tomczak et al. (2014) observe a rapid build-up at the low-mass end of the quiescent stellar mass function since z = 2.5, whereby the total stellar mass density of quiescent galaxies increases by a factor of ~12, whereas the mass density of star-forming galaxies only increases by a factor of ~2.2. This is consistent with blue disk to quiescent spheroid evolution. Bell et al. (2012) also note the dramatic increase from z = 2.2 to the present day in the number density of non-star-forming galaxies above $3 \times 10^{10} M_{\odot}$.

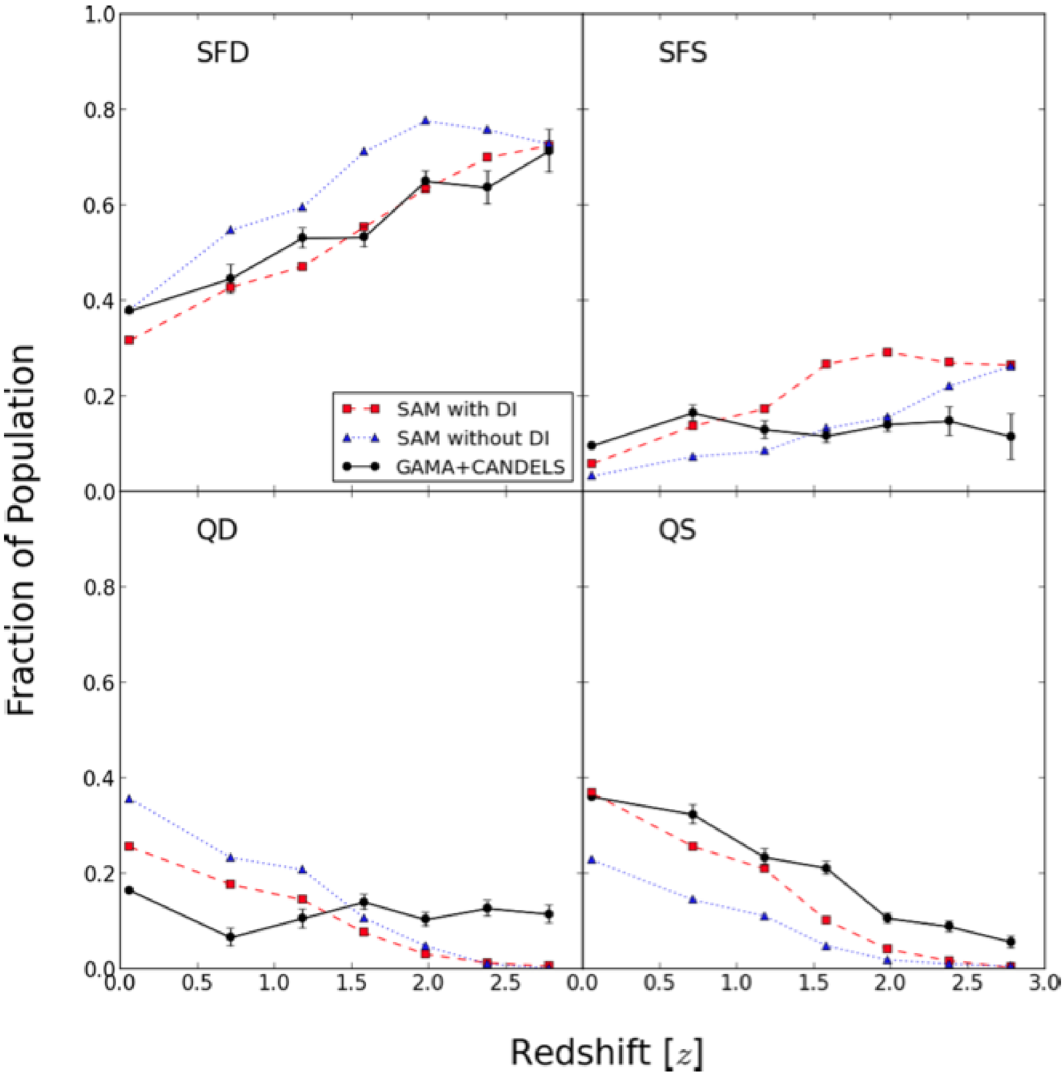

Figure 1.5: *Galaxy evolution from Brennan et al. (2015). The 4 panels track from z=3 to z=0 star-forming discs (SFD), quiescent spheroids (QS), and also quiescent discs (QD) and star-forming spheroids (SFS). The observations (solid black line) are compared to 2 semi-analytic models (SAMs), with and without a disk instability (DI) correction). Analysis of the build-up of stellar populations from high redshift to the present reveals that the stellar mass contained in objects in the blue cloud has remained relatively constant, while the stellar mass represented by galaxies on the red sequence has grown significantly; this implies that blue star-forming galaxies are in fact being transformed into red, quiescent ones.*

1.1.4 Inside-Out Growth and Quenching of Galaxies

In the ΛCDM paradigm of hierarchical galaxy formation, galaxies naturally grow and accrete material over time, making them become generally larger and more massive as the Universe evolves (White & Frenk 1991). This general picture is confirmed by observations (e.g. evolution of the mass function - Tomczak et al. 2014; size evolution - van der Wel et al. 2014), and can be thought of as an 'inside-out' progression of galaxy evolution.

The details of how the stellar mass is distributed within a given galaxy relates to the interplay of hierarchical growth and the detailed baryonic physics. Support for the idea of an inside-out progression of galaxy growth comes from stellar metallicity gradients. Chemical elements may be considered fossils in galactic archaeology, on which the star formation and chemical enrichment histories are imprinted (e.g. Nomoto, Kobayashi & Tominaga 2013, Taylor & Kobayashi (2017). Galaxy centres are typically older and more chemically evolved than their outer parts, in line with building mass at larger radii at later times. Metallicity gradients may provide one of the most stringent constraints on star formation history; for disc galaxies, the radial gradients suggest the inside-out growth (Kobayashi & Nakasato 2011).

Taking star formation as an indicator of where stellar mass is increasing in a galaxy can give insight into this process. For example, Tacchella et al. (2015) note that most present day galaxies with stellar masses $\geq 10^{11}\ M_{\odot}$ show no ongoing star formation; yet ten billion years ago similarly massive galaxies with high central stellar mass densities and bulges typically formed stars at rates of 100 $M_{\odot}$ per year. Tachella et al. (2018) build on this by looking at the ratio of star formation rate to existing stellar mass as a function of galactocentric radius, termed the specific star formation rate (sSFR). They find that their sample of $z \sim 2$ galaxies show a central down-turn in sSFR at high masses, which they interpret as 'inside-out quenching' (i.e. implying a direct connection between the existing stellar mass and the reduced near-instantaneous SFR). Similar trends are seen in the current-day Universe (Belfiore et al. 2018).

While centrally lower sSFR certainly indicates a reduced SFR relative to the existing stellar mass, it does not directly indicate how or when the central stellar mass was assembled (e.g. through a continuous suppression of SFR, through central migration of stellar mass, or from a disconnected earlier formation phase). This leaves the connection to active quenching processes somewhat ambiguous, and for this reason this thesis focuses on absolute SFR, rather than the ratio with the Local integrated stellar mass. There are several reasons to consider a centrally operating mechanism that does, however, centrally suppress the SFR in both absolute and relative terms, and these are more fully considered in Section 1.2.

1.1.5 Bimodality

For many years astronomical observations and galaxy surveys have reported there are 2 main types of galaxies: blue star-forming galaxies with spiral arms and discs, that are found in lower-density environments, and more massive red and 'dead' ellipticals most often found in galaxy clusters ((Hubble 1926; Gabor et al. 2010; Taylor et al. 2015). This is also known as the morphology-density relation (see e.g. Dressler 1980). Blue star-forming galaxies mostly have stellar masses below $\sim 10^{10.5} M_{\odot}$ and red galaxies mostly have higher stellar masses (Kauffmann et al. 2003a; Cattaneo et al. 2009). Blue galaxies create stars at a high rate while red galaxies show little to no star formation (Salim et al. 2005, 2007; Noeske et al. 2007). Taylor et al. (2015) note the elliptical 'early type' galaxies are older, redder, less likely to be star forming, and smaller than the 'late type' spirals of the same mass; how the properties of a galaxy scale with mass is different for the early- and late-type populations. Bimodality appears to be in place even at high redshift (Ilbert et al. 2010; Brammer et al. 2011, Pontzen et al. 2017). The star-forming/quiescent bimodality is observed out to z=3 (Brennan et al. 2015); other authors report the SFR-M_* correlation is present out to z $\sim$ 6 and holds over at least four orders of magnitude in mass (Speagle et al. 2014; Salmon et al. 2015).

Comparing galaxies at high redshifts to the Local Universe, the number of red galaxies has at least doubled since z $\sim$ 1 while the number of blue galaxies has remained relatively constant (Cheung et al. 2012; Faber et al. 2007). The finding implies galaxies evolve from blue to red with time, i.e., from star forming to quenched (Cheung et al. 2012; Pan et al. 2013; Brennan et al. 2017). The red quiescent galaxies lie on a relatively narrow ridge called the red sequence in the color-magnitude diagram and are comprised of mainly early-type galaxies. The blue galaxies, are distributed throughout the blue cloud and are mainly disk or late-type galaxies.

Dekel & Birnboim (2006) propose a theory of bimodality driven by the thermal properties of the inflowing gas in galaxies, that involves the clustering and feedback processes which are functions of the dark matter halo mass. In haloes below a critical shock-heating mass $M_{shock} \leq 10^{12} M_{\odot}$, discs are built by cold streams, not heated by a virial shock, yielding efficient early star formation. Cold streams penetrating through hot media in $M \geq M_{shock}$ haloes preferentially at $z \geq 2$ lead to massive starbursts in $L > L_*$ galaxies, where L_* is the characteristic luminosity of the brightest disc galaxies. At $z < 2$, in $M > M_{shock}$ haloes that host galaxy groups, the gas is heated by a virial shock, and feedback from energetic sources such as AGN shuts off gas supply and prevents further star formation, resulting in passive evolution to 'red-and-dead' massive spheroids starting at z ~ 1.

The concept of color bimodality is challenged by a third population of galaxies that lie in the 'green valley' between the blue cloud and the red sequence. Green valley galaxies are considered to be a transitioning population migrating from the blue cloud towards the red sequence (Salim et al. 2007; Wyder et al. 2007; Pan et al. 2013) and as such may provide key insights into causes and processes associated with the blue to red evolutionary transition. As well as the term green valley, the abbreviation 'quenching-in-progress' is used for a transitioning population.

Methods used to define a green valley galaxy include dust-corrected NUV-r where NUV and r are the magnitudes in the near-ultraviolet and r band; typical green valley values have 4<NUV-r<5 (Salim et al. 2007; Wyder et al. 2007; Pan et al. 2013; Cheung et al. 2016). Green valley galaxies occupy the region in between the blue cloud and the red sequence on the colour–magnitude diagram (Renzini & Peng 2015; Brennan et al. 2017).

Evidence suggests the transition from blue to red is rapid, ~ 1 Gyr (Bell et al. 2004; Blanton 2006; Gabor et al. 2010), implied by the relative scarcity of galaxies in the green valley compared to the blue cloud or red sequence. Mendez et al. (2011) argue the observed bimodality requires a short timescale for movement to the red sequence after quenching of star formation on the order of ~ 1 Gyr, and that if quenching caused the residual star formation to decline slowly over say 14 Gyr, the remnant would gradually transition to the red sequence, removing any distinct green valley between the red and blue galaxy populations. Schawinski et al. (2014) find indications of two distinct paths through the green valley, one taken by galaxies that leave the blue cloud as disc-dominated systems (slow path) and the other by galaxies that transition as bulge-dominated systems (fast path).

1.1.6 The Star Formation Main Sequence

The stellar mass and star formation rate (SFR) of galaxies are so closely correlated that following Noeske et al. (2007) the correlation is designated as the star formation main sequence (MS) (Renzini & Peng 2015). Delgado et al. (2016) describe the tight correlation between the galaxy stellar mass (M_*) and the SFR for galaxies in the blue cloud, with only

0.2 - 0.3 dex dispersion in SFR for fixed M_*. At $0 < z < 2$ most star-forming galaxies follow a tight relation between SFR and M_*; there is a strong evolution in the normalization of the MS with redshift whereby the normalization (e.g., the mean sSFR at some fiducial mass) decreases steadily with cosmic time or decreasing redshift at least from z = 2 to the present (Noeske et al. 2007; Madau & Dickinson 2014; Tacchella et al. 2016). Most studies find that the average SFR is a mildly declining function of stellar mass; the MS slope below unity signifies that the specific SFR declines weakly with increasing stellar mass (Delgado et al. 2016). This implies that more massive galaxies completed the bulk of their star formation earlier than lower-mass galaxies (Madau & Dickinson 2014).

The slope, shape, dispersion, and redshift evolution of the SFR-M_* correlation can vary quite dramatically from one study to another, with the logarithmic slope of the relation ranging from ~0.4 up to ~1 (Renzini & Peng 2015). To address this variation, and to better identify quenching galaxies, Renzini & Peng (2015) develop a MS based on a 3D SFR-mass-number plot where the third-dimension gives the number of galaxies in fixed-size (0.2×0.2 dex) SFR-M_* bins. The plot uses galaxies from the Sloan Digital Sky Survey (SDSS) DR7 release (Abazajian et al. 2009), and excludes AGNs. The plot features two peaks that correspond to actively SF galaxies on one side and quenched galaxies on the other side, with a sharp divide in between (Figure 1.6).

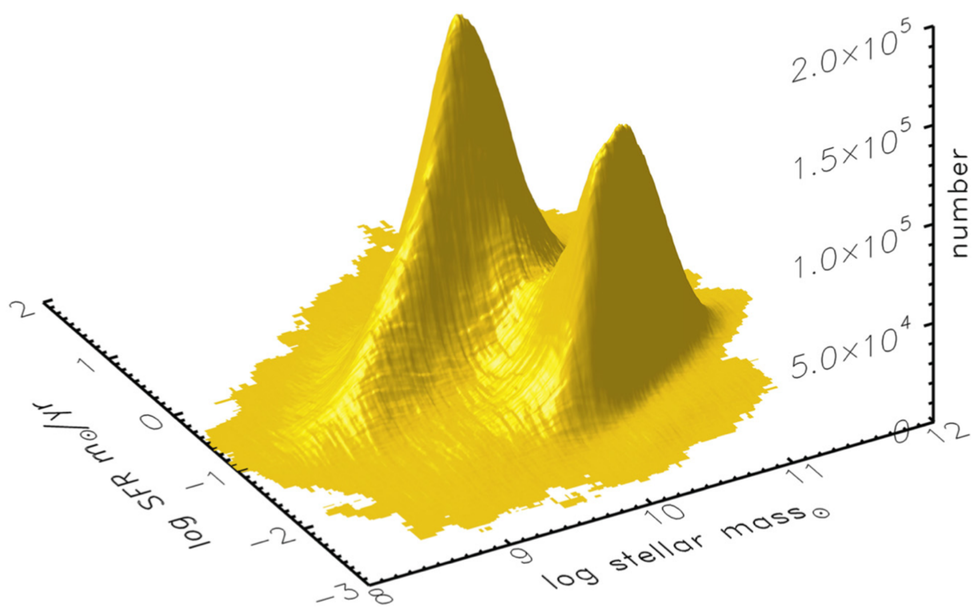

Figure 1.6: *SFMS (source: Renzini & Peng 2015). A 3D view of the SFR-M_* relation for Local galaxies in the SDSS database and $0.02 < z < 0.085$. The third-dimension is the number of galaxies in the SFR-M bins. There are two prominent peaks, one for star-forming galaxies and one for quenched ones. The SF peak has a sharp ridge line with a steep fall off in the number of galaxies on either side of the ridge line. The ridge is used as the definition of the main sequence of star-forming galaxies.*

Renzini & Peng (2015) claim the variation in the MS in results from various authors is due to a pre-selection of SF galaxies, for examples using galaxy color to distinguish SF and non-SF galaxies, or setting a minimum threshold for specific SFR. They report the best straight-line fit to the ridge line (MS of star forming galaxies) is:

$$log(SFR) = (0.76 \pm 0.01)log(M_*/M_\odot) - 7.64 \pm 0.02 \tag{1.1}$$

Renzini & Peng (2015) note the ridge line is linear up to the highest stellar masses in the sample, without any flattening with increasing mass. A bending or flattening of the main sequence at the high-mass end reported by other authors could be due to the growing fraction of the total mass being given by already quenched bulges, hence contributing mass but no star formation (Whitaker et al. 2012). Brennan et al. (2017) also interpret the decrease in slope at higher stellar mass as due to the likelihood that higher mass galaxies are already starting to quench. Whitaker et al. (2015) find the slope of the SFR/M_* relation is of order unity for disk-like galaxies, however galaxies with Sersic n > 2 (implying more dominant bulges and more likely to host AGN) have significantly lower SFR/M_* than the main ridgeline of the star formation sequence. They study galaxies at $0.5 < z < 2.5$ selected from the 3D-HST photometric catalogs, and suggest that bulges in massive z ~ 2 galaxies are actively building up, and the stars in the galaxy centre are relatively young. At z < 1, the presence of older bulges within star-forming galaxies lowers global SFR/M_*, decreasing the slope and contributing significantly to the scatter of the star formation sequence.

The MS may be used to determine which galaxies are quenched, which are undergoing quenching, and which are ultraluminous (Renzini & Peng 2015; Brennan et al. 2017); on the SFR-M plot the distance from the MS is used to identify galaxies that do not belong to the MS, whether they are starburst outliers above the MS, or those that have started the quenching process and while still star forming, are below the MS and in transition toward quiescence. Brennan et al. (2017) find strong correlations between the distance from the MS ridge line and galaxy structural properties, and moving from galaxies above the MS to those below it, there is a nearly monotonic trend towards higher median Sersic index, smaller radius, lower SFR density, and higher stellar density. Whitaker et al. (2012) report in galaxies above the MS the spectral energy distributions (SEDs) are dusty but blue, which they interpreted as indicative of AGNs or merger-induced starbursts. Below the MS, the SEDs are not dusty but red, which they interpreted as indicative of star formation being shut down.

An operational definition of active (star-forming) galaxies and passive galaxies is often required in galaxy studies, and usually involves reference to the main sequence of star formation. Lange et al. (2016) in their study of bulge-disk decompositions analyze the stellar mass - half-light radius relations of bulges, discs and spheroids, and separate active and passive galaxies using a specific star-formation rate cut of 0.01 Gyr^{-1} (Furlong et al. 2015), which is approximately one decade below the observed MS. Furlong et al. (2015) study the evolution of galaxy masses and star formation rates in hydrodynamical simulations in a ΛCDM cosmology with the Evolution and Assembly of Galaxies and their Environment (EAGLE) simulations. They find strong agreement between simulation and data across cosmic time and confirm specific star formation rates of simulated galaxies are bimodal, with distinct star forming and passive sequences. They use a sSFR cut 1 dex below the observational data to separate star forming from passive galaxies. Bluck et al. (2014) investigate the origin of galaxy bimodality and define a galaxy to be passive if it is forming stars at a rate a factor of 10 lower than similar stellar mass and redshift galaxies which are actively star forming; they show this metric distinguishes star forming from passive galaxies.

A further example of the use of the MS to study galaxy evolution is Rodighiero et al. (2011) who examine the contribution of starburst galaxies (defined by distance above the MS) to the cosmic SFR density at $z \sim 2$, and conclude starburst galaxies represent only 2% of mass-selected star-forming galaxies and account for only 10% of the cosmic SFR density. These authors argue starburst galaxies are merger driven and represent a phase of transformation of star-forming galaxies into passive ellipticals.

1.1.7 Confinement of Star-forming Galaxies into a Main Sequence: The Compaction Model

Tacchella et al. (2016, 2018) use cosmological simulations to study the evolution of high-redshift star-forming galaxies on, above and below the MS and detect distinct phases of gas compaction, depletion, replenishment, and eventual quenching. The galaxies oscillate about the MS ridge on time-scales of ~1 Gyr at $z \sim 3$. The mechanisms of compaction or build-up of central stellar mass density include mergers, streams of gas arriving from filaments of the cosmic web, or disk instabilities associated with the high gas fraction (Dekel & Burkert 2014; Zolotov et al. 2015; Tacchella et al. 2016) that lead to a high central SFR or central starburst (Ellison et al. 2017).

Gas depletion is triggered by the high central SFR that is associated with stellar/supernova feedback and in some cases active galactic nucleus feedback (Tacchella et al. 2016). With gas depletion comes central (inside-out) quenching quenching (Tacchella et al. 2018), and replenishment from the cosmic web may occur; for galaxies above a threshold halo mass ($M_{vir} > 10^{11.5} M_{\odot}$) there is suppression of fresh gas supply by a hot halo which allows the long- term maintenance of quenching.

The compaction model is supported by simulation studies and observations in galaxies at high redshift (Dekel & Burkert 2014, Nogueira-Cavalcante et al. 2019). Ellison et al. (2018) describe these phases (gas compaction, depletion, replenishment, and eventual quenching) together as the compaction model or scenario and reports that the 4 processes are also observed in the Local Universe. These authors study radial profiles of star formation in MaNGA survey galaxies with IFS, and find galaxies above the main sequence have SFR elevated throughout the galaxy, but the greatest enhancement in star formation occurs at small radii (< 3kpc, or 0.5 R_e). For quiescent/passive galaxies that lie at least a factor of 10 below the star-forming main sequence, there is a deficit of star formation throughout the galaxy, with the lowest values of SFR in the central 3 kpc. The authors argue star formation activity in galaxies is dominated by changes in the central regions, consistent with the compaction model.

The compaction model is consistent with cyclic central star formation whereby intermittent central suppression of star formation occurs in starforming galaxies (Krumholz et al. 2017; Tacchella et al. 2018; Sormani et al. 2019), and is discussed further in the Discussion Chapter, Section 5.2.

1.2 Quenching Mechanisms and Models

'Quenching' is a term commonly used to express star formation coming to an end in a galaxy (e.g. Peng et al. 2010, 2012; Mendel et al. 2013). Quenching is an evolutionary process involving the cessation of star formation in some star-forming galaxies that over time creates the red sequence of passive galaxies, and (after Bluck et al. 2014) quenching involves proposed *mechanisms* that cause the shutting down of star formation. Peng et al. (2010) discuss quenching processes that cause the cessation of star formation in some star-forming galaxies and lead to the emergence of the red sequence of passive galaxies, and state that quenching is distinct from the general decline in the specific star formation rate of star-forming galaxies that has occurred between z $\sim$ 2 and the present, whose cause is not well understood but which may be linked to the dwindling supply of gas onto galaxies. Quenching is assumed to produce passive galaxies with a very low or zero star formation rate; galaxies with intermediate SFRs (between MS and zero) may then be described as quenching-in-progress. In the following subsections, various models and mechanisms that explore these concepts of quenching are discussed in more detail.

1.2.1 Compaction Model and Quenching

The compaction model was described in the previous section 1.1.7 as a mechanism for confining star-forming galaxies into a main sequence. It also models quenching. Galaxies undergo distinct phases of gas compaction, depletion, replenishment, and eventual quenching. Gas depletion is triggered by the high central SFR that is associated with stellar/supernova feedback and in some cases active galactic nucleus feedback (Tacchella et al. 2016; Tacchella et al. 2017). With gas depletion comes central quenching (inside-out quenching), and replenishment from the cosmic web may occur; for galaxies above a threshold halo mass $M_{vir} > 10^{11.5} M_{\odot}$ there is suppression of fresh gas supply by a hot halo which allows the long- term maintenance of quenching.

1.2.2 Bar-driven Quenching

Bars occur in around 30 per cent of massive ($M_{*} \geq 10^{9.5} M_{\odot}$) spiral galaxies in the Local Universe, and are considered to play key roles in the evolution of disc galaxies (Spinoso et al. 2017), including driving inflows of gas towards the centre; triggering nuclear starbursts; development of pseudobulges and boxy/peanut-shaped stellar bulges; triggering of AGN activity; and central quenching associated with gas depletion and outflows. These phases generally mirror the compaction model. Several authors consider bar-driven quenching should be seen as an alternative to the main mechanisms of quenching explored in the literature such as mergers, and AGN feedback (Kormendy 2013; Spinoso et al. 2017). Kormendy (2013) states bars drive secular evolution in galactic disks and notes many barred and oval galaxies have dense central concentrations of gas and star formation as a result of nonaxisymmetries such as bars transporting gas towards the centre.

Gavazzi et al. (2015) note as galaxy stellar mass increases, the specific SFR is constant up to a characteristic stellar mass (M_{knee}), beyond which it decreases steeply with increasing stellar mass; the critical stellar mass M_{knee} in the Local Universe corresponds to $\sim 10^{9.5} M_{\odot}$. They propose that above M_{knee} bars form through disk instability, and initially accelerate SF activity in the circumnuclear region by causing intense gas inflows that effectively trigger bursts of star formation; subsequently bars contribute to quenching the star formation in the longer term within the bar extent (on kpc scales). An enhancement of the central SFR and specific SFR in barred galaxies has recently been reported in the CALIFA study (Catalan-Torrecilla et al. 2017). They present a simple model of isolated disk galaxies in which a developing or existing bar removes in a few dynamical times most of the gas from the central region of the galaxy (i.e., within the bar corotational radius). As a consequence, after a short transient nuclear starburst, the inner region of the galaxy stops forming stars, and grows redder with time. Based on their model simulations and observations, they conclude there is significant central quenching caused by the bars in massive galaxies.

Gavazzi et al. (2015) describe their evolutionary scenario as follows: at a given redshift, galaxies above $M_{\rm knee}$ undergo a 'bar instability' that permits a bar to form. Bar stable and bar unstable galaxies are identified using the Toomre parameter, and also the value of the v_{rot}/σ_* ratio where v_{rot} is the rotational velocity of the disk and σ_* is the stellar velocity dispersion. The developing bar forces the gas within the corotational radius to fall toward the center within a few dynamical times. Central gas at high concentration is immediately consumed by a vigorous burst of star formation (and/or AGN activity), resulting in the formation of a pseudobulge. Observational support for this scenario includes: (a) an AGN-starburst connection is observed by Ruschel-Dutra et al. using mid-infrared observations (2017); these authors report in 7 out of 15 AGN circumnuclear star formation is found in the vicinity of the nucleus; (b) sometimes AGN are associated with enhancement of star formation and yet AGN are preferentially found in the green valley with quenching-in-progress (Section 1.5.6). After a few rotations, the bar sweeps all the gas within its corotational radius, quenching the SF in the central region of the galaxy. Subsequently this region grows redder with time, decreasing the global sSFR of the galaxy; the bar becomes less and less visible, while a thicker but still rotationally supported stellar condensation (i.e., a boxy/peanut bulge) becomes clearly observable, often with a pseudobulge.

Spinoso et al. (2017) argue the strongest gas inflows and enhanced star formation happen at the onset of bar formation, when the bar is irregular and short, and therefore hard to detect; when the bar is stronger and well developed, and easy to observe, star formation has already ceased at the galactic centre. They also note a merger may trigger the instability associated with the development of a bar. They describe a cosmological 'zoom-in' hydrodynamical simulation ErisBH that examines a strong stellar bar which emerges in the late evolution of the simulated Milky Way-type galaxy; the simulation analyses the formation and evolution of the bar and the effect on galactic structure, gas distribution and star formation. During its early growth the bar drives gas inflows that enhance nuclear star formation, with a small portion of the inflow fueling the black hole, and after exhaustion of the gas in the central ~2 kpc star formation is low due to the absence of dense gas. Where gas inflow fuels a black hole, outflows may result: a majority of luminous AGN have winds and outflows, for example McElroy et al. (2015) used integral field spectroscopy to demonstrate winds and outflows in 16/17 galaxies in their sample of 17 Local, luminous type II AGN. Such outflows may remove or heat gas in massive galaxies, thereby inhibiting star formation and further AGN activity, and reducing galaxy luminosity.

1.2.3 Bulge Growth and Morphological Quenching

The importance of bulge growth in quenching has been emphasised by many authors (Bell et al. 2012; Pan et al. 2013; Genzel et al. 2014; Forster Schreiber et al. (2014); Lang et al. 2014; Tachella et al. 2015). These authors all state they find a correlation, rather than a proof that bulges cause quenching, however in their papers mechanisms are proposed whereby a bulge may shut down star formation. Van Dokkum et al. (2014) find that at fixed total mass and redshift, the presence of a dense core is a good predictor of quiescence while the absence of a dense core is a nearly perfect predictor of star formation. Bulges may act both through a high mass density and a conversion of a flat central disk into a spheroid. The growth of central mass concentration in a bulge is thought to stabilize a gas disk against fragmentation into dense clumps, and subsequent star formation, leading to less efficient star formation (Saintonge et al. 2012; Crocker et al. 2012; Martig et al. 2013; Tachella et al. 2015). Significant bulge growth precedes a departure from the star-forming main sequence, and quiescent galaxies have overall higher Sersic indices and Bulge-to-total flux ratios than star forming galaxies (Lang et al. 2014).

Bluck et al. (2014) study the origin of galaxy color bimodality in over half a million Local SDSS galaxies, using bulge and disc decompositions, and focus on central galaxies. The passive fraction varies as a function of both intrinsic galaxy structural properties, and of environment. The passive fraction for central galaxies is more tightly coupled to bulge mass, than any other intrinsic property leading the authors to conclude the physical mechanism(s) for inducing the cessation of star formation must be strongly coupled to the bulge. Bluck et al. (2019) report the bulge-to-total stellar mass ratio correlates more closely with the distance from the star forming main sequence than stellar mass, for both central and satellite galaxies, further emphasising the apparent relationship between the bulge and reduced star formation.

Bulge-dominated galaxies form stars less efficiently than disk-dominated ones (Martig et al. 2009; Saintonge et al. 2012). Martig et al. (2009) suggests *morphological quenching* stabilizes a disk against SF by a morphological transition from a rotating stellar disk to a pressure-dominated spheroid. The spheroid leads to greater stability of the gas, as shown by the Toomre parameter Q, through (a) the higher concentration of stellar mass in the spheroid, affecting Q via κ (κ is the epicyclic frequency or vorticity, which is produced by the shearing force which in turn relates to higher central concentration); and (b) the replacement of the stellar disk by the pressure-supported stellar spheroid, that is the removal of the stellar disk; the stellar disk increases instability by enhancing the self-gravity of perturbations in the disk (Martig et al. 2009). They show in simulations that once a galaxy develops a spheroid-dominated morphology, whether by major merger, minor merger, or disk instabilities, quenching of SF occurs without gas removal or suppression of gas supply by mechanisms such as AGN feedback, virial shock heating, or ram pressure stripping.

A recent study sought to identify the fractions of galaxies showing inside-out and outside-in quenching features, by quantifying the spatial distribution of quenched areas (Lin et al. 2019). More massive galaxies tend to have higher fractions of inside-out quenching than less massive ones, irrespective of their environments. These authors suggest that morphological quenching may be responsible for the inside-out quenching seen in all environments.

Saintonge et al. (2012) provide evidence that a gas disk, which would be otherwise unstable, can be made stable by a significant stellar bulge. Their studies of the variations in the molecular gas depletion time in galaxies show bulge-dominated galaxies fall systematically below the mean molecular Kennicutt-Schmidt relation (Kennicutt & Evans 2012), indicating that at fixed gas surface density they are less efficient at forming stars.

Morphological quenching caused by a morphological transition from a rotating stellar disk to a pressure-dominated spheroid is likely a real phenomenon, in that the physics is correct and appropriate; but that it is unlikely to be responsible for the major evolutionary trends of e.g. bimodality, and reduction in cosmic SFR. Cheung et al. (2012) dismiss morphological quenching as a cause of quenching on the basis early-type galaxies have low absolute gas contents compared to star-forming galaxies.

1.2.4 Strangulation

In strangulation the supply of cold gas onto a galaxy disk is halted, for example because the halo gas is stripped owing to external forces (Maier et al. 2016). In strangulation star formation can continue, using the gas available in the disk until it is completely used up. Maier et al. (2016) study the MACS J0416.1-2403 galaxy cluster and compare a region of galaxies accreted longer ago, with a region of recently accreted and infalling galaxies. The long accreted star-forming galaxies have higher metallicities compared to the recently accreted and infalling galaxies. They show strangulation is needed to explain the higher metallicities of accreted cluster galaxies by study of chemical evolutionary paths of model galaxies with and without the inflow of gas.

Peng, Maiolino & Cochrane (2015) perform an analysis of stellar metallicity in SDSS galaxies showing that strangulation is the primary mechanism responsible for quenching star formation, with a typical timescale of four billion years, at least for Local galaxies with a stellar mass less than 10^{11} $M_{\odot}$. They report most quenched galaxies have clear evidence of strangulation whereby the supply of cold gas to the galaxy is cut. Measurements of metallicity can distinguish between sudden gas removal through a massive outflow or strong ram pressure stripping, when the stellar metallicity and stellar mass of the quiescent galaxy are the same as those of its star-forming progenitor just before quenching; and strangulation, when star formation can continue using the gas available in the galaxy until it is completely used up and the gas metallicity increases because of the lack of dilution from inflowing gas. The strangulation galaxies have a stellar metallicity that is much higher than their star-forming progenitors, and a slightly higher stellar mass. A statistical analysis of the metallicity difference between star-forming and quiescent SDSS galaxies showed the stellar metallicity of quiescent galaxies is noticeably higher than for star-forming galaxies consistent with the strangulation scenario (Peng et al. 2015). The metallicity difference decreases with increasing stellar mass, reaching the maximum value around 0.4 dex for galaxies at Mstar $< 10^{9.5} M_{\odot}$ and becomes negligible at Mstar $\geq 10^{11} M_{\odot}$. Strangulation implies the supply of cold gas to the galaxy is cut, and thus Peng et al.'s result argues against commonly cited quenching mechanisms such as gas removal thorough outflows, or centrally located quenching mechanisms such as bar-driven quenching or morphological quenching.

McIntosh et al. (2014) describe strangulation as an important quenching mechanism. They note the growth of the red galaxy population at z ~ 0 has occurred largely above the characteristic mass limit of galaxy stellar mass $\geq 3 \times 10^{10} M_{\odot}$ that broadly divides galaxies into the blue cloud of late-type (disc-dominated) systems and the red sequence of early-type galaxies (ETGs) including elliptical, S0 and bulge- dominated spirals. Low- to moderate-mass red sequence galaxies are produced by migrating blue-cloud galaxies that experience star formation quenching, with strangulation as the main quenching mechanism for the bulk of low-redshift satellite galaxies including those in the outskirts of galaxy clusters. The assembly of the most massive galaxies $> 10^{11} M_{\odot}$ occurs by dissipationless (dry) merging of pre-existing red systems (McIntosh et al. 2014).

Note that strangulation removes the need for Localised effects (outflows, bars, etc.) as drivers of the suppression of SF needed to explain the cosmic SFR evolution, or colour bimodality. The strangulation mechanism is supported by a finding of coherent star formation (Nelson et al. 2016). Radial profiles of SF in galaxy disks indicate that there is no preference for quenching to be located at the centre or periphery. If SF is found to be low in one area (say the centre), it will also be low in the periphery of the galaxy and elsewhere in the disk; and conversely if a galaxy has high overall SF, so that it is above the SF main sequence, then SF will be found to be high in all areas of the galaxy (Nelson et al. 2016). Thus galaxies with quenching-in-progress may show an even decline of star formation that occurs across the disk. Coherent star formation has recently been reported in a study of MaNGA galaxies (Ellison et al. 2018); although these authors avoid the use of the term coherent, their description of the distribution of SF is consistent with Nelson et al. (2016).

1.2.5 The Role of the Cosmic Web in Star Formation and Quenching

The 3D distribution of galaxies in our Universe exhibits a visually striking web-like pattern, a filamentary network composed of geometrically distinct components termed voids, sheets, filaments, and knots, known as the cosmic web (Metuki et al. 2015; Alam et al. 2019). Libeskind et al. (2018) provides a description and review of each component. The network has the massive galaxy clusters (knots) as its centres, which are interconnected through filaments and sheets; these components provide most of the mass of the Universe, while the volume is dominated by vast near-empty regions called voids (Cautun et al. 2014). These components display structures and substructures over a wide range of scales and densities, and demonstrate the hierarchical development of the cosmic web (Cautun et al. 2014). Filaments are described as the highways of the Universe, as transport channels whereby mass and galaxies are channelled into higher density cluster regions (Libeskind et al. 2018). Large scale filaments are the presumed channels of gas flow over cosmic time (Alpaslan et al. 2016).

A number of studies have sought to determine whether the location of a galaxy relative to filiaments predisposes it to higher or lower stellar mass growth (either in the past or currently (Darvish et al. 2014; Alpaslan et al. 2016; Snedden et al. 2016; Kraljic et al. 2018). Kraljic et al. (2018) analysed the stellar mass, $u - r$ dust corrected colour and specific star formation rate of galaxies as a function of their distances to the 3D cosmic web features, such as nodes, filaments and walls. More massive and/or passive galaxies are located closer to the filament and wall than their less massive and/or star-forming counterparts. The red fraction of galaxies increases when closing in on nodes, and on filaments regardless of the distance to nodes.

Darvish et al. (2014) note that studies of the environmental dependence of the SFR in galaxies at $z \geq 1$ have yielded conflicting results. However at $z \sim 1$ there is an increase of SF activity for star-forming galaxies at intermediate densities, likely associated with galaxy groups, followed by a decline for the richest clusters. 'Intermediate' densities and/or 'group' environments are likely to be filaments. Darvish et al. (2014) report the observed fraction of star-forming galaxies is enhanced in filaments, relative to the field and cluster environments at $z \sim 0.8$-0.9. Sobral et al. (2011) report the median SFR of Hα emitter galaxies at $z= 0.84$ is found to increase with density for both field and intermediate (group or cluster outskirts) densities; while stellar mass is the primary predictor of star formation activity at $z \sim 1$, increasing density enhances the median SFR of (lower mass) star-forming galaxies in low density environments, but ultimately suppresses star formation activity in all galaxies above surface densities of 10-30 Mpc^{-2} in group and cluster environments.

Alpaslan et al. (2016) investigate the location of SF galaxies along filaments in the cosmic web and how SFR may vary according to a galaxy's placement beside or within a filament (Figure 1.7). These authors conclude spiral galaxies at the edges of filaments have greater access to reservoirs of star forming gas compared to similar galaxies in the cores of filaments. Alpaslan et al. (2016) report stellar mass plays a decisive role in determining galaxy properties, and any effects arising from the large-scale structure are second-order perturbations; nontheless spiral galaxies at the edges of filaments, on the borders of voids, have higher sSFRs (at fixed stellar mass), and lower stellar masses compared to their counterparts at the cores of filaments.

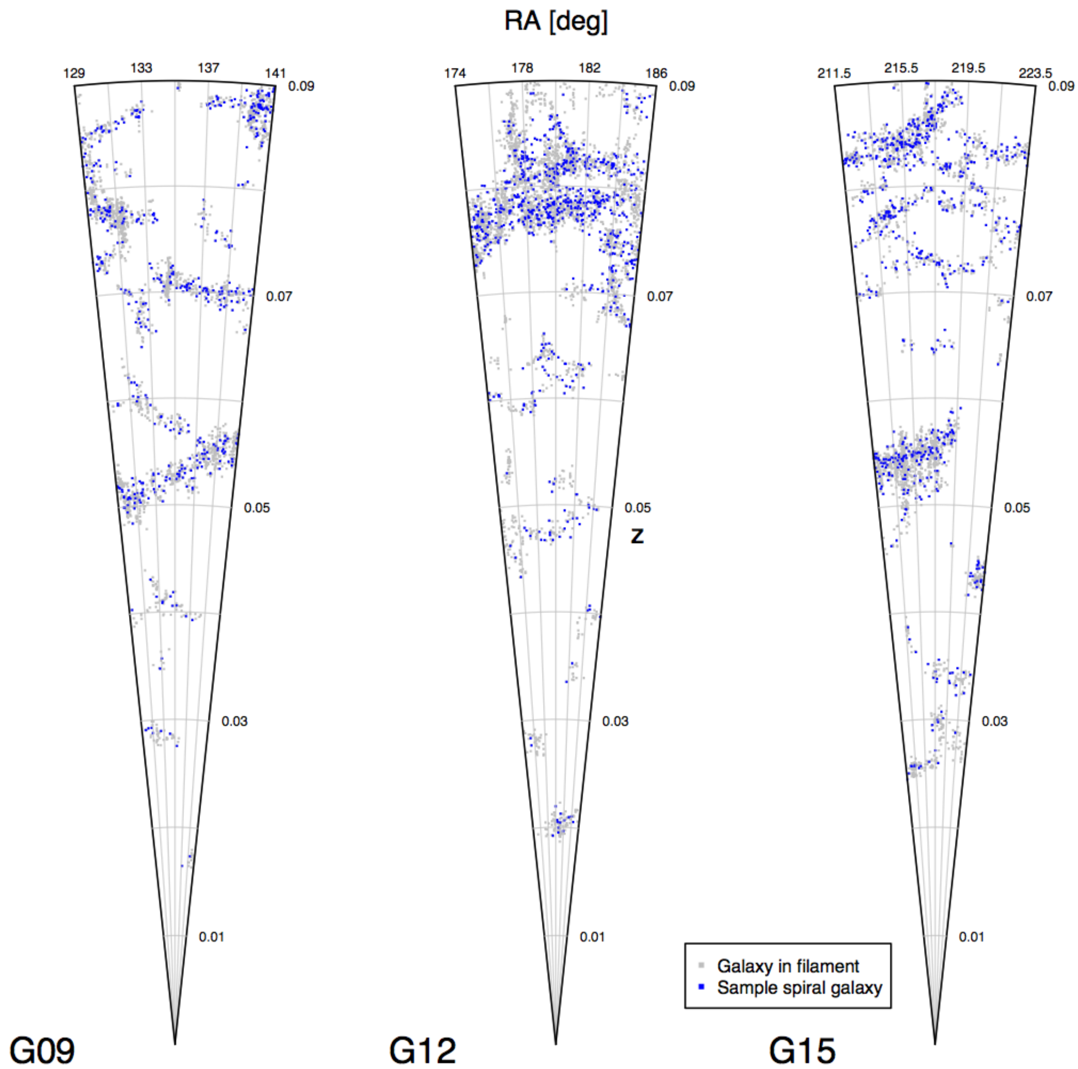

Figure 1.7: *The figure is taken from Alpaslan et al. 2016, Fig. 2. It displays the three equatorial GAMA fields (G09, G12 and G15) and the galaxies that are filament galaxies. All the filament galaxies in the low redshift large-scale structure catalogue are shown as grey points. The blue points are nonAGN spiral galaxies that are not in groups or pairs. These authors conclude a location of spiral galaxies at the edges of filaments provides greater access to reservoirs of star forming gas compared to similar galaxies in the cores of filaments.*

Aragon-Calvo & Szalay (2013) use an N-body simulation to study galaxy haloes inside voids. These authors point out the notion that voids are empty regions is not entirely accurate; high-resolution simulations show voids are filled with a complex web of tenuous filaments and low-mass haloes. They find that haloes inside voids feed through highly coherent laminar streams of matter (gas), unlike the environment inside filaments and clusters where the velocity field is turbulent. These streams appear to provide an efficient gas feeding mechanism with low accretion rates that can be sustained for large periods of time. This steady and coherent gas accretion may explain some of the observed properties of galaxies in voids and low-density environments including extended gas discs, polar discs, higher gas content and star formation rates (Aragon-Calvo & Szalay 2013). The demonstration of a relationship between the SFR of a galaxy and its position in relation to a cosmic web filament supports a theory whereby a detachment from its feeding filament may lead to quenching (see Cosmic Web Detachment Subsection below, that describes detachment events as a major merger; accretion of a satellite; or cosmic web infall/crossing).

Sanchez Almeida et al. (2014) report a fingerprint of the cosmic web gas at low redshift is its low metallicity (between 10^{-2} and 10^{-3} $Z_{\odot}$). The metallicity of cosmological origin is not zero because of a small amount of contamination from the first population III stars.

Alam et al. (2019) present a different view to Aragon-Calvo & Szalay (2013); they consider whether the properties of galaxies and their halos vary according to the Local cosmic web environment. They ask whether there is any impact on the galaxy properties according to the different tidal forces that are found in different geometrical locations within the web. Using SDSS data and the construction of a mock galaxy catalogue, these authors find evidence that the halo mass plays the primary role in shaping the galaxy content inside individual dark matter haloes; the lack of strong cosmic web effects on the colour transformation of galaxies implies the galaxy quenching is a relatively Local process that is contained within the boundary of haloes and that the tidal modulation of the large-scale cold gas accretion is unlikely to be the controlling factor triggering galaxy quenching.

1.2.6 The Cosmic Web Detachment model of Quenching

The Cosmic Web Detachment (CWD) model is a conceptual framework to interpret galaxy evolution in a cosmological context, providing a direct link between the star formation history of galaxies and the cosmic web (Aragon-Calvo, Neyrinck & Silk 2019). The CWD model unifies several mechanisms known to disrupt or stop star formation into one single physical process and provides a explanation for many galaxy properties.

Galaxies begin accreting star-forming gas in their formation phase via a network of primordial highly coherent filaments. The efficient star formation phase ends when a CWD process occurs, including a major merger; accretion of a satellite galaxy; or a collision of the galaxy with a wall or filament. These interactions with other galaxies or elements of the cosmic web can detach the galaxy from its network of primordial filaments so the galaxy can no longer accrete cold gas and star formation stops.

The stripping of the filamentary web around galaxies is the physical process responsible of star formation quenching in gas stripping, harassment, strangulation and starvation. CWD may act at a more fundamental level than internal feedback processes because it is a purely gravitational/mechanical process. Aragon-Calvo et al. (2019) state cosmic web detachment is fundamentally a starvation process consistent with the strangulation process described by Peng et al. (2015) triggered by non-linear interactions between galaxies and other galaxies or their environment. There is a clear correlation in the model between web detachment events and major mergers. It is suggested that a galaxy entering a wall, filament or cluster is in effect being slammed against a wall of gas which may inject gas into the central black hole and activate an AGN (Aragon-Calvo et al. 2019).

Aragon-Calvo et al. (2019) argue that according to the hierarchical scenario of galaxy formation small galaxies form first (and therefore their population should be composed of old stars) while massive galaxies form later (and as such they should be forming stars at the present time). The opposite is actually observed: massive galaxies are no longer producing stars while low-mass galaxies are actively forming new stars. This apparent anti- hierarchical behavior of the star formation history of galaxies is commonly referred to as ‘downsizing’. The key to downsizing is the realization that low-mass star-forming galaxies are found mostly in isolated environments and therefore their surrounding cosmic web has remained unperturbed for most of the history of the Universe (Aragon-Calvo et al. 2019). Low-mass isolated galaxies can therefore experience a slow but steady gas accretion; on the other hand, massive galaxies form in dense environments where there is a higher rate of web detachment events due to the non-linear dynamics characteristic of such environments. The net effect is the observed anti-hierarchical star formation history.

Kraljic et al. (2018) note that a decline of star formation activity can be due to a quenching process such as strangulation, where the supply of cold gas is halted (Peng, Maiolino & Cochrane 2015), and could also occur in the cosmic web detachment (Aragon-Calvo et al. 2019), where turbulent regions inside filaments prevent galaxies to stay connected to their filamentary flows and thus to replenish their gas reservoir.

1.2.7 Halo Quenching

When a galaxy grows more massive than the characteristic mass M* $\geq 2 \times 10^{11}$ $M_\odot$, a transition occurs in their evolution possibly associated with the shock heating of the infalling gas. Above this mass galaxies are embedded in massive and hot X-ray haloes that prevent any further cold gas accretion on to the galaxy (Cappellari et al. 2013).

When galaxies form by spherical infall of gas inside dark matter haloes, the gas is first heated to the halo virial temperature behind an expanding virial shock (Birnboim & Dekel 2003). The gas then cools radiatively while supported by pressure in a quasi-static equilibrium; and gas slowly contracts to a disc where it eventually forms stars. Birnboim & Dekel (2003) find a virial shock does not develop in most haloes that form before z $\sim$ 2, and not in haloes less massive than 2 $\times 10^{11} M_\odot$; in these haloes the infalling gas is not heated to the virial temperature until it hits the disc, and this implies there is no cooling-dominated quasi-static contraction phase.

Birnboim & Dekel (2007) identify a generic sequence of events (Shocked-Accretion Massive Burst and Shutdown, SAMBA) whereby the build-up of galaxies by spherical gas accretion through dark matter haloes is subject to the development of virial shocks. SAMBA gives rise to a substantial population of $\sim 10^{11} M_\odot$ galaxies with a strongly suppressed star formation rate at z $\leq$ 1. The quenching and bursting occur at all redshifts in galaxies of baryonic mass $\sim 10^{11} M_\odot$ and involve a substantial fraction of this mass. There are 4 phases of SAMBA: (i) continuous cold accretion while the halo is below a threshold mass $M_{sh} \sim 10^{11} M_\odot$; (ii) tentative quenching of gas supply for $\sim$ 2 Gyr, starting abruptly once the halo is $\sim M_{sh}$ and growing a rapidly expanding shock; (iii) a massive burst due to the collapse of $\sim 10^{11} M_\odot$ gas in $\sim$ 0.5 Gyr, when the accumulated heated gas cools and joins new infalling gas; and (iv) a long-term shutdown.

There is observational support for such a halo quenching scenario in a galaxy called G1 at z=0.67 (Churchill et al. 2012). A filamentary structure that is a metal-poor HI complex mostly comprising cold gas is accreting into the halo of galaxy G1 and is observed to be experiencing virial shock heating and dynamical disruption. Consistent with predictions of both theoretical treatments (e.g., Birnboim & Dekel 2003; Birnboim et al. 2007) and cosmological simulations the observations indicate that the gas accreting into the halo of galaxy G1 at times after its formation epoch has not accreted onto the galaxy itself; and the analysis indicates that the HI complex will not accrete onto the galaxy. The authors conclude the star formation of galaxy G1 has likely been quenched for gigayears.

Further observational support for halo quenching comes from the discovery of a bright, spectrally flat γ-ray ring at the expected virial shock position for 112 massive, high latitude, extended galaxy clusters (Reiss et al. 2017). These authors stack the 1-100 GeV Fermi-LAT data over ~8 years, and radially bin the data. The nearby Coma cluster has also shown evidence for a γ-ray virial ring. Reiss et al. (2017) conclude the γ-ray ring supports and calibrates the virial shock model.

1.2.8 AGN Feedback

The extent to which AGN feedback is responsible for the decline of star formation in large elliptical galaxies is an outstanding question in galaxy evolution. Many authors have proposed AGN powered by central supermassive black holes (BHs) are a critical part of the quenching process: Di Matteo, Springel & Hernquist (2005); Hopkins et al. (2005); Croton et al. (2006); Sijacki et al. (2007); Bower et al. (2008); Di Matteo et al. (2008); Cattaneo et al. (2009); Johansson, Naab & Burkert (2009); Fabian (2012); Dubois et al. (2013, 2016); Pontzen et al. (2017). AGNs drive rapid outflows which can be directly observed in post-starburst galaxies (e.g. Tremonti, Moustakas & Diamond-Stanic 2007; Rupke & Veilleux 2011), suggesting that BHs are able to suppress SF by removing the supply of gas.

Cattaneo et al. (2009) claim the central bulges of spirals structurally resemble miniature ellipticals. All ellipticals, and spirals with bulges contain a central black hole, and ellipticals and bulges within spirals have the same black hole mass to stellar mass ratio, of the order of 0.1% (Ferrarese & Merritt 2000, Cattaneo et al. 2009). Cattaneo et al. (2009) note that black holes release vast amounts of energy that powers quasars and other weaker active galactic nuclei. Even a tiny fraction (<1%) of this energy released within a bulge is sufficient to halt star formation by heating and ejecting ambient gas, which suggests a possible AGN role in quenching in large elliptical galaxies.

Salim et al. (2007) report star-forming galaxies with no AGN form a well defined linear star-forming sequence - the MS (Figure 1.6). However a significant fraction of AGN galaxies populates the green valley in between the blue cloud and the red sequence on the colour–magnitude diagram, where most galaxies are AGNs or AGN/SF composites.

The 'radio-mode' AGN feedback proposed by Croton et al. (2006) demonstrates that the galaxies situated in dark halos above a transition mass (a halo virial mass of 2-3 x $10^{11} M_{\odot}$), start to suppress the accretion of gas, and at the same time suppress further star formation. The ‘radio mode’ feedback injects sufficient energy into the surrounding medium to reduce or even stop the cooling flow of gas, explaining why the gas at the centre of most galaxy clusters does not condense and turn into stars when the observed X-ray emission indicates a cooling time much shorter than the age of the cluster (Croton et al. 2006). In the Local Universe radio galaxies generally operate in radio-mode and mechanical energy deposited by the jet heats the ambient gas and prevents radiative cooling, thus inhibiting star formation.

Radio-mode feedback occurs in massive galaxies containing massive black holes accreting at very low fractions of the Eddington limit (the maximum luminosity a star can achieve when there is balance between the force of radiation acting outward and the gravitational force acting inward), and is commonly observed in local giant ellipticals. Accreting BHs at the centre of galaxies release huge amounts of energy into the surroundings in both radiative and kinetic forms (Werner et al. 2014; Ishbashi et al. 2014). McNamara et al. (2014) has demonstrated radio-mode feedback not only heats hot atmospheres surrounding elliptical galaxies and BCGs (brightest cluster galaxies which are the largest and most luminous galaxies in the Universe), it is able to sweep higher density molecular gas away from their centers.

The low radiative efficiency in radio-mode is in contrast to quasar-mode AGN which have high radiative efficiency and high accretion rates close to the Eddington limit. The Eddington luminosity is calculated as 1.2 x $10^{38} M/M_{\odot}$ ergs/sec. The radiative or quasar-mode is usually seen at high redshifts (z ~ 2), close to the peak epoch of AGN activity. In the quasar-mode, AGN feedback suppresses star formation in the host galaxy by removal of the ambient gas.

New ALMA observations suggest an AGN feedback model - stimulated feedback - in which thermal instabilities occur preferentially when cool, X-ray emitting gas lying within the central galaxy is lifted to higher altitudes behind buoyant X-ray bubbles inflated by radio AGN (McNamara et al. 2016). The rising X-ray bubbles simutaneously heat hot atmospheres and regulate cooling and star formation, while promoting cooling in their wakes.

Strong observational evidence of AGN feedback is seen (a) in the form of pc-scale relativistic winds (e.g., Tombesi et al. 2010a,b) and (b) massive outflows on scales from sub-kpc (Alatalo et al. 2011) to several kpc (Sturm et al. 2011; Rupke & Veilleux 2011; Cicone et al. 2014). Both of these forms of feedback have been seen in a type 1 ultraluminous infrared galaxy, IRAS F111191+3257 (Tombesi et al. 2015). McElroy et al. (2015) use integral field spectroscopy to demonstrate winds and outflows are present in 16/17 galaxies in their sample of 17 Local, luminous type II AGN.

Forster Schreiber et al. (2014) report powerful nuclear outflows are ubiquitous in galaxies with log M* > 11, that are plausibly driven by AGN; such outflows appear less common in galaxies at lower masses. Along with star formation driven winds in the outer parts of the galaxies, such outflows could efficiently remove gas from the galaxies and, in this way, contribute to the quenching process.

An AGN role in inside-out quenching is supported by Taylor & Kobayashi (2016; 2017) who have performed cosmological chemodynamical simulations that include both detailed chemical enrichment and feedback from AGN; they show that in massive galaxies (M_* >11.0) falling below the MS, inside-out quenching is demonstrated in the radial SFR from 0-0.8 R_e in AGN galaxies but not in galaxies without AGN.

Belfiore et al. (2016, 2017a) argue against the AGN origin of LIER (low ionization emission-line region) regions, instead supporting the scenario where LIERs are caused by photoionization from a diffuse ionizing background produced by hot evolved stars. Galactic regions that are often classified as 'LINERs' (low ionization nuclear emission-line regions) in the BPT diagnostic diagram (discussed in 2.7 are relabelled LIER as they are not confined to nuclear regions. LIERs are readily formed by the hard ionizing spectrum of post-asymptotic giant branch (pAGB) stars. These authors claim a typical low luminosity AGN does not emit enough energy to be the dominant contributor to the ionizing flux on the kpc scales probed by the SDSS or MaNGA surveys. In LIER galaxies without SF, line ratios sensitive to the ionization parameter ([O III]/[O II], [O III]/H_β) show flat or very shallow profiles over radial scales of tens of kpc which is not consistent with the steeper radial profiles predicted in an AGN scenario; with an AGN a large scatter is expected in the EW_$H\alpha$ profiles, as line and stellar continuum emission would originate from independent sources, instead the radial profile of LIERS is flat with little scatter.

1.2.9 AGN Feedback that triggers SF

Feedback from the central black hole is usually invoked in galaxy formation and evolution models to *suppress* star formation. However, AGN feedback may also operate in the opposite direction and even trigger star formation in the host galaxy (Ishibashi & Fabian 2012; Zubovas & King 2016). AGN may co-exist with circumnuclear starbursts with an apparent AGN-starburst connection (Ruschel-Dutra et al. (2017). Mahoro et al. (2017) study a sample of 1472 AGN hosting galaxies identified by X-ray and 221,154 nonAGN galaxies and use U-B rest-frame colors to locate galaxies in the green valley with criteria 0.8 $\leq$ U - B $\leq$ 1.2. Measurements of star formation using FIR Herschel/PACS data demonstrate most AGN are located on or above the main-sequence of star formation indicating rather than star formation quenching, AGN host galaxies display SF enhancement (Mahoro et al. 2017).

Zubovas & King (2016) use an AGN wind outflow semi-analytical model to investigate the propagation of AGN-driven outflows and the effect that the pressure of the outflows exerts on galaxy discs. They find star formation enhancement in the outskirts of galaxy discs may result from AGN-driven outflows because of the difference in pressure between the wind outflow and the disk. The outflow pressure is uniform inside the contact discontinuity, however the internal disc pressure decreases with decreasing gas surface density Σ_g and radius, so the outflow pressure becomes more significant. The outflow-to-disc pressure ratio increases from typically negligible values close to the galaxy centre to $P_{ext}/P_d \sim 3$ at the outer edge of the outflow.

Ruschel-Dutra et al. (2017) analyse the presence of circumnuclear star formation in a sample of 15 AGN using mid-infrared observations, to investigate theoretical predictions for the AGN-starburst connection. In 7/15 AGN circumnuclear star formation is found in the vicinity of the nucleus (distances as low as tens of parsecs from the nucleus). The intense continuum emission from the AGN complicates measurement of the SFR, however these authors use the emission band at 11.3 μm PAH flux in conjunction with empirical relations for the SFR as this band is relatively insensitive to the radiation from the accretion disc. They report a correlation with the bolometric luminosity of the AGN only for objects with $L_{AGN} \geq 10^{42}$ erg s^{-1}, and no correlation with lower luminosity AGN where the radiative energy output due to star formation tends to be higher than the central engine.

The structure and evolution of the dense nuclear star cluster in the central parsec surrounding Sgr A* in the Galactic Center is reviewed by Genzel et al. (2010) ‘including the astounding fact that stars have been forming in the vicinity of Sgr A* recently, apparently with a top-heavy stellar mass function’. The nuclear star cluster in the central parsec is one of the richest concentrations of young massive stars in the entire Milky Way; there is uncertainty how the stars arrived there. The tidal shear from the central mass is so high gravitational collapse of gas clouds requires gas densities higher than the critical 'Roche' density, exceeding by several orders of magnitude the density of any gas currently observed in the central region. The required cloud densities approach conditions in outer stellar atmospheres, which seem implausible. An alternative explanation that the stars formed elsewhere in more benign formation regions and were transported into the central core by two-body relaxation also is not straightforward. A favored explanation is in situ formation in a dense gas accretion disk that can overcome the tidal forces.

1.2.10 Galaxy Environment and Quenching

Environmental factors have been long recognized to play a role in galaxy evolution and quenching in dense environments, by preventing gas from reaching galaxies or by removing gas reservoirs. They include ram pressure stripping, strangulation and harassment (Bekki, Couch & Shioya 2002; Fujita 2004; Kawata & Mulchaey 2008; Peng, Maiolino & Cochrane 2015; Schaefer et al. 2019).

Bianconi et al. (2016) discuss how cluster environments accelerate the ageing process of galaxies. The morphology-density relation (Dressler 1980) implies that environment affects the star formation history and structure of galaxies with young and active galaxies typically found in the cluster outskirts, and passive ones in the cluster core. Environment effects include ram pressure on gas present in a galaxy as it travels through the cluster due to the intracluster medium, with the gas compression causing sudden enhancement of the star formation but also later gas removal; stripping of the hot gaseous halo as a galaxy falls into a galaxy cluster by gravitational interactions can cause strangulation by cutting gas supply and preventing further gas accretion; and harassment results from the high density of galaxies causing frequent gravitational encounters that perturb the dynamical equilibrium of the gas and promote collapse of gas clouds, new bursts of SF and subsequent ejection of a portion of the remaining gas by stellar winds.

Maier et al. (2016) describe strangulation as a scenario in which the supply of cold gas onto the galaxy disk is halted because the halo gas is stripped owing to external forces (see above under strangulation, Section 1.2.4). In strangulation star formation can continue, using the gas available in the disk until it is completely used up. These authors study the MACS J0416.1-2403 cluster and compare a region of galaxies accreted longer ago, with a region of recently accreted and infalling galaxies. The long accreted star-forming galaxies have higher metallicities compared to the recently accreted and infalling galaxies.

Galaxies falling into a cluster interact with other galaxies causing interruption of the inflow of pristine gas, which leads to strangulation.

Mayer et al. (2007) report simulations of dwarf spheroidal galaxies showing that the progenitors of these galaxies were probably gas-dominated dwarf galaxies that became satellites of a larger galaxy earlier than the other dwarf spheroidals. They find that a combination of tidal shocks and ram pressure swept away the entire gas content of such progenitors about ten billion years ago.

van den Bosch et al. (2008) examine a number of transformation and quenching mechanisms in addition to merging, which are special in that they only operate on satellite galaxies. When a small halo is accreted by a larger halo its hot, diffuse gas may be stripped either entirely or partially, thus removing its fuel for future star formation and leading to a slow process of strangulation. When the external pressure is sufficiently high, ram pressure may also remove the cold gas of the satellite galaxy resulting in an extremely fast quenching of its star formation, and the complete removal of the cold gas reservoir is referred to as 'ram-pressure stripping'. These two quenching mechanisms can transform blue satellite galaxies to the red sequence, but they do not have a big impact on the morphology of the satellite galaxy; the transformation mechanisms operating on satellites affect colour more than morphology. These authors (like McIntosh et al. 2014) argue that strangulation is the main transformation mechanism for satellite galaxies.

Davies et al. (2016) note quenching involves a complex mix of galaxy mass and Local environmental effects. They suggest that different quenching processes dominate the transition from star forming to passive systems at distinct stellar masses, and propose a characteristic stellar mass scale between environmental quenching via ram pressure stripping of cold gas, and environmental quenching via starvation at log galaxy stellar mass ~8; and between environmental quenching via starvation, and mass quenching at log galaxy stellar mass ~10. Davies et al (2016) find that passive fractions are higher in both interacting pair and group galaxies than the field at all stellar masses, and this effect is most apparent in the lowest mass galaxies. Thus all passive $\log[M_*/M_\odot] < 8.5$ galaxies are found in pair/group environments; this finding is consistent with other studies. Galaxy-galaxy interactions are required to form passive low-mass galaxies (Geha et al., 2012; Weisz et al. 2011); and Peng et al. (2012) conclude environmental quenching must be the dominant factor in producing red low-mass systems.

1.3 Addressing Quenching via Integral Field Spectroscopy

Integral field spectroscopy (IFS) - also called Integral field unit spectroscopy (IFU) - was developed to provide 2 dimensional spectroscopy of stars and gas, that can explore the dynamical structure of galaxy disks and bulges. IFS provides the spatially extended internal kinematics and line-strength distributions that are not available to single-aperture surveys. It constitutes a major development in optical astronomy, however only a brief discussion of key issues can be presented here. In a nutshell, the complexity of galaxies is not captured with a single aperture spectrum (Green et al. 2018). Prior to IFS major spectroscopic surveys that used a single fibre (for example the 2dF Galaxy Redshift Survey (Colless et al. 2001); the Sloan Digital Sky Survey (Abazajian et al. 2003)), or single slit (for example the VIMOS VLT Deep Survey (Le Fevre et al. 2005) and the All-Wavelength Extended Groth Strip International Survey (AEGIS) (Davis et al. 2007)) on each object obtained just one integrated measurement of parameters such as current star formation rates, gas phase metallicities, stellar ages, etc. for each galaxy. These single measurements reflect the location of the aperture but may not be representative of the galaxy as a whole (Croom et al. 2012). Most importantly single measurements cannot identify gradients in the SFR or stellar populations across a galaxy disk that might indicate evolutionary processes such as the presence of quenching.

The gains in information from IFS compared to single-fibre surveys include: the spatial distribution of gas and star formation, kinematic information revealing the mass and dark matter distributions including tracing regularity or disturbance in gas or stellar motions, gradients across the galaxy in stellar and/or gas metallicity and age, and maps of resolved emission lines that allow study of the processes driving ionization in different parts of the galaxy (Bryant et al. 2015; Schaefer et al. 2017; Morselli et al. 2018). IFS allows the spatial distribution of star formation in galaxies to be resolved, and the results of the various quenching mechanisms to be observed in a large set of galaxies (Schaefer et al. 2017). It permits measurement of both the current star formation via emission lines, and the integrated star formation history via stellar age and metallicity. The mean stellar age is effectively a luminosity-weighted integral of the star formation history; and the stellar metallicity gradient provides an indication of its merging history.

Further examples of the uses of IFS include Bacon et al. (2001), Thorp et al. (2019), Taylor and Kobayashi (2017), Belfiore et al. (2017b), and Delgado et al. (2016). Many galaxy components are not spherical or even axisymmetric but are triaxial, for example many bulges and bars are triaxial (Bacon et al. 2001) and in many elliptical galaxies the inner and outer regions appear to rotate around different axes. Such galaxies are difficult to map with traditional long-slit spectroscopy along at most a few position angles. To examine galaxy mergers Thorp et al. (2019) studied spatially resolved star formation and metallicity profiles using IFS, finding that the SFR is generally centrally enhanced by a merger by a factor of 2.5 on average. They report most of the post- mergers have either normal or suppressed central metallicities, and that values are suppressed on extended scales throughout the disk, to at least 1.9 R_e. Taylor and Kobayashi (2017) report stellar metallicity gradients in simulations of massive galaxies (mass $\geq 3 \times 10^{11} M_{\odot}$) are made flatter by mergers (meaning that their centres no longer show greater chemical enrichment than the outskirts) and are unable to regenerate due to the quenching of star formation by AGN feedback. Belfiore et al. (2017b) has pointed out that metals are direct products of stellar nucleosynthesis; in this way chemical evolution studies become a powerful tool to understand star formation and gas flows in and out of galaxies. These authors note important galaxy properties such as star formation rate and metallicity can have substantial gradients so observations of the central regions may not represent global values. Delgado et al. (2016) also note the problem that non-IFS studies only partially cover a galaxy and are thereby subject to aperture effects. Delgado et al. (2016) emphasizes the importance of the SF history and the measurement of SFRs to understanding galaxy evolution, and how the lack of spatially resolved information has been a major limitation that is now becoming addressed by integral field spectroscopy surveys such as ATLAS3D (Cappellari et al. 2011), CALIFA (Sanchez et al. 2012), SAMI, and MaNGA (Bundy et al. 2015).

1.3.1 The SAMI Galaxy Survey: Introduction

The main goal of the SAMI Galaxy Survey (Bryant et al. 2015) is to provide a complete census of the resolved optical properties of nearby galaxies including star formation rate and distribution, age, metallicity, and kinematics across a wide range of environments. The science goals discussed in Croom et al. (2012) include understanding: (a) how did the galaxy population observed today with some very distinctive features come about; (b) key galaxy properties such as color bimodality and morphology; and (c) key physical processes that occur as galaxies form and evolve, including the build up of angular momentum, stellar feedback and the distribution of star formation. The SAMI Galaxy Survey commenced in

2013 and will observe a total of ~3600 galaxies with the upgraded Sydney- AAO Multi-object Integral field spectrograph (SAMI) on the Anglo-Australian Telescope (AAT) over 4 years (Croom et al. 2012; Green et al. 2018).

Previous and ongoing studies of SAMI galaxies include kinematic properties (Fogarty et al. 2015), *asymmetry in gas kinematics* (Bloom et al. 2017), dynamical scaling (Cortese et al. 2014), *spatially resolving the environmental quenching of SF* (Schaefer et al. 2017), *galaxy classification through high-order stellar kinematics* (van de Sande et al. 2017), galaxy rotation curves for gas and stars (Cecil et al, 2016), *energy sources of turbulent velocity dispersion* (Zhou et al. 2017), *spatially resolving the main sequence of star formation* (Medling et al. 2018), *mass as the driver of the kinematic morphology - density relation in clusters* (Brough et al. 2017), *Star-forming, rotating spheroidal galaxies in the GAMA and SAMI surveys* (Moffett et al. 2019), and Data Release one with emission-line physics value-added products (Green et al. 2018). The papers in italics cover studies in which I have been involved and I am listed as a co-author. (A complete list of my publications is included in the Appendix 7.1).

The SAMI multiobject integral field spectrograph uses a new kind of fibre bundle - the hexabundle - in order to achieve high fill-factor spatially-resolved 3D spectroscopy over a 1° diameter field (Sharp et al. 2015). Each hexabundle has 61 optical fibres with cores that subtend 1.6 arcsec on the sky, giving a total hexabundle diameter of 15 arcsec. Hexabundles have a physical size <1 mm and a filling fraction of 73%; 13 of these hexabundles manually plug into a field plate with pre-drilled holes, which is installed at the prime focus of the Anglo-Australian Telescope. This instrument allows simultaneous IFS observations of 12 galaxies and one calibration star thereby speeding up the rate galaxy observations are collected compared with single IFU instruments.

The SAMI target selection and sampling, including four volume-limited samples based on pseudo-stellar mass cuts, are described in Section 2.2. The galaxies comprising the SAMI Galaxy Survey sample are chosen from the GAMA survey sample (Driver et al. 2009) with an additional 8 galaxy clusters. The sampling aims to represent a broad range in environment density and stellar mass. The complete SAMI Galaxy Survey sample contains supplementary, low redshift dwarf galaxies (Bryant et al. 2015). The key science drivers for SAMI require a galaxy sample that is evenly distributed over a broad range of stellar masses. Various feedback processes that are inherently mass-dependent have been incorporated into galaxy formation models and so require data covering a wide mass range to allow testing of feedback processes.

GAMA, the parent survey for SAMI, is a deep, highly complete spectroscopic survey of galaxies made in three equatorial regions centred on 9, 12 and 15 hours Right Ascension, with additional fields observed at 2 and 23 hours Right Ascension, -35° to -30° and -10.25$circ$to -3.72° declination respectively (Driver et al. 2011, Liske et al. 2015). The equatorial fields have 98.5% complete spectroscopy to r = 19.8 mag, two magnitudes deeper than the SDSS (Liske et al. 2015). All the galaxies studied in this thesis are within the GAMA G09, G12 and G15 fields (where the number refers to the respective Right Ascension of the fields).

The SAMI Galaxy Survey is reviewed and compared to other large IFS Surveys in terms of spatial resolution, spectral resolution, flux calibration, environment measures, mass range and sampling of galaxy clusters in Green et al. (2018). For example a test of the absolute flux calibration directly compares SAMI cubes to SDSS g-band images. Green et al. (2018) report the median SAMI/SDSS flux ratio is 1.051 ± 0.005 and the flux ratio rms is 0.10, with 95 per cent of objects having flux ratios within ±0.16 of the median.

The SAMI Galaxy Survey is discussed further in Section 2.1.

1.4 Questions Addressed in This Thesis

This introduction presents many theories and mechanisms of galaxy evolution (and in particular quenching), and discusses how IFS galaxy surveys such as SAMI provide a means to test theories and models. The thesis examines how variations in star formation distribution can serve as a tracer of galaxy evolution and attempts to examine whether the star formation distribution may vary according to the roles of different quenching mechanisms such as stellar feedback, bulge growth or galaxy strangulation. The starting point is how the radial profiles of star formation surface density in galaxies vary according to galaxy properties and by location on (or above and below) the main sequence of star formation. The radial profiles are measured in a SAMI sample of galaxies in mostly low density environments. Galaxies with profiles indicating central suppression of star formation are identified and their frequency in the Local Universe is estimated; their properties (such as bulge/total flux ratio, environmental surface density and other properties) are compared to galaxies without central suppression.

These results are then discussed in relation to various theories of galaxy evolution and galaxy quenching. Of particular interest is whether Local processes occurring at the galaxy centre, or a global process such as strangulation are dominant factors in quenching.

1.4.1 Layout of the Thesis

Chapter 2 addresses methods that are fundamental to all the studies using SAMI observations. It covers the sample selection, the data reduction, and the emission line and continuum measurements in the SAMI galaxy survey, including calculation of SFR and dust correction. It includes additional data products used in this thesis based on the GAMA Galaxy Survey.

Chapter 3 presents the selection criteria for the sub-sample of galaxies defined as 'star forming' selected from the SAMI galaxy survey that is used in this thesis. The distribution of galaxies on the SFR-mass plane is examined, in particular verifying the existence of a 'main sequence' of star forming galaxies. Sub-groups are defined using the measured scatter around the main sequence, being either above, on, below, or well below the main sequence ridge-line, and called Above-MS, MS, Below-MS and Sub-MS sub-groups. The global properties of the star forming sample are explored with respect to the subgroups, using a collection of available photometric and environmental parameters from the SAMI Survey.

Chapter 4 presents radial profiles of star formation for 436 star-forming galaxies, comprising 68 Above-MS galaxies, 317 MS, and 51 Below-MS. The SFR profile shapes are quantitatively explored using a 2-part linear fit, deriving an 'inner' slope (0-0.5 R_e), and an 'outer' slope (0.5-1.5 R_e). From analysis of the inner slope there is identified (using the slope of the radial profile) a subset of galaxies with central suppression of star formation, that is used to consider the significance of central processes in quenching.

Chapter 5 presents a discussion of the findings and conclusions. The discussion focuses on the two main empirical findings, namely the large-scale similarity in the relative distribution of star formation within the sample; and the existence of a subset of galaxies that show a relative suppression of star formation in their central regions, creating a positive ('rising') star formation profile slope. These behaviours are considered in terms of contemporary ideas around the quenching of galaxies.

Chapter 2

METHODS AND DERIVED QUANTITIES

2.1 Introduction

This chapter addresses methods that are fundamental to all the studies using SAMI observations. The methods created within the SAMI team by various investigators produced high-level data products, that were generated in collaboration with me, but I did not lead the development and application of these techniques. This chapter covers the sample selection, the data reduction, and the emission line and continuum measurements in the SAMI galaxy survey, including calculation of SFR and dust correction. It includes additional data products used in this thesis such as galaxy stellar mass, bulge fraction and environmental surface density that are based on the GAMA Galaxy Survey (Liske et al. 2015).

The methods developed or tailored to this study by myself include: the definition of the star formation main sequence, discussed in Section 3.3; and developing radial profiles of star formation and measurement of profile slope in Section 4.3.

The SAMI multiobject integral field spectrograph provides spatially resolved 3D spectroscopy of up to 12 galaxies at a time over a 1° diameter field (Sharp et al. 2015). Seven dithered observations totalling 3.5 hours are taken so there is near-uniform spatial coverage across each of the 13 hexabundles, with the 13th hexabundle on a standard star. The AAOmega data reduction pipeline 2DFDR is used for the standard data reduction (Sharp et al. 2015). 2DFDR performs a standard sequence of tasks for 1D spectral extraction from 2D images, including bias subtraction, flat-fielding, fibre trace (or 'tramline') fitting and wavelength calibration (Hopkins et al. 2013). A spectro-photometric standard star observed during the same night is used for flux correction, while correction for telluric absorption is based on simultaneous observations of a secondary standard star included in the same SAMI plate of the target. Row-stacked spectra of each exposure are generated by 2DFDR and then combined, reconstructed into an image and resampled on a Cartesian grid of $0.5'' \times 0.5''$ spaxel size (Sharp et al. 2015).

2.2 SAMI Survey Sample Selection

The SAMI Galaxy Survey sample consists of two separate but complementary samples with matched selection criteria (Green et al. 2018; Scott et al. 2018): a SAMI-GAMA sample drawn from the Galaxy And Mass Assembly survey (Driver et al. 2011, Figure 1.7) and an additional cluster sample.

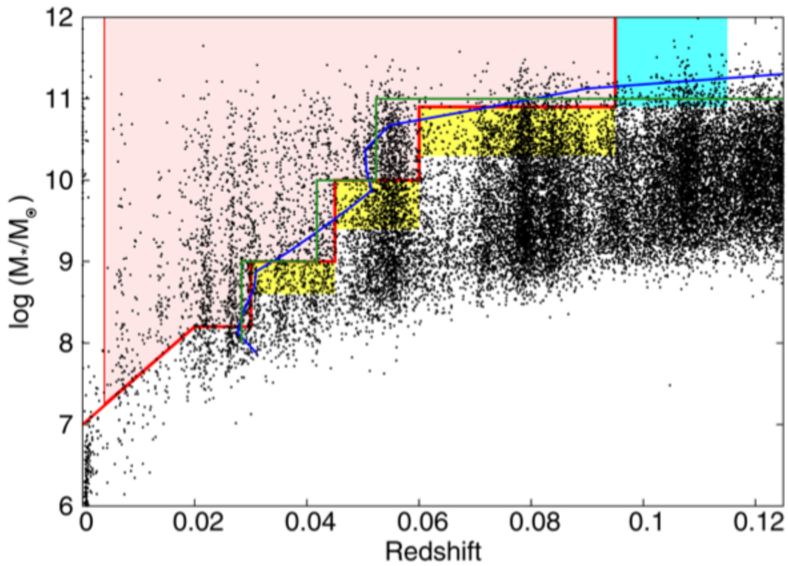

Figure 2.1: *Figure source is Bryant et al. 2015. Stellar mass and redshift (adjusted to the Tonry et al. 2000 flow model) distribution are used to define the selection of SAMI galaxies from the GAMA-I catalogue. Black points are the GAMA catalogue from which SAMI targets were selected. In the final selection, the highest priority targets lie above the red line and within the redshift range z = 0.004-0.095 (pink region). The yellow and cyan boxes represent lower priority targets to be used as fillers in pointings where 12 high-priority targets cannot be optimally tiled within the 1° diameter field.*

In this thesis the galaxy sample is the SAMI Data Release 2 (DR2) SAMI-GAMA sample. The thesis sample (n=1021) does not include the SAMI DR2 additional cluster sample and consists predominantly of galaxies in a low density environment. DR2 galaxies are primarily drawn from three 4 × 12 deg fields of the initial GAMA-I survey, the equatorial

G09, G12, and G15 GAMA I regions (Driver et al. 2011). These regions include galaxies in a range of environments but do not contain any galaxy clusters within the z $\leq$ 0.1 SAMI limit.

Details of the selection process of the SAMI Galaxy Survey sample are described in Bryant et al. (2015), and Owers et al. (2019). The SAMI-GAMA sample consists of a series of volume-limited samples, where the stellar mass limit for each sample increases with redshift (Figure 2.1, Bryant et al. 2015). Stellar masses are estimated from the rest-frame i-band absolute magnitude and $g-i$ colour by using the colour-mass relation following the method of Taylor et al. (2011), assuming a Chabrier (2003) stellar initial mass function (IMF) and exponentially declining star formation histories.

Additional criteria are used to mitigate measurement biases in our sample, and are described as follows:

Inclination: To avoid excessive obscuration of Hα emission by dust lanes, a limit is imposed on the maximum ellipticity (approximately corresponding to inclination for thin disks) of ellipticities >0.7. Ellipticity is obtained from the GAMA Galaxy survey (http://www.gama-survey.org/dr2/tools/sov.php, GAL_ ELLIP_R in the SersicCatAll Table, Sersic Photometry Data Management Unit).

Angular Size: Galaxies are selected with SDSS r- band effective radius (R_e) limits of 0.4 R_e $\leq 7.5'' \leq 4.5$ R_e; this selection helps to avoid beam smearing at higher z and incomplete galaxy sampling at lower z.

The global properties of the galaxy sample of 1021 galaxies, including SFR, galaxy stellar mass, Sérsic n, $g-i$ color, visual morphology, and environmental surface density are presented in the next chapter, Section 3.5.

2.3 Measuring Emission Line Fluxes

LZIFU is an Interactive Data Language (IDL) spectral fitting pipeline that provides flexible emission line fitting in IFS data cubes (Ho et al. 2014). It fits, and then removes the continuum emission in each spaxel using simple stellar population (SSP) models. User-assigned emission line(s) are modeled on a spaxel-to-spaxel basis to produce 2D maps of line fluxes, velocity and velocity dispersion (Ho et al. 2016a, 2016b). The continuum fit is performed with LZIFU using the penalized pixel-fitting routine, pPXF (Cappellari & Emsellem 2004) and returns a Gaussian fit to the emission lines using the mpfit algorithm (Markwardt 2009). After removing the continuum, LZIFU models emission lines as Gaussians and performs a bounded-value nonlinear least-squares fits using the Levenberg-Marquardt least-squares method implemented in IDL (Markwardt 2009). The 11 strong optical lines are fit simultaneously, [O II]$\lambda\lambda$3726,3729, Hβ, [O III]$\lambda\lambda$4959,5007, [OI]λ6300, [N II]$\lambda\lambda$6548,83, Hα, and [S II]$\lambda\lambda$6716,31.

The outputs of LZIFU are emission line cubes, emission line flux (and corresponding error) maps, continuum cubes, and velocity and velocity dispersion maps stored in multi-extension FITS files. The [O II]$\lambda\lambda$3726,3729 doublet is summed because the blue spectral resolution makes an independent measurement of the components impractical. The blue resolution is R = 1700; and red is R= 4500.

The emission line flux maps are used to classify each spaxel using [O III]/Hβ, [N II]/Hα, [S II]/Hα, and [O I]/Hα flux ratios to determine whether the emission lines are dominated by photoionization from H II regions or other sources like AGN or shocks. The Baldwin, Phillips, & Terlevich (1981) diagnostic diagrams and dividing lines from Kewley et al. (2006) are used to classify spaxels as star-forming if the following three conditions are all met:

log([OIII]/Hβ)<(0.61/(log([NII]/Hα)-0.05)+1.3   (Kauffmann et al. 2003b)

log([OIII]/Hβ)<(0.72/(log([SII]/Hα)-0.32)+1.3   (Kewley et al. 2001)

log([OIII]/Hβ)<(0.73/(log([OI]/Hα)+0.59)+1.33   (Kewley et al. 2001)

Only spaxels with ratios that have a signal-to-noise ratio of at least 5 are classified. The implementation of LZIFU to SAMI data is further discussed in Green et al. (2018).

2.4 Adaptive Binning

Galaxy surface brightness decreases significantly from the central parts of the SAMI hexabundle to the outer edge of the field (typically sampling beyond 1 effective radius of most galaxies). In order to maintain a high-quality continuum (and subsequent emission-line) fit, the outer spaxels must be co-added to meet a minimum signal-to-noise ratio (S/N). An adaptive spatial binning scheme using a Voronoi tesselation is used (Cappellari & Copin 2003), with a target continuum S/N=10. The covariance between neighbouring spaxels is carefully accounted for in this binning process (Sharp et al. 2015).

2.5 Calculation of Star Formation Rate and Dust Corrections

In SAMI galaxies studies the SFR of a galaxy is generally determined using Hα emission. The nebular Hα recombination line is a widely used tracer of recent star formation; the current star formation of a galaxy can be calculated from the Hα luminosity as this emission gives a direct probe of the young massive stellar population (Kennicutt 1998). The emission arises from recombination of gas ionized by photons from massive stars ($\geq$15 $M_\odot$) and is expected to be observed over the typical lifetimes ($\leq$5 Myr) of extremely massive stars (Weisz et al. 2012).

Balmer extinction maps (called Balmer Decrement Attenuation Correction or BDAC) are available on the SAMI website[1] (Green et al. 2018). They are calculated from the Balmer Decrement (BD) and the Cardelli et al. (1989) extinction law.

For each spaxel:

$$\mathrm{BD} = \frac{\mathrm{H}\alpha}{\mathrm{H}\beta} \tag{2.1}$$

$$\delta\mathrm{BD} = \mathrm{BD} * \left[\left(\frac{\delta\mathrm{H}\alpha}{\mathrm{H}\alpha}\right)^2 + \left(\frac{\delta\mathrm{H}\beta}{\mathrm{H}\beta}\right)^2\right]^{0.5} \tag{2.2}$$

$$\mathrm{BDAC} = \left(\frac{\mathrm{BD}}{2.86}\right)^{2.36} \tag{2.3}$$

.

The exponent in the dust obscuration correction factor (2.36) is calculated:

$$\frac{k(\lambda_{H\alpha})}{k(\lambda_{H\beta}) - k(\lambda_{H\alpha})} \tag{2.4}$$

.

k(λ) at a given λ is determined from the Cardelli, Clayton & Mathis (1989) galactic dust extinction curve, derived from observations of the UV extinction of stars. The extinction curves have been verified in studies of the obscuration of the ionized gas in star-forming galaxies (Calzetti 2001; Gunawardhana et al. 2011). This approach implicitly models the dust as a foreground screen averaged over the galaxy (Calzetti 2001).

$$\delta\mathrm{BDAC} = \left[\frac{\mathrm{BDAC} \times 2.36 \times \delta\mathrm{BD}}{\mathrm{BD}}\right] \tag{2.5}$$

The δ terms indicate the standard error on the quantity. The BDAC maps are in units

[1]http://datacentral.aao.gov.au/asvo/schema-browser/sami/extinction_map/

of attenuation correction factor - such that a BDAC map may be multiplied by the SAMI Hα cube to obtain de-extincted Hα cubes. BD values of less than 2.86 imply that the Hβ lines are brighter than expected for the typically assumed "Case B" recombination. No dust correction is applied to bins with BD<2.86.

The BDAC maps set to NaN the correction and error for spaxels with Hα flux ($f_{H\alpha}$ > 40 $\times$ $10^{-16} ergs^{-1}cm^{-2}$ and Balmer decrement > 10. These numbers help eliminate spurious Hα fits to the edges of the fibre bundles.

Following Kewley et al. (2006) an intrinsic H_α/H_β ratio of 2.86 is used for galaxies dominated by star formation and Hα/Hβ = 3.1 for galaxies dominated by AGN (the Balmer decrement for case B recombination at T = 10^4 K and $n_e \sim 10^2 - 10^4 cm^{-3}$, where n_e is the number density of electrons (Osterbrock & Ferland 2006)). Galaxies with AGN are excluded from the thesis sample as discussed in Section 2.7.

The corrected H_α luminosity is then:

$$LH\alpha(W) = 4\pi d_L^2 f_{H\alpha}(BDAC) \tag{2.6}$$

where d_L is the luminosity distance in centimetres.

The SFR is calculated from the dust corrected H_α luminosity using the Kennicutt (1998) relation with a Chabrier (2003) IMF:

$$\text{SFR} = L(H\alpha) \times \frac{7.9}{1.53} \times 10^{-42} M_\odot yr^{-1} \tag{2.7}$$

The flux values in the SAMI LZIFU release datasets are in units of

10^{-16} $erg\ s^{-1}cm^{-2}\text{Å}^{-1}spaxel^{-1}$, and the variance in the same units squared (Allen et al. 2015).

2.6 Photometric Properties

2.6.1 Galaxy Stellar Mass

Galaxy stellar masses are taken from the GAMA Galaxy Survey (Liske et al. 2015). In GAMA, a combined approach using both absolute magnitudes and colours to calculate a proxy for stellar mass is adopted. The method follows Taylor et al. (2011), with photometry based on SDSS (DR7) optical imaging (Abazajian et al. 2009). The GAMA survey stellar masses generated by optical SED fitting are:

$$log(M_*)/[M_\odot] = 1.15 + 0.70(g - i)_{rest} - 0.4M_i \quad (2.8)$$

where M_i is the AB rest-frame i-band magnitude. In the SAMI survey observed-frame extinction- corrected apparent magnitudes (g and i) (with colours limited to reasonable values of $-0.2 < g - i < 1.6$) are used (Bryant et al. 2015) with the stellar mass:

$$\begin{aligned} log(M_*)/[M_\odot] = &-0.4i + 0.4D - log10(1.0 + z) \\ &+ (1.2117 - 0.5893z) + (0.7106 - 0.1467z) \times (g - i) \quad (2.9) \end{aligned}$$

where D is the distance modulus and z is redshift.

2.6.2 Bulge-disk decompositions

The SAMI Galaxy Survey bulge-disk decompositions are a subset of GAMA BDDecomp Data Management Unit (DMU). This DMU led by Sarah Casura provides single Sersic and two-component bulge-disk fits to the 2D surface brightness distribution in the KiDS r-band for a selected sample of 13096 galaxies with z < 0.08 in the GAMA II equatorial survey regions using the surface photometry package ProFit (Robotham et al., 2018).

The bulge fraction is available for most SAMI galaxies via collaboration with the GAMA Survey II (Kennedy et al. 2016). The SAMI version is identical to the full GAMA version of the DMU except that all tables have been restricted to the SAMI sample. It contains 2 catalogues: "BDInputs", with the most important outputs of the preparatory work pipeline (segmentation, PSF estimation, initial guesses); and "BDModelsAll", with the output from the actual galaxy fitting and post-processing (model selection and flagging of bad fits). This thesis uses the "BDModelsAll" catalogue, and uses bulge-to-total flux ratio as an indicator of bulge size.

The galaxy modelling is done using ProFit, the Bayesian two-dimensional surface brightness profile fitting code of Robotham et al. (2018) fitting 3 models to each galaxy: a single-Sérsic, a Sérsic + exponential and a point source + exponential. These authors emphasise ‘that important principles’ for achieving a good fit are: a pixel-matched error map (reflecting the local uncertainty in the image provided); a segmentation map that flags the pixels to use when computing the fit likelihoods; a careful sky subtraction;

and reasonable initial guesses for the profile parameters (e.g. finding objects, generating segmentation maps, etc.). The preparatory work is carried out using the sister package ProFound, with the PSF estimated by fitting nearby stars using a combination of ProFound and ProFit.

2.6.3 Environmental Surface Density

The local environment of galaxies is measured using the nearest-neighbor surface density to probe the underlying density field (Brough et al. 2017). Galaxies with closer neighbors are in denser environments and the nearest-neighbor measurement can be refined to an overdensity that parametrizes whether galaxies are in an environment that is more or less dense than the average in a given sample.

The SAMI-GAMA Environment-Measures catalogue provides three different metrics of the local environment of GAMA II galaxies in the equatorial survey regions. The catalogue may be accessed on the GAMA Galaxy Survey website [2]. The metrics are surface density, the number of galaxies within a cylinder, and the adaptive Gaussian environment parameter. This thesis uses surface density as an index of environmental density.

The three environment measurements are performed on a density defining pseudo-volume-limited population of galaxies. This population is defined as all galaxies with M_*r*(z_ref=0, Q=1.03) < -18.5 mag, where Q defines the expected evolution of M_*r* as a function of redshift. Q is taken from Loveday et al. (2015).

Given the depth of the GAMA II survey (r < 19.8 mag) the above absolute magnitude limit implies a redshift (i.e. volume) limit of z=0.103. However, in order to account for the upper edge of the velocity range employed when searching for nearby galaxies (see below), the environment measurements are only provided for galaxies out to z = 0.1.

Included in this catalogue are all galaxies in the GAMA II completeness masks with redshift quality nQ > 2 (i.e. reliable redshifts) and within the redshift limits of 0.002 < Z < 0.1.

This catalogue is based on GAMA II catalogues Distances_Frames_v12, kCorrectionsv04, and the GAMA II completeness masks, and assumes the cosmological parameters $H_0 = 70\,\text{km/s/Mpc}$, $\Omega_M = 0.3$, $\Omega_\Lambda = 0.7$.

The "surface density" column provides the surface density Σ_5 in Mpc^{-2} based on the

[2] http://www.gama-survey.org/dr3/data/cat/EnvironmentMeasures/v05/EnvironmentMeasures.notes

distance to the 5th nearest neighbour (r_5) among the density defining population in a velocity cylinder of ±1000 km/s:

$$\Sigma_5 = \frac{5}{\pi \times (r_5)^2}. \tag{2.10}$$

2.6.4 Galaxy Color and Sérsic *n*

Galaxies of different morphologies (e.g. disk, spheroidal, or a combination) exhibit different characteristic light profiles, quantified by the azimuthally averaged radial profile of their surface brightness. This profile can be well approximated using the so-called Sérsic function (Sérsic 1963, 1968).

$$I(r) = I_e \exp\left[-b\left(\left(\frac{r}{r_e}\right)^{1/n} - 1\right)\right] \tag{2.11}$$

The Sérsic equation provides the intensity I at a given radius r as given by Equation 1 in Kelvin et al. (2014), where I_e is the intensity at the effective radius r_e, the radius containing half of the projected total light, and n quantifies the characteristic gradient of the light profile - referred to as the Sérsic index. The value of b_n is a function of Sérsic index, as defined in Ciotti (1991), and is such that $\Gamma(2n) = 2\gamma(2n, b_n)$, where Γ and γ represent the complete and incomplete gamma functions respectively.

The Sérsic index reflects the shape of the galaxy light profile and single-Sérsic model fits have been shown to provide a good description of light profiles as faint as B $\sim$ 28 mag arcsec^{-2} (Caon, Capaccioli & D'Onofrio 1993, Kelvin et al. 2014).

Optical colors were measured from aperture-matched photometry presented in Liske et al. (2015), using images from the Sloan Digital Sky Survey (SDSS) DR7 data release (Abazajian et al. 2009) convolved to a common PSF. Both $g - i$ color and Sérsic n have been obtained for each galaxy in the sample using published data from the GAMA Galaxy Survey (Liske et al. 2015).

2.7 Galaxy Classification as SF, AGN/LINER and AGN_Composite

Galaxies are classified as either star-forming, composite or AGN/LINER using their emission line ratios in the central 2″ to determine their location on the Baldwin, Phillips, & Terlevich (1981) diagram (Figure 2.2). In Baldwin-Phillips-Terlevich (BPT) diagrams the relative strengths of certain prominent emission lines are used to probe the conditions within nebular gas and determine the source of excitation, which broadly falls into two categories: stellar photoionization, or photoionization by a centrally located, spectrally hard radiation field, such as produced by the accretion disk of a massive black hole (Kewley et al. 2006, and references therein). It is argued the optical spectra of H II regions and starburst nuclei have very weak low-ionization transitions [N II], [S II], and [O I]; by contrast AGN create an extensive partially ionized zone with strong low-ionization forbidden lines (Ho 2008). The harder radiation field of an AGN power-law continuum extends into the extreme ultraviolet (UV) and X-rays so it penetrates much deeper into an optically thick cloud to produce the strong low-ionization transitions.

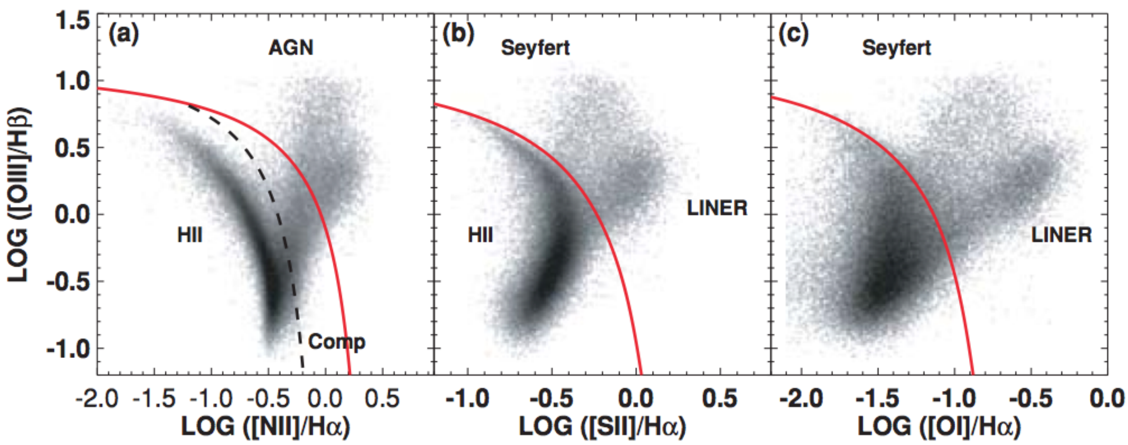

Figure 2.2: *Figure from Kewley et al. (2006). BPT Diagrams for Emission Line Classification. The Ke01 line is the red solid line in the left panel and it is determined by the upper limit of the theoretical pure stellar photoionization models.*

The emission line classification as described in Kewley et al. (2006) is employed. BPT diagrams are based on the four optical line ratios [O III]/Hβ, [N II]/Hα, [S II]/Hα, and [O I]/Hα displayed in Figure 2.2. Kewley et al. (2001) created a theoretical 'maximum starburst line' called Ke01 on the the BPT diagrams using a combination of stellar population synthesis models and photoionization models. The Ke01 line is the red solid line in Figure 2.2 and it is determined by the upper limit of the theoretical pure stellar photoionization models. Galaxies lying above this line are classified AGN. Kauffmann et al. (2003b) added an empirical line hereafter referred to as Ka03 (the dashed line in Figure 2.2) to divide pure star-forming galaxies from Seyfert-H II composite objects whose spectra contain significant contributions from both AGN and star formation.

I have created BPT diagrams using my own python code for all galaxies, and my results generally agree with the SAMI team classification of galaxies into SF and AGN;

for selecting the sample in the thesis I have used the team classification, as described in Schaefer et al. (2017).

2.8 Statistical Tests

2.8.1 Spearman Correlation

(These notes have drawn upon the Scientific Python Reference Guide [3]). The Spearman correlation is a nonparametric measure of the relationship between two datasets. The correlation coefficient varies between -1 and +1 with 0 implying no correlation. Correlations of -1 or +1 imply an exact monotonic relationship; Spearman Correlation is said to measure monoticity. Positive correlations imply that as x increases, so does y.

The Spearman correlation does not assume that both datasets are normally distributed. The p-value indicates the probability of an uncorrelated system producing datasets that have a Spearman correlation at least as large as the one computed from these datasets. The p-values may not be entirely reliable for small sample sizes under 500.

2.8.2 Kolmogorov-Smirnov Test

(These notes have drawn upon the Scientific Python Reference Guide [4]).

The 2-sample Kolmogorov-Smirnov Test (K-S Test) tests whether 2 samples are drawn from the same distribution. In other words it allows one to reject the possibility that the two samples are coming from the exact same distribution. The K-S test is only valid for continuous distributions.

[3] https://docs.scipy.org/doc/scipy-0.14.0/reference/generated/scipy.stats.spearmanr.html
[4] https://docs.scipy.org/doc/scipy-0.14.0/reference/generated/scipy.stats.ks_2samp.html

Chapter 3

SAMPLE DEFINITION AND GLOBAL PROPERTIES

3.1 Introduction

This chapter explores the global properties of the star-forming galaxies in the SAMI sample. Firstly, the selection of a subsample of star-forming SAMI galaxies is described, which is then used to form a relationship between galaxy mass and star formation rate (SFR). Additional subgroups of this star-forming sample are defined with respect to the principal locus of galaxies which form the so-called 'main sequence' of star-forming galaxies. Distribution of global galaxy properties within these subgroups are then explored. These subgroups are also used in Chapter 4, which presents analysis of the spatially resolved star formation properties of the star-forming sample.

3.2 Star-Forming Galaxy Sample Selection

To focus on the behaviour of star formation within the SAMI sample, a reference sample of star-forming galaxies is selected using a consistent set of selection criteria to avoid certain observational biases. Starting from the parent SAMI sample, as described in Section 2.2, the following selection criteria are applied:

- Galaxies must have suitable emission lines measurable within a central 2" diameter aperture that meet the S/N requirements for the classification method described in Section 2.7. Only spaxels with ratios that have a signal-to-noise ratio of at least 5 are classified.

- the maximum ellipticity (approximately corresponding to inclination for thin disks) of ellipticities >0.7.

- Galaxies are selected with SDSS r- band effective radius (R_e) limits of 0.4 R_e $\leq$7.5″$\leq$4.5 R_e.

These selection criteria give the final sample of 1021 star-forming galaxies that will be used in the subsequent analysis presented in this thesis.

The galaxy sample of 1021 galaxies used in this thesis is introduced in Figure 3.1, plotted on the stellar mass-star formation plane, with coding by galaxy visual morphology. The definition and discussion of the visual morphology is presented in Section 3.3.

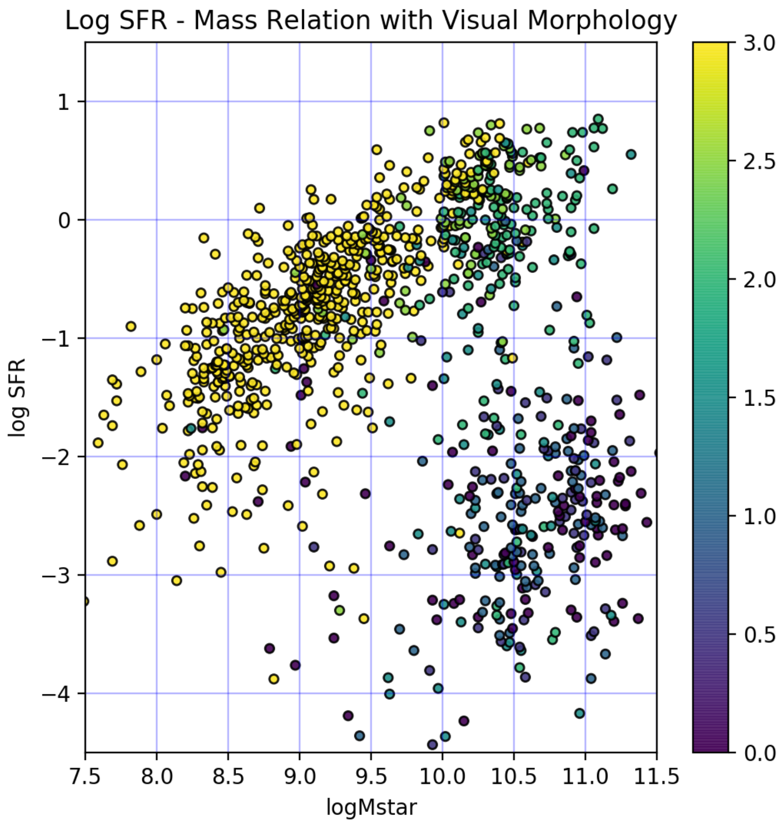

Figure 3.1: *The galaxy sample is plotted on the stellar mass-star formation plane with SFR presented in* $M_{\odot} yr^{-1}$. *The 1021 galaxies of the thesis sample are color coded according to this scale: Morphological Type (0=E; 0.5=E/S0; 1=S0; 1.5=S0/Early-spiral; 2=Early-spirals; 2.5=Early/Late spirals; 3=Late spiral.)*

3.3 Defining the Star Formation Main Sequence

The relationship between star formation rate (SFR) and stellar mass in galaxies is a key observational property established from local (Brinchmann et al. 2004) and high-redshift

(Daddi et al. 2007, Elbaz et al. 2007, Noeske et al. 2007) surveys. The precise shape and slope of this relationship is influenced by selection effects. Rather than a simple linear (in log-log terms) correlation, the relationship is defined by an approximately linear locus of galaxies, the so-called 'main sequence', with an asymmetric spread around this locus to include a tail of lower SFR galaxies. The slope and scatter of the main sequence is relatively constant out to redshift ~ 2 or beyond (Whitaker et al. 2014), varying mainly in normalisation, in line with the evolution of cosmic star formation rate density (Madau & Dickinson 2014). The main sequence therefore defines a useful reference point on the SFR-mass plane from which to compare galaxy star formation properties while accounting for the increased SFR at higher galaxy mass.

As illustrated in Figure 3.2, a well-defined sequence only exists for galaxies with a prominent disk. The figure compares linear fits to the SAMI star-forming sample that result from different morphological selections. This highlights the importance of sample selection on the main sequence definition. In an effort to mitigate issues related to sample selection effects, Renzini & Peng (2015) defined the main sequence as the ridge-line of galaxy number density on the SFR-mass plane using SDSS data, resulting in the following definition (red line in Figure 3.2):

$$\log(\mathrm{SFR}) = (0.76 \pm 0.01)\log(M_*/M_\odot) - 7.64 \pm 0.02. \tag{3.1}$$

This compares well with line fitted to only the SAMI galaxies with morphological class 2.5 or higher (Early-/late- and late-type spirals), which has a slope of 0.82 and an intercept of -8.22. In this thesis, the definition of Renzini & Peng (2015) is used, in part for consistency with other studies, and also given the larger sample used to establish the relation (240,000 galaxies, vs. <1,000).

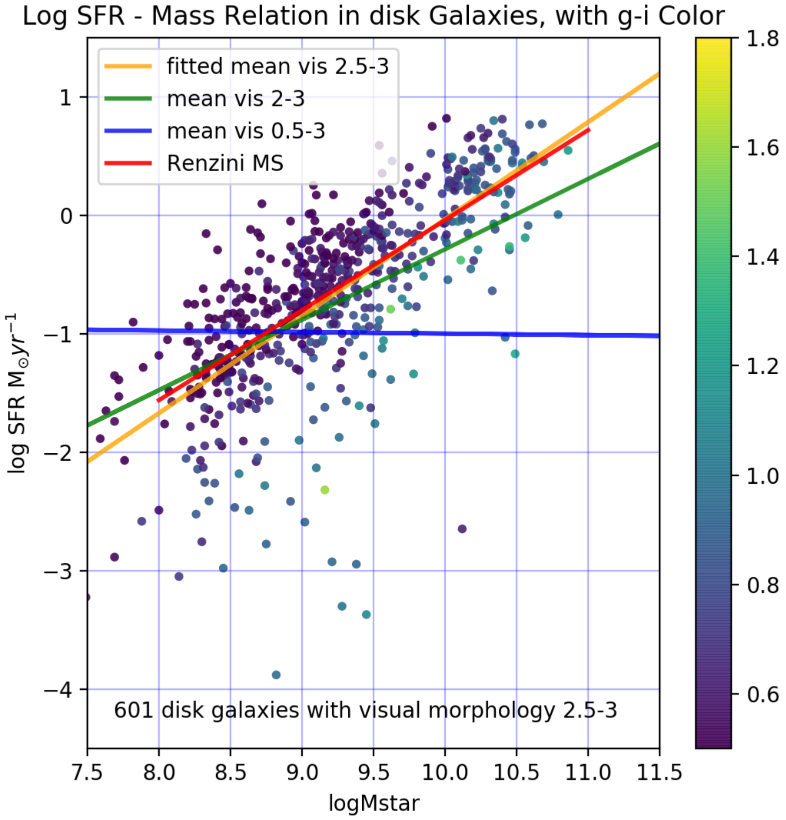

Figure 3.2: *Only galaxies with a visual morphology of 2.5 - 3 are shown (n=601). A ridgeline is fitted to the 601 galaxies with the orange line, while the red, green and blue lines are overlays. The orange line has a slope and intercept similar to the SDSS sample of Renzini and Peng (2015), the red line. If early spirals (type=2) are included in the fit the slope is reduced as shown by the overlaid green line, and if S0/early spiral types (type 1.5) are included the slope is reduced further as shown by the overlaid blue line.*

A main sequence ridgeline (the orange line in Figure 3.2) is identified by selecting disk galaxies based on their morphology (types 2.5-3). The main sequence only exists for star forming galaxies with disks. The slope of the MS ridgeline depends on the selection of galaxies by morphology and it varies as shown in Figure 3.2 where the inclusion of some early type galaxies (vis 2 or below) has a big effect on the slope. In this way visual morphology plays a role in determining the slope of the ridgeline. The visual morphology of the galaxies was performed by a SAMI working group on visual morphology consisting of 14 members. Visual classification on either SDSS DR9 or VST RGB images is done using a classification scheme consistent with one used by the earlier GAMA survey (Kelvin et al. 2014). The method is described in Cortese et al. (2016), and (a) decides whether the galaxy is an early- or late-type system according to the presence/absence of disk/spiral structures and signs of star formation, and (b) determines if distinct structural components (i.e., bulge/disk) in the galaxy are present.

The fitted orange line (visual morphology type 2.5-3) in Figure 3.2 has a slope 0.82 and an intercept of -8.22, thus

$$\log(\mathrm{SFR}) = 0.82 \times log(M_*/M_\odot) - 8.22. \tag{3.2}$$

In this thesis the ridgeline of Renzini and Peng (2015) (the red line in Figure 3.2) expressed in Equation 3.1 is called the main sequence and used in dividing the sample of galaxies into groups.

3.4 Defining Groups of Galaxies Around the SFR Main Sequence

The scatter of the thesis sample galaxies around the main sequence (MS) is quantified by the standard deviation, σ, of distances of each galaxy from the main sequence at the same mass. One standard deviation corresponds to 0.417 exponential degrees. Lines that are 1 σ above (blue line) in Figure 3.3 and below (red line) the ridgeline, and a third line 4 σ below the ridgeline (magenta line) are drawn to define the 4 categories (Above-MS, MS, Below-MS, and a fourth category way-below or Sub-MS).

Thus four groups are defined in Figure 3.3:

- **Group 1, Above-MS**: These galaxies lie above the main sequence by more than one standard deviation on the fiducial relation.

- **Group 2, MS**: These galaxies lie on the relation within +/- the standard deviation.

- **Group 3, Below-MS**: These galaxies lie below the main sequence by more than one standard deviation on the fiducial relation, but within 4 standard deviations. We consider this group to represent galaxies where quenching of star formation may be in progress, but not fully complete.

- **Group 4, Sub-MS**: These galaxies lie below the main sequence by more than 4 standard deviations. We refer to these galaxies as ‘quenched’, but they may be more accurately considered as ‘near quenched’, as they still exhibit measurable Hα emission. Only a small proportion of the Sub-MS galaxies are able to have radial profiles of star formation with the various fits, as discussed in the next chapter.

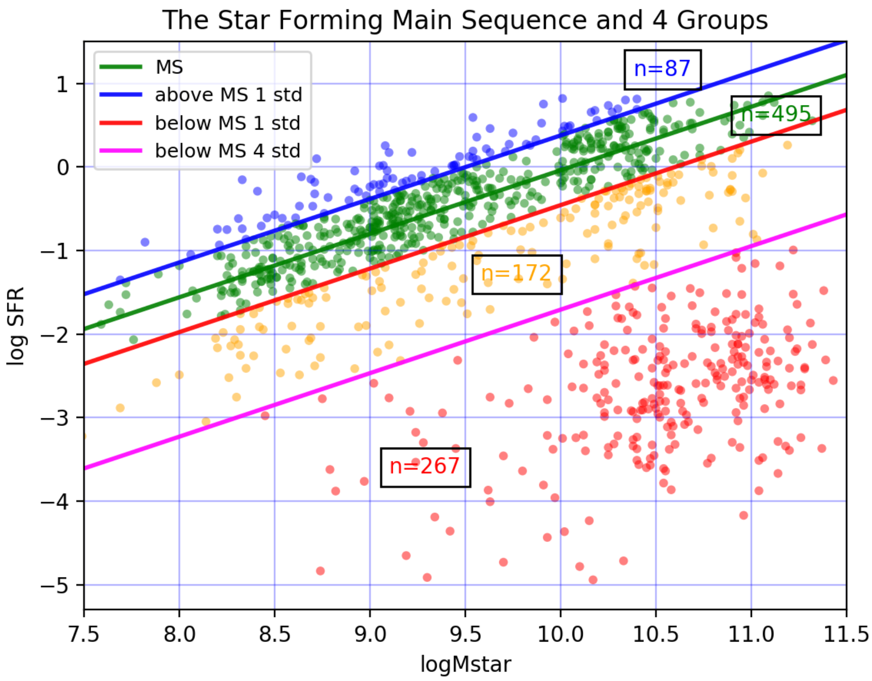

Figure 3.3: *Galaxies are divided into 4 groups (Above-MS, MS, Below-MS, Sub-MS using lines 1 σ above and below the green main sequence ridgeline). The lowest magenta line is 4 σ below the green line.*

3.5 Global Properties of Galaxies in Groups

Before considering the spatial distribution of star formation properties, presented in the following chapter, it is first instructive to consider the distribution of global galaxy parameters within the different SFR subgroups defined in the previous section. Note that not all galaxies in this star-forming sample have their global parameters consistently measured at the time of writing, therefore care must be taken in interpreting the relative fractions of objects within and between the various groups. However, it is still instructive to consider these distributions for context of the sample. The following properties are considered:

- Optical colour
- Visual morphology
- Sérsic index
- Bulge-to-total flux ratio
- Environmental surface density

For each of these properties, their distribution within the SFR-subgroups is considered via cumulative distribution plots and Kolmogorov-Smirnov (KS) tests.

3.5.1 Visual Morphology

Striking differences in visual morphology are apparent between galaxies on or above the MS, and those below it, and between high-mass and low-mass galaxies. The visual morphology (left pane) and $g - i$ color (right pane) of the 4 groups are presented in Figure 3.4. The relationships portrayed in the 2 plots for galaxy stellar mass, SFR, visual morphology and $g - i$ color are well-established and are presented here in order to illustrate the galaxy sample. There is a dearth of galaxies in the Sub-MS (group 4) group of log stellar mass < 9.5 or 10 (Figure 3.4, left pane), and this may reflect the finding that field galaxies in this mass range are reported to be star-forming (Geha et al. 2012; Medling et al. 2018) where a field galaxy is defined as having a distance from a massive galaxy or cluster >1.4 Mpc. Quenched galaxies below log stellar mass 9.5 or 10 are expected to have a massive neighbour, thus Davies et al. (2015) find that essentially all passive galaxies with log stellar mass < 8.5 are found in pair/group environments.

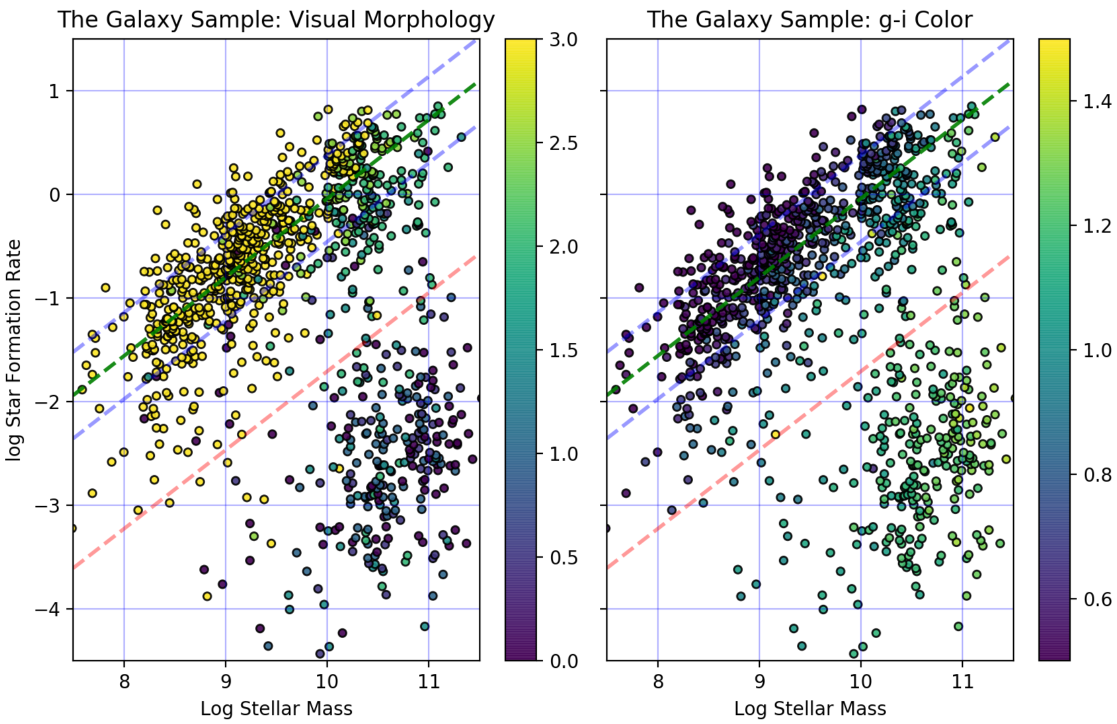

Figure 3.4: *The galaxy sample (n=1021) in four groups showing the visual morphology (left pane) and g-i color in magnitudes (right pane). Near the MS, galaxies tend to be blue as an indicator of the young stellar content. In the Sub-MS group of galaxies below the red line, there are relatively few of low mass (log stellar mass < 9.5 or 10).*

The distribution of visual morphology in the Above-MS, Below-MS and Sub-MS groups are compared to the MS group.

Comparing MS and Sub-MS: KS Test statistic = 0.2477, p value = 2.557e-8

Comparing MS and Below-MS: KS Test statistic= 0.2880, p value =1.532-7

Comparing MS and Above-MS: KS Test statistic= 0.2009, p value =0.018.

3.5.2 $g - i$ Color

The $g - i$ colour is used as an indicator of the general stellar population properties of the galaxies, with bluer/redder galaxies indicating the possible presence of young/old stellar populations respectively. While susceptible to dust effects, the $g - i$ colour sets the galaxy sample in context with the general 'red sequence' and 'blue cloud' populations from studies of galaxy colour and magnitude (e.g. Baldry et al. 2004).

The distribution of $g - i$ color in the Above-MS, Below-MS and Sub-MS groups are compared to the MS group.

Comparing MS and Sub-MS: KS Test statistic = 0.3048, p value = 1.068e-14

Comparing MS and Below-MS: KS Test statistic= 0.4917, p value =1.153e-23

Comparing MS and Above-MS: KS Test statistic= 0.3889, p value =1.491e-8.

3.5.3 Sérsic Index

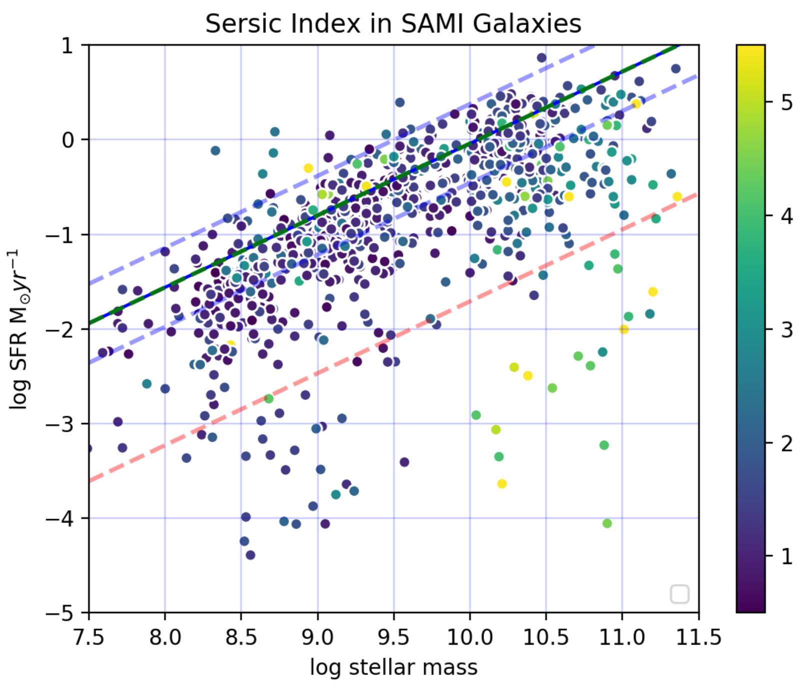

Figure 3.5: *The galaxy sample (n=808) with each galaxy color-coded by the Sérsic Index.*

The Sérsic index is monotonically related to the central galaxy light concentration (Trujillo et al. 2001), providing a measure of continuum light concentration; it has been used to differentiate between early-type and late-type galaxies, for example Cheung et al. (2012) reported Sérsic n = 2.3 divides the red sequence from the blue cloud. In Figure 3.5 the green and yellow galaxies (Sérsic n >2.3) are concentrated at higher masses and below the MS, and there are more n>2.3 galaxies in the Sub-MS group.

Sérsic index values are higher in the Below-MS group compared to the MS: KS Test statistic= 0.3514, p value=1.247e-10.

3.5.4 Bulge-to-total Flux Ratio

The presence of a bulge is of key importance in galaxy classification (Section 3.3), and bulge-disk decompositions with measurements of flux ratios are undertaken to assess the significance of bulges (Graham & Worley 2008, Kennedy et al. 2016).

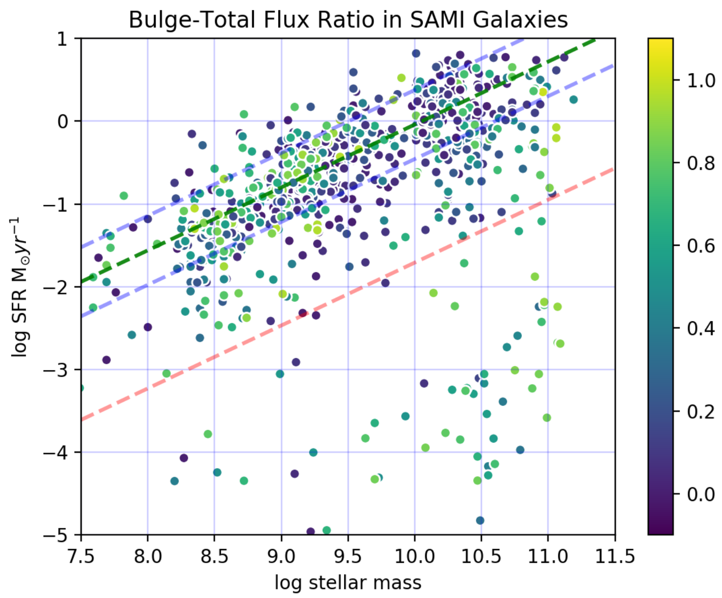

Figure 3.6: *The galaxy sample (n=742) in four groups with the color presenting the bulge-to-total flux ratio.*

The bulge-to-total flux ratio values are available for most SAMI galaxies due to collaboration with the GAMA Survey II (Kennedy et al. 2016), as discussed in subsection 2.6.2, and are here used to provide an indicator of bulge presence and size.

The galaxy sample in four groups showing the bulge-to-total flux ratio is presented in Figure 3.6. The Sub-MS group below the red line has higher flux ratio values, and the Below-MS group has higher values than the MS and Above-MS groups.

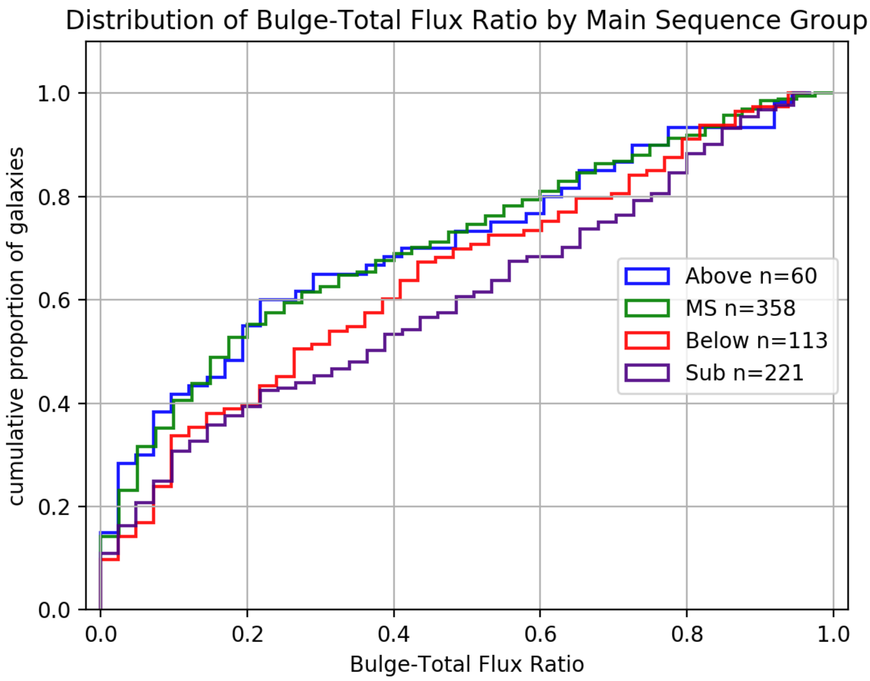

Figure 3.7: *The cumulative histogram of the bulge-to-total flux ratio values shows the Sub-MS and the Below-MS group have higher values than the MS group.*

The cumulative histogram of the bulge-to-total flux ratio values (Figure 3.7) shows the Sub-MS group has higher values than the other groups. The Below-MS group is also has higher values than the MS group, but the result is significant only at the p=0.04 level.

Comparing MS and Sub-MS: KS Test statistic = 0.1773, p value=0.0003

Comparing MS and Below-MS: KS Test statistic= 0.1475, p value=0.0428

3.5.5 Environmental Surface Density (ESD)

The index of environmental density used is surface density in Mpc^{-2} as described in Section 2.6.3, based on the distance to the 5th nearest neighbour.

The values of surface density in Mpc^{-2} are plotted on a M-SFR scatter plot, Figure 3.8. Most galaxies have a low ESD (log ESD -1 to 2) consistent with field galaxies. This is expected as the SAMI 'GAMA fields' on which my thesis sample is based lacks galaxies in large clusters and consists mainly of field galaxies. A histogram of ESD values by group (Figure 3.9) is performed to study any association of ESD, and the galaxy location on, above or below the main sequence.

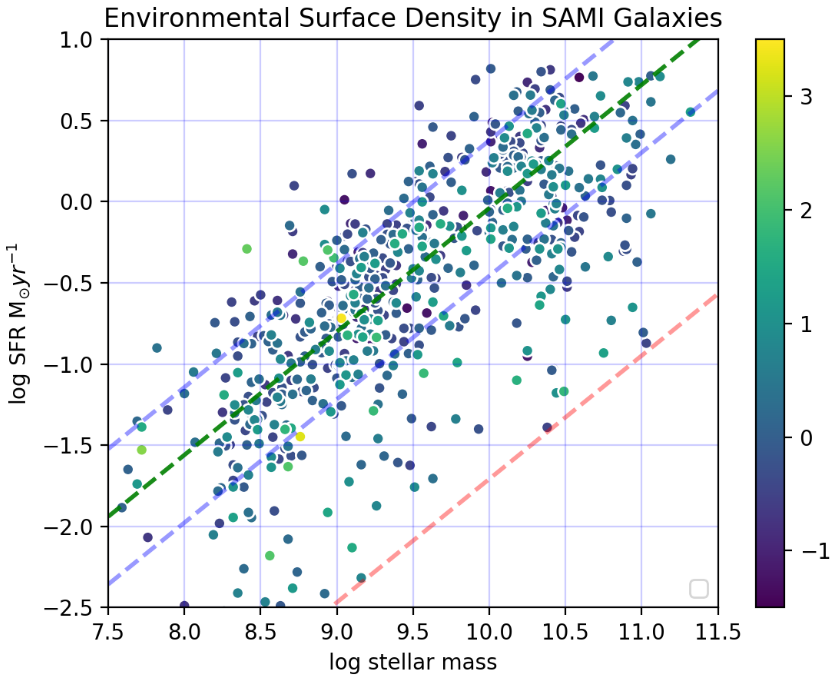

Figure 3.8: *The 628 galaxies with environmental surface density (ESD) in Mpc^{-2} are shown with the log ESD color coded. No clear association of location in relation to the Main Sequence and ESD is found.*

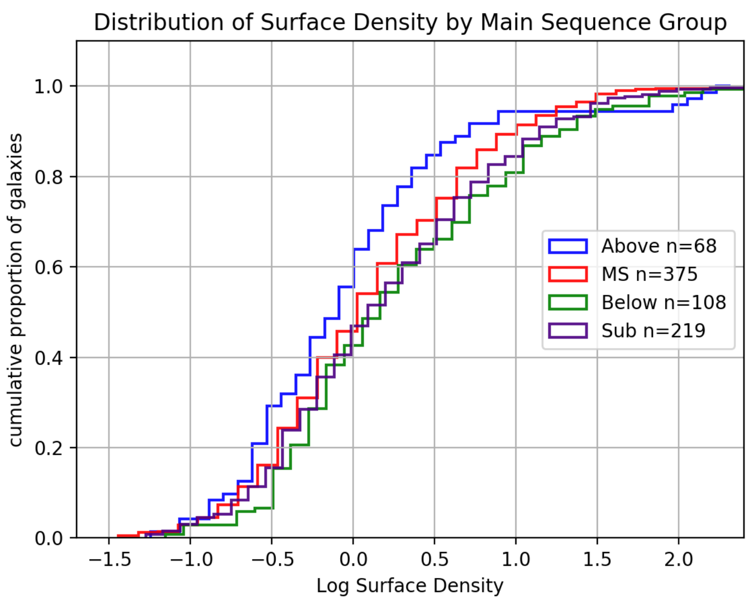

Figure 3.9: *The cumulative histogram of the log environmental surface density values shows the Below-MS group may have higher values than the Above-MS and MS groups.*

The Above-MS group has significantly lower ESD values compared to the Below-MS group, KS statistic=0.221, p-value=0.017; there was not a significant difference for the Above-MS to MS comparison, or the MS to Below-MS comparison.

3.6 Galaxy Characteristics: Discussion and Conclusions

This chapter presents the selection criteria for the sub-sample of galaxies defined as 'star-forming' selected from the SAMI galaxy survey that is used in this thesis. This sample is used to explore the distribution of galaxies on the SFR-mass plane, in particular verifying the existence of a 'main sequence' of star-forming galaxies.

Using the main sequence defined by Renzini & Peng (2015), sub-groups are defined using the measured scatter around the main sequence, being either above, on, below, or well below the main sequence ridge-line, and called Above-MS, MS, Below-MS and Sub-MS sub-groups. The global properties of the star forming sample are explored with respect to the sub-groups, using a collection of available photometric and environmental parameters from the SAMI Survey. The outcomes can be summarised as follows:

- **Visual Morphology:** There are striking differences in visual morphology apparent between galaxies on or above the MS, and those below it, and between high-mass and low-mass galaxies. This pattern is replicated with other indicators, as expected galaxies with properties consistent with early type galaxies (including high g-i color, high Sérsic n, high bulge-to-total flux ratio) are located at higher masses and below the star formation MS.

- **Optical colour:** The $g - i$ colour is used as an indicator of the general stellar population properties of the galaxies, with bluer/redder galaxies indicating the possible presence of young/old stellar populations respectively. As expected the galaxies above the MS are bluer, and those below the MS are redder compared to MS galaxies.

- **Sérsic index:** The galaxies with Sérsic n >2.3 are concentrated at higher masses and are located in the Below-MS and Sub-MS groups.

- **Bulge-to-total flux ratio:** The Sub-MS group has higher flux ratio values than the other groups. The Below-MS group is also has higher values than the MS group, but the result is significant only at the p=0.04 level.

- **Environmental surface density:** The SAMI 'GAMA fields' on which the sample is based lacks large clusters and consists mainly of field galaxies. As expected most galaxies have a low environmental surface density (ESD), a log ESD of -1 to 2, consistent with field galaxies.

All 5 global properties listed above have been used by various authors in defining galaxies that may be in the process of being quenched, as discussed in Section 1.2. While properties such as bulge-to-total flux ratio or environmental surface density may suggest possible quenching mechanisms, more detailed investigation with tools such as integral field spectroscopy are needed to better define the quenching process.

Only the Above-MS, MS and Below-MS groups are included in analyses of the radial profile of star formation, for reasons discussed in the next chapter. The analyses cannot purport to represent all galaxies, because omitted are Sub-MS galaxies and also galaxies that are below the detection threshold of the SAMI Galaxy Survey. Galaxies which do not have a measurable SFR using the methods of the SAMI Galaxy Survey and this thesis do not appear in these plots, and care is required in calculating proportions of galaxies for any measurement when the number of these 'invisible' galaxies is unknown.

While this important limitation is acknowledged, the study of the distribution of star formation in the Above-MS, MS and Below-MS groups may be helpful in furthering understanding of galaxy evolution and quenching.

Chapter 4

Radial Profiles of Star Formation Surface Density

4.1 Introduction

In this chapter new tools and data provided by the SAMI Galaxy Survey are used to explore how the star formation (SF) distribution within galaxies varies by location on, above or below the main sequence.

Radial profiles of star formation rate (SFR) surface density are used to identify differences in SFRs at different radii of the galaxy. Many quenching mechanisms act locally on a galaxy, for examples: SF at the galaxy centre may be suppressed by bulge growth with higher central stellar mass surface density (Mosleh et al. 2017), by morphological quenching (Martig et al. 2013), and by AGN feedback (Croton et al. 2006, Taylor & Kobayashi 2017). In dense environments, mechanisms such as ram pressure stripping may act preferentially on the galaxy periphery (Gunn & Gott 1972, Schaefer et al. 2017, Schaefer et al. 2019). Other proposed quenching mechanisms may act in a galaxy-wide manner, for example strangulation (Peng et al. 2015).

Each of the above processes may be expected leave a spatial imprint on the distribution of SF on a galaxy. Here, IFU data from SAMI are used to assess observational evidence for such possible local quenching mechanisms within galaxies. The extent to which such local mechanisms influence a galaxy's location on the SFR-mass plane are also considered. The distribution of SF is measured using radial profiles of the SFR surface density. These profiles are characterised using two-part linear fits, and the distribution of slopes is investigated with respect to various other properties.

Galaxies will be identified that have central suppression of star formation and the properties of galaxies with and without central suppression will be examined. Central suppression is based on the presence of a rising profile over 0-0.5 R_e, and (obviously) can only be diagnosed where the radial fit of star formation surface density over 0-0.5 R_e can be obtained. Many galaxies in the Below-MS and MS groups do not have a radial profile over 0-0.5 R_e due to lack of central star forming spaxels, thus their SFR at the galaxy centre is unknown and these galaxies are excluded from further analysis.

4.2 Constructing Radial Profiles

To avoid the impact of non-SF related ionisation or non-detection of emission, non-star forming spaxels (as determined from the emission lines ratios, described in Chapter 2, Section 2.3) have been removed.

In a given annulus the surface density has been calculated using the area of the remaining spaxels in the annulus. Circular annuli are used in calculating profiles in this thesis, with the value of the circularised R_e taken from the GAMA website. Galaxies have been excluded from the sample if their circularised R_e is <2 arc seconds in view of the limit imposed by seeing in SAMI galaxies, generally taken as 2 arc seconds. An R_e of 2 arc seconds means the 0.5 R_e central aperture has a diameter of 4 spaxels, providing 4 measurement points on the central radial profile.

I use the emission line flux maps created in the SAMI pipeline processing as described in Section 2.3 (a) to classify each spaxel using the [O III]/Hβ, [N II]/Hα, [S II]/Hα, and [O I]/Hα flux ratios, (b) to create maps of dust corrected star formation surface density with non-star forming spaxels removed, and (c) to create radial profiles of star formation surface density. Figure 4.1 presents example star formation maps, in the left column 3 examples of star forming galaxies with a falling profile of star formation surface density, moving from the centre outwards. The right column shows 3 galaxies with a rising profile. Non-star forming spaxels are not displayed and included in profile measurements.

In addition to imposing a minimum size requirement, it is also necessary to ensure a sufficient number of spaxels within the radial range of interest to permit a reliable profile to be constructed. This is of particular importance in the central regions, where annuli cover a relatively small area on the sky. Galaxies are therefore required to have a minimum of 60% of the spaxels within $0.5R_e$ to be classified as star forming. Figure 4.2 shows examples of galaxies that do not meet this criterion, which are hereby referred to as centrally non-star forming, or 'Central NSF', galaxies.

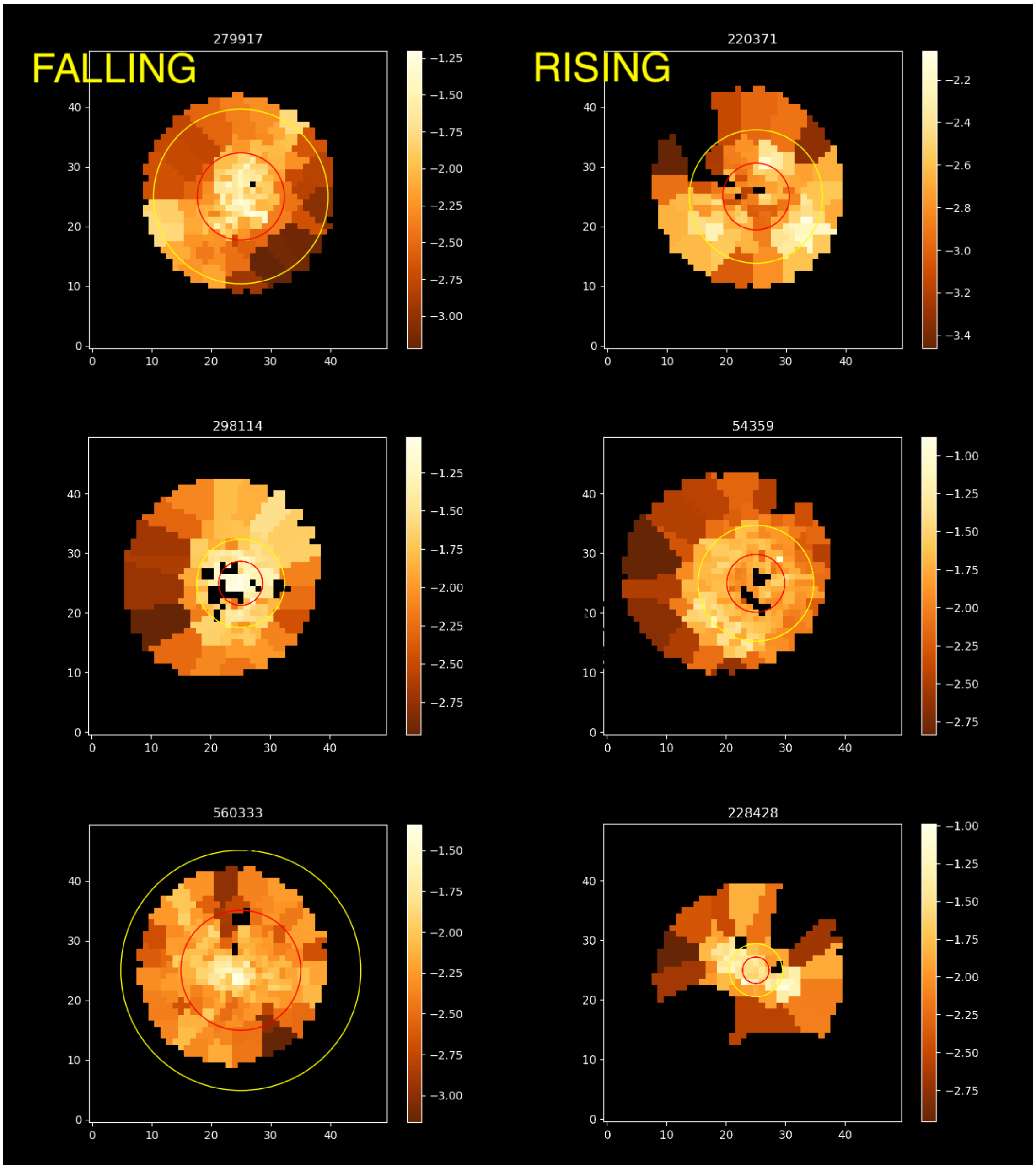

Figure 4.1: *The left column displays 3 examples of galaxies with a falling profile of star formation surface density, moving from the centre outwards. The right column shows 3 galaxies with a rising profile. The annuli shown are 0.5 (red circle) and 1 (yellow)* R_e.

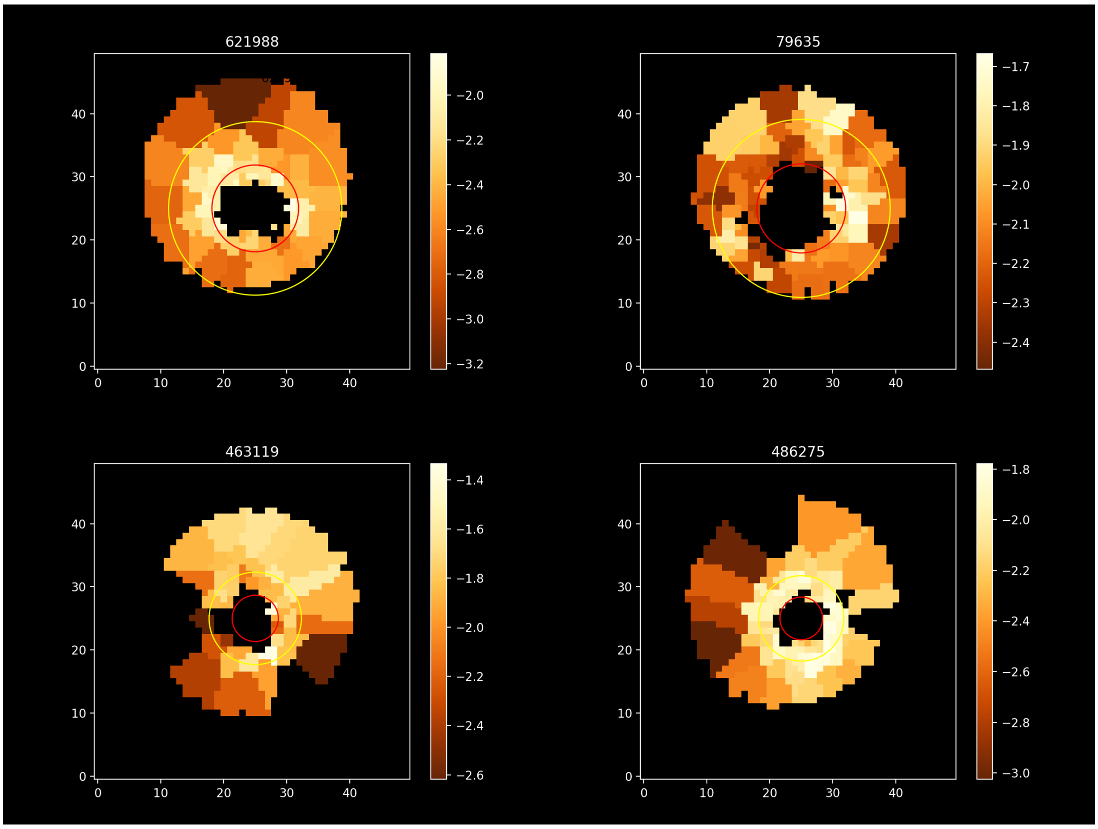

Figure 4.2: *The galaxy star formation maps display star-forming galaxies that have < 60 per cent of spaxels within a 0.5 R_e radius that are star-forming (the annuli shown are 0.5 (red circle) and 1 (yellow) R_e). These galaxies are termed 'Central NSF' galaxies.*

The effect of excluding the Central NSF galaxies on the median radial profiles of star formation is shown in Figure 4.3. The median profiles for galaxies in the Above-MS, MS and Below-MS groups are presented, without any breakdown by galaxy stellar mass. Non star forming spaxels are excluded in all galaxies. The left panel shows all galaxies with a profile (n=633), and the right panel includes only profiles where 60 per cent of the spaxels over 0-0.5 R_e are star forming (n=436). The galaxies with profiles displayed in the right panel constitute the study sample. The only substantial difference between the panels is in the Below-MS group. This indicates that the Central NSF galaxies are most dominant in this group, and are responsible for the central flattening of the median profile in the left panel. Indeed, of the 633 galaxies meeting the size selection, it is found that 7% of Above-MS (5 objects), 25% of MS (105 objects), and 63% of Below-MS (87 objects) are Central NSF. By removing these objects, the median profile of the Below-MS group in the right panel follows a very similar slope to the other sub-groups.

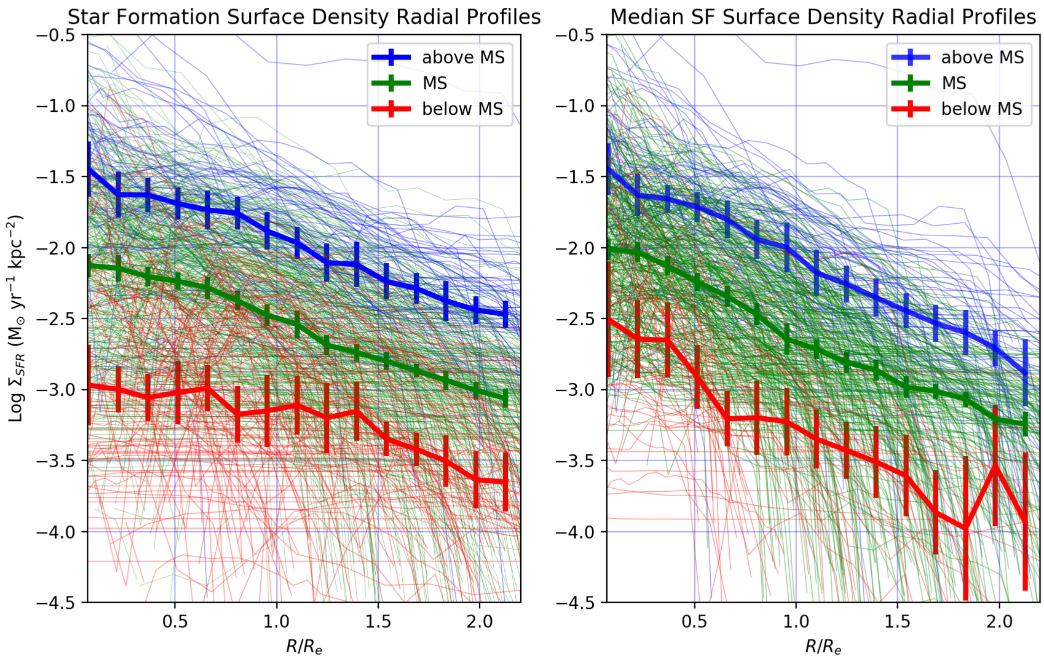

Figure 4.3: *Median radial profiles of star formation of galaxies divided into Above-MS, MS and Below-MS groups. LEFT: the sample of 633 galaxies that includes galaxies not meeting the requirement (that 60 percent of central spaxels are star forming). RIGHT: 436 galaxy profiles remain when galaxies not meeting the requirement are removed, and these galaxies constitute the study sample. The Below-MS group has a profile that declines more rapidly moving from the centre outwards.*

The distribution and proportion of the Central NSF galaxies is displayed in Figure 4.4. There are 196 Central NSF galaxies coded black, that consist of 4 galaxies in the Above-MS zone, 105 in the MS zone and 87 in the Below-MS zone of the plot. Central NSF galaxies have been excluded from the slope analyses in this chapter. Only a minority of the Below-MS galaxies are included in the slope analyses, and it is possible there is a strong bias towards Below-MS galaxies with vigorous central star formation.

To examine why the Below-MS profile changes when the 60 per cent requirement is applied, the dust-corrected Hα luminosity surface density profile has been compared in Below-MS galaxies meeting (below-sf) and not-meeting (below-nsf) the requirement, in Figure 4.5.

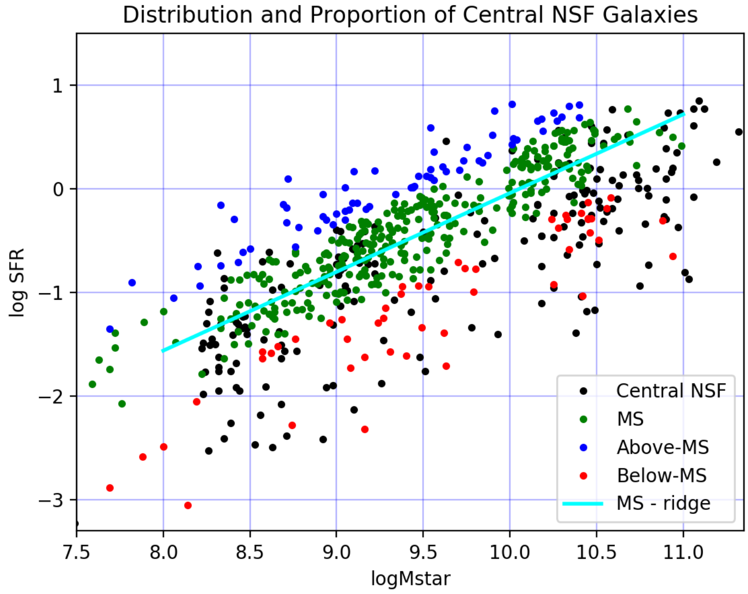

Figure 4.4: *The galaxies are presented in 3 groups (Above-MS, MS and Below-MS) in the scatter plot, with the Central NSF galaxies coded black. Central NSF galaxies are concentrated in the Below-MS galaxies at higher galaxy stellar masses.*

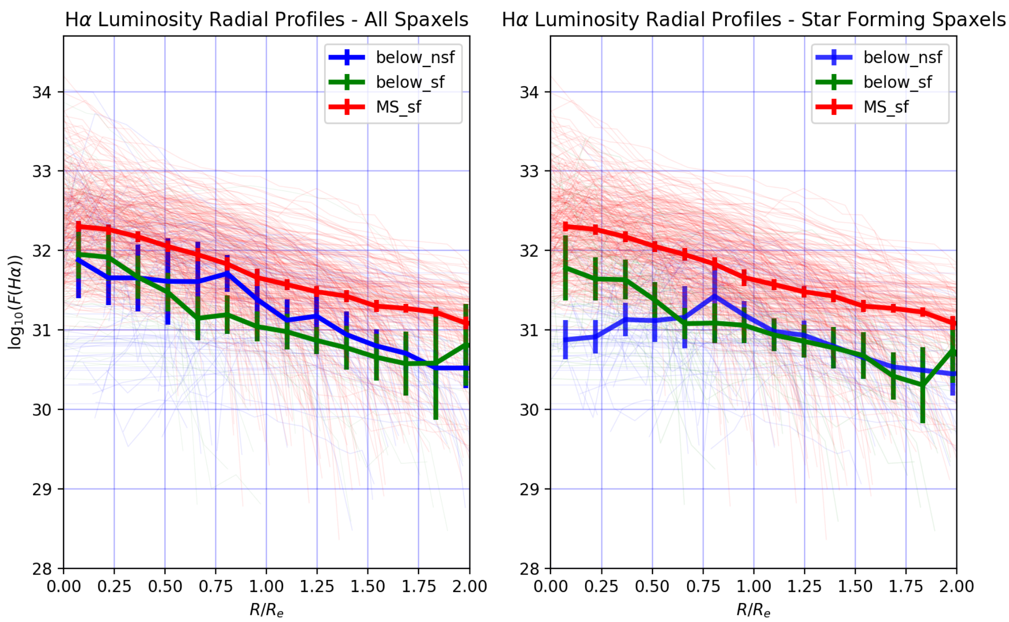

Figure 4.5: *Left: Hα luminosity surface density profiles are compared for Below-MS galaxies meeting and not-meeting the 60 percent star forming spaxels requirement over 0-0.5 R_e, respectively labelled the below-sf and below-nsf groups (below nsf are Central NSF galaxies in the Below-MS group). Profiles of MS galaxies that meet the requirement are also shown. This panel includes measurements of dust-corrected Hα in all spaxels that provide measurements. Right: Only spaxels that are star forming spaxels are allowed to provide measurements. This shows a marked difference between the below-sf and below-nsf groups over 0-0.5 R_e. The below-nsf galaxies have more central suppression than the below-sf galaxies.*

Figure 4.5 (left) plots the Hα flux surface density profiles for the Below MS group, comparing the Central NSF galaxies that do not meet the 60 percent star forming spaxels requirement over 0-0.5 $R_e$with the rest of the sample. The below-nsf galaxies have higher slope (more rising) profile, KS statistic=0.365, p-value = 0.0011. The right panel shows the galaxies with fewer star-forming spaxels at the centre have a lower central Hα surface density than galaxies with more sf spaxels. Not all central Hα emission is the result of star formation, so the central SFR cannot be measured in Central NSF galaxies without considering a more complex decomposition of the possible SF and AGN contributions (Davies et al. 2016). However, even taking the upper limit that all the Hα flux in Central NSF galaxies can be attributed to SF, our results would not change significantly, given the similarity of the raw Hα profiles.

4.3 Radial Profiles of Above-MS, MS and Below-MS groups in 3 mass subgroups

The radial profiles of star formation surface density (shown in the right panel of Figure 4.3 for 436 star-forming galaxies, comprising 68 Above-MS galaxies, 317 MS, and 51 Below-MS) are further investigated in Figure 4.6 with a breakdown of the Above-MS, MS and Below-MS groups into 3 stellar mass bins. Central-nsf galaxies are excluded.

Overall (Overall impressions will be supplemented by detailed slope measurements and analyses in the following sections of this chapter):

- Generally the slopes of the Above-MS, MS and Below-MS groups are similar on large scales.
- There is some evidence that the low mass bin of Below-MS is slightly shallower (slope less negative)
- There is a lot of scatter in the profiles around the generally exponential decline, with some objects showing an intriguing central decline in SF.

.

Between 0 - 2.2 R_e the 3 mass group profiles show a smooth and exponential decline, and run generally in parallel. Within each subgroup the higher mass galaxies have higher SFRs but the slopes of the profiles are similar to the lower mass galaxies. In a given mass range little difference is apparent in the slope of the profiles between the Above-MS, MS and Below-MS groups, with the following exception.

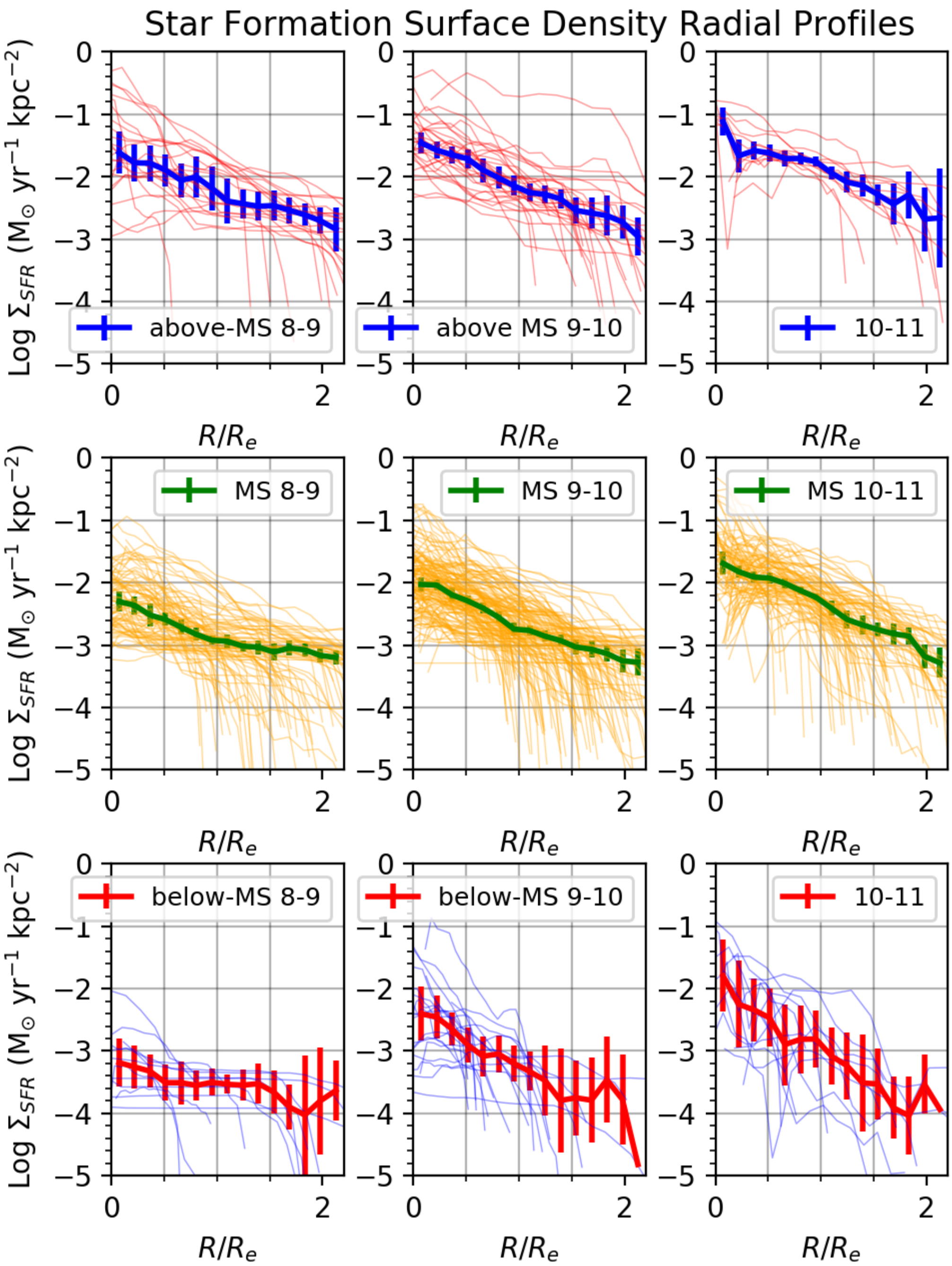

Figure 4.6: *Radial profiles of star formation of galaxies in 3 galaxy log stellar mass groups are compared for the Above-MS, MS and Below-MS groups.*

Comparing the MS and Below-MS groups in Figure 4.6 the MS group shows a near-exponential decline between 0 - 1.5 R_e while for the Below MS subgroup in the

$\log M_* = 8 - 9$ mass bin the decline is less, that is the profile is clearly flatter (slope values **less** negative). By contrast in the $\log M_* = 10 - 11$ mass bin the decline is greater (slope values **more** negative), a finding that may reflect the fact that 63 per cent of Below-MS galaxies are excluded as Central NSF galaxies.

4.4 Measurement of Slope Values of Profiles in Galaxy Groups

From the initial inspection of the SFR profiles, a two-part linear fit is now considered, as a simple way of capturing deviations from a simple exponential decline. The 'inner fit' refers to the profile over $0 - 0.5R_e$, and an 'outer fit' over $0.5 - 1.5R_e$. In particular, a number of profiles indicate a central depression in SF compared to a simple exponential. This change in slope appears to happen around 0.5 R_e, which is also a characteristic radius for potential quenching effects due to a bulge or central AGN; Belfiore et al. (2018) present radial profiles of galaxies with a central depression in star formation and also demonstrate the change in slope at around 0.5 R_e.

Some examples of fits to individual radial profiles of star formation surface density are displayed by comparing radial profiles for the Above-MS, MS and Below-MS groups in small groups of 5 galaxies per plot (Figures 4.7; 4.8; 4.9). In each figure, Above-MS, MS and Below-MS, the upper 2 plots each display 5 galaxies with a rising profile (increasing from the centre moving outwards with slope of fit >0) over 0-0.5 R_e and the lower 2 plots a falling profile (decreasing from the centre moving outwards with slope of fit <0).

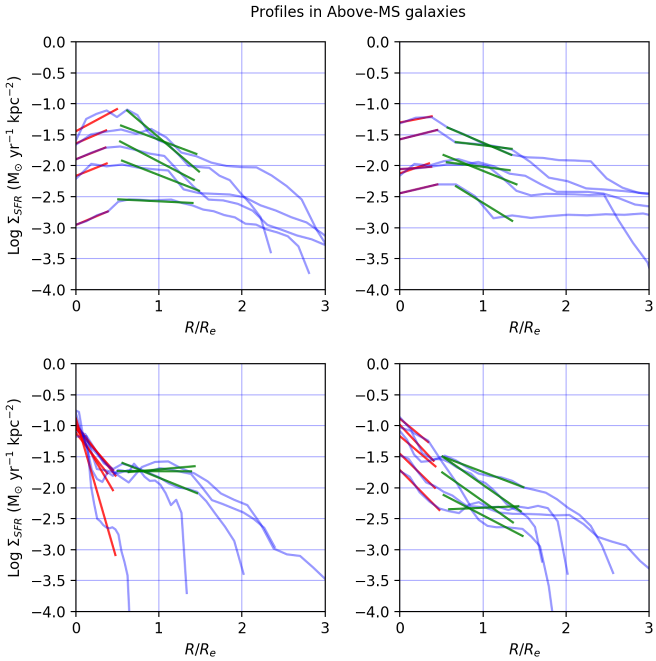

Figure 4.7: *Above-MS Galaxies. The upper 2 plots each display 5 galaxies with a rising profile (increasing from the centre moving outwards with slope of fit >0) over 0-0.5 R_e (red fits) and the lower 2 plots a falling profile (decreasing from the centre moving outwards with slope of fit <0). The green lines are the fits over 0.5-1.5 R_e.*

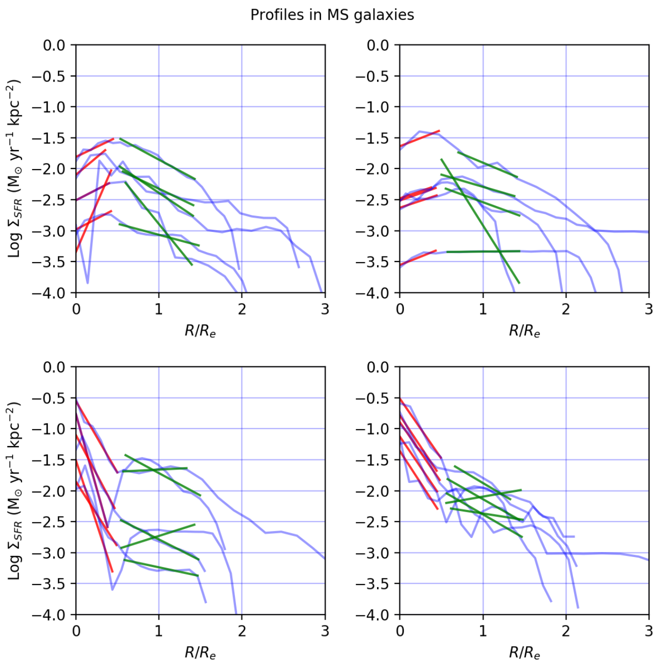

Figure 4.8: *MS-galaxies with rising profiles are displayed in the upper panes and falling profile galaxies in the lower 2 panes.*

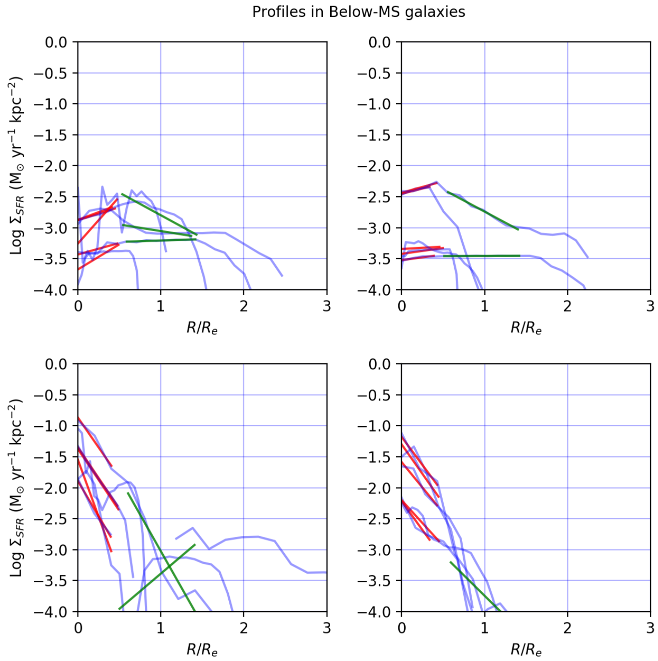

Figure 4.9: *Below-MS Galaxies, with examples of rising profiles in the upper panes and falling profile galaxies in the lower 2 panes.*

The inner slope values of all galaxies that have measurements of the profile slope value over 0-0.5 R_e are presented in Figure 4.10.

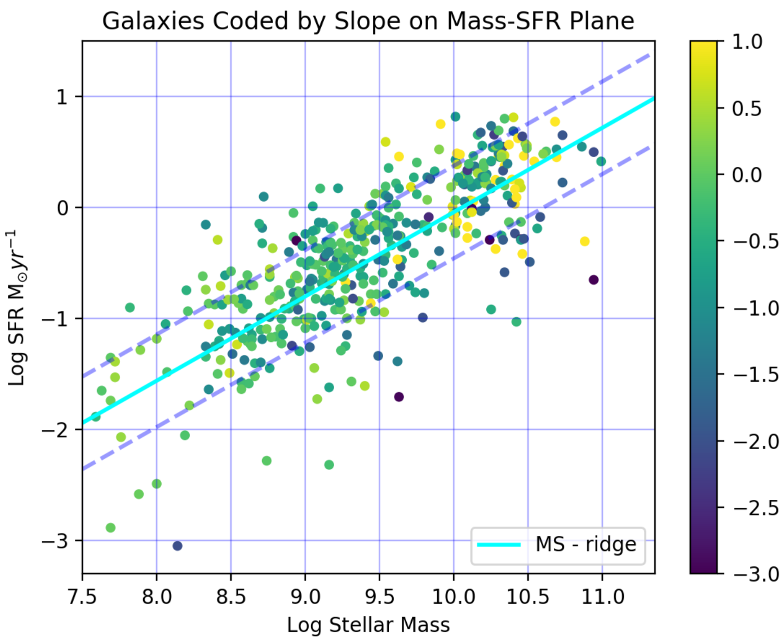

Figure 4.10: *The inner slope values over 0-0.5 R_e are color-coded in galaxies located in relation to the MS ridgeline. A positive value is an indication of a rising profile (increasing from the centre moving outwards)*

The figure shows that positive values of inner slope (a rising profile) occur in galaxies irrespective of their location on, above or below the MS. More detailed analyses of rising slope galaxies follow.

4.4.1 Errors on Slope Measurement

Errors in the profile slope measurement are computed using python numpy polyfit and covariance code. Direct calculation of a reliable error in this way was possible for 55% of the sample, with the remainder having too few points in the 0-0.5 R_e profile. In those cases, the slope error was estimated by taking the mean error within the same SFR subgroup.

The slope errors are used to robustly classify galaxies with a rising central SF profile. For a galaxy to be classified as having a rising profile, the central (0-0.5 R_e) slope must be a positive value greater than the slope error - i.e. inconsistent with zero at the 1 σ level or higher. To verify that the errors (and therefore potentially the classification as rising or not) are not biased, the following plots present the errors plotted against other values, including slope value, mass, and star formation.

Figure 4.11 illustrates the magnitude of the errors, and the relationship of errors to galaxy mass, SFR, the slope value itself, and the 'delta-SFR' which is the distance above or below the MS ridgeline on the mass-SFR plot.

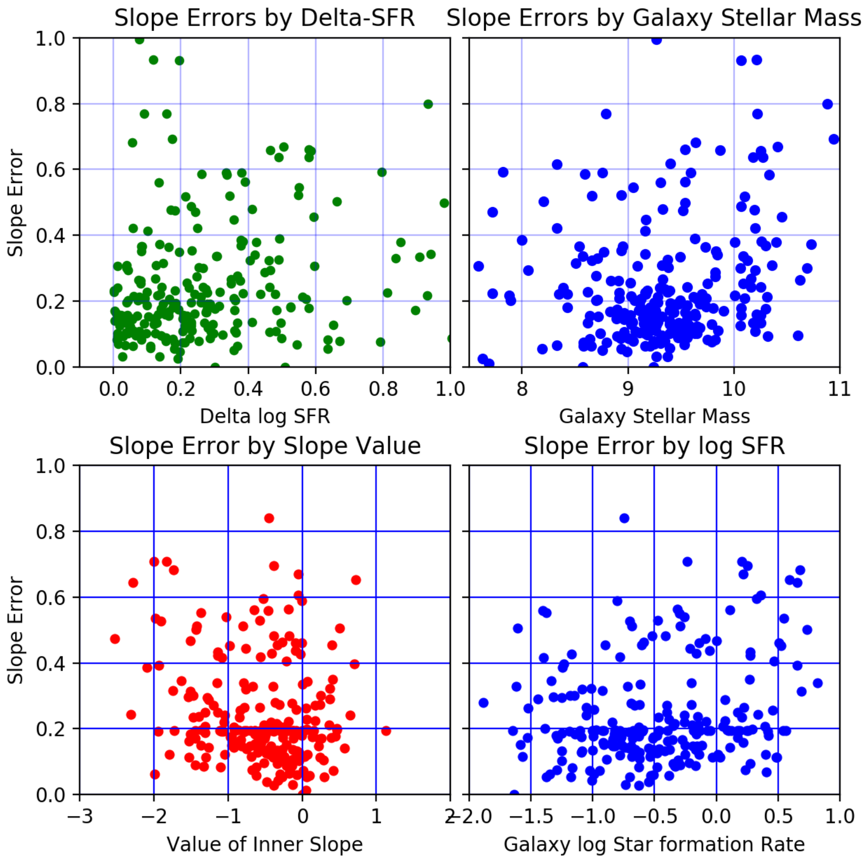

Figure 4.11: *The relationship of slope errors to the 'delta-SFR', the galaxy mass, the slope value itself, and the SFR are presented.*

There is a statistically significant relationship between the radial profile slope errors, and the galaxy mass, the galaxy SFR, the profile slope value itself, and the 'delta-SFR' (Table 4.1).

Table 4.1: Comparison of Slope Errors of Radial Profiles over 0-0.5 R_e and Galaxy Characteristics

Property	Spearman Correlation	p-Value
Galaxy mass	0.2043	p-value = 0.0015
Log SFR	0.2174	p-value=0.0007
Slope Value	-0.1952	p-value=0.0024
Delta Log SFR	0.2085	p-value= 0.0012

The slope errors are greater in galaxies of higher mass, and higher log SFR (Table 4.1). Higher slope values (profiles falling less steeply, or rising) are associated with lower errors. The distance of a galaxy from the galaxy main sequence ridgeline is strongly correlated, with higher distances having greater errors.

4.4.2 Slope Values of Radial Profiles in Galaxy Groups

Comparisons are made of slope values between the 3 galaxy groups, using the 'inner fit' over $0 - 0.5R_e$, and the 'outer fit' over $0.5 - 1.5R_e$. The profiles with inner fit lines are displayed in 4.12, and inner fit slope values in Figure 4.13, comparing the 3 galaxy groups. The inner fit slope values vary between -5 and 2.

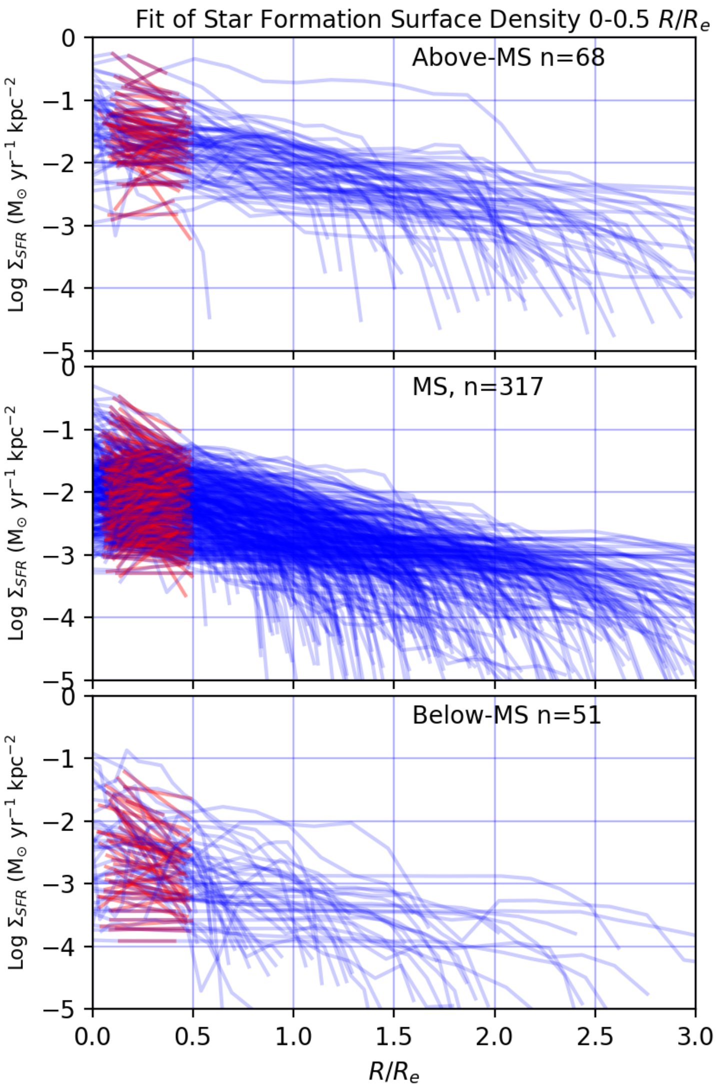

Figure 4.12: *The radial profiles over 0-0.5 R_e are fitted (red lines) and their slope is measured to allow comparison between the Above-MS, MS and Below-MS groups.*

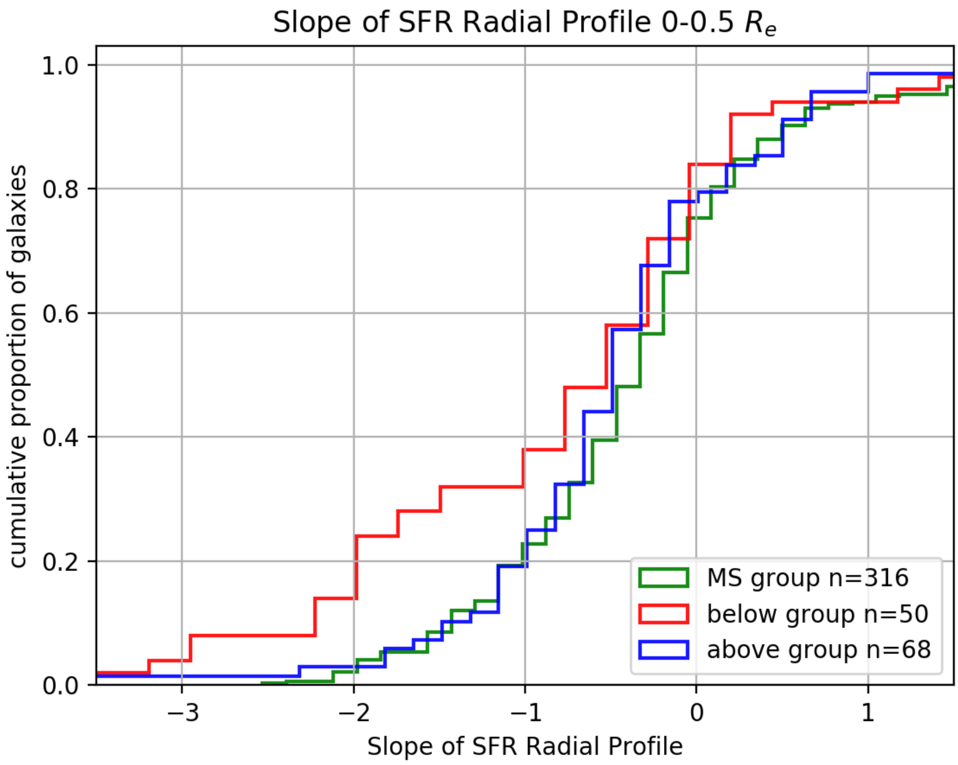

Figure 4.13: *The comparison between the inner fit slope values of the radial profile in 3 groups is made using a cumulative histogram.*

The star formation inner profile slope values over 0 - 0.5 R_e are compared for the Above-MS, MS and Below-MS groups in Figure 4.13 without breakdown into mass subgroups. The Below-MS group (red) shows lower slope values compared to the MS (green) group (KS statistic=0.218, p-value=0.026).

This does not mean the Below-MS group has less central suppression as many Below-MS galaxies did not have a central profile performed (because <60 percent of spaxels were star-forming), and these galaxies are shown (in Figure 4.5) to have similar central Hα luminosity, compared to the Below-MS galaxies with central profiles. The Above-MS group does not differ significantly in the distribution of slope values compared to the MS group, KS statistic = 0.114, p-value = 0.438. This result is consistent with the appearance of the radial profiles in Figure 4.3, right panel.

The effect of mass on the slope of the star formation radial profile is now examined in galaxies on, above and below the MS, in the 3 log stellar mass bins in Figures 4.14 and 4.15, and Table 4.2).

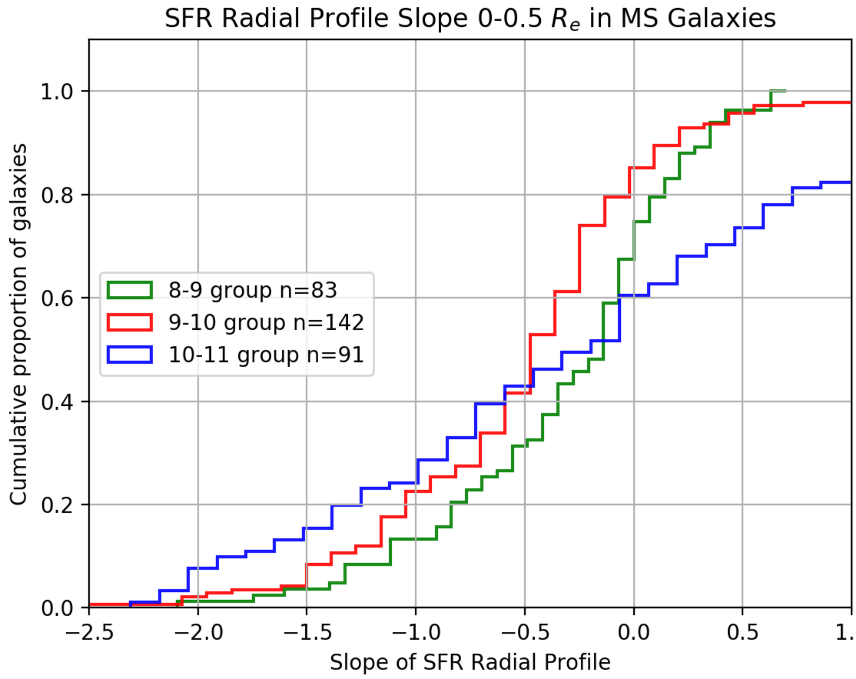

Figure 4.14: *Radial Profiles of star formation of galaxies in 3 galaxy log stellar mass bins are compared for the MS group galaxies. Central NSF galaxies are excluded.*

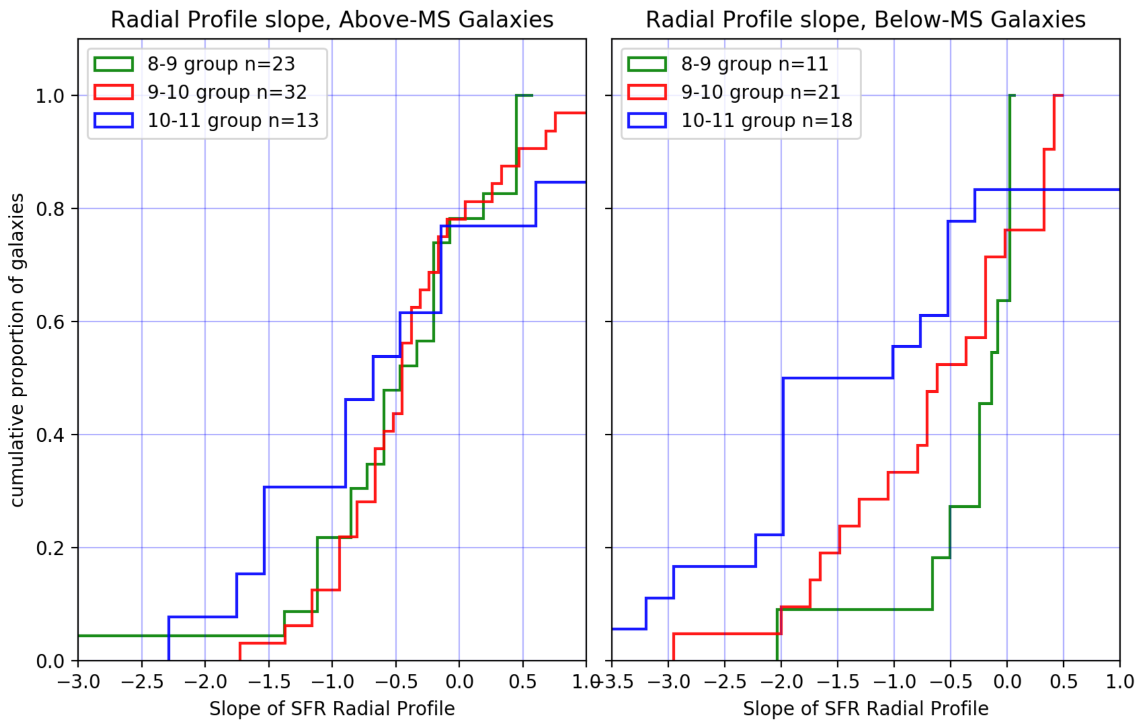

Figure 4.15: *Radial Profiles of star formation of galaxies over 0-0.5 R_e in 3 galaxy log stellar mass groups are compared for the Above-MS (left),and Below-MS (right) groups. Central NSF galaxies are excluded.*

Table 4.2: Comparison of Radial Profiles over 0 - 0.5 R_e of Galaxy Sample

Log Stellar Mass Bin	8-9 v 9-10		9-10 v 10-11		8-9 v 10-11	
	KS statistic	p-value	KS statistic	p-value	KS statistic	p-value
Above-MS	0.1413	0.9343	0.2764	0.4156	0.2642	0.5389
MS	0.2716	0.0007	0.2790	0.0003	0.2606	0.0043
Below-MS	0.3420	0.2990	0.4048	0.0604	0.5051	0.0393

Comparisons are performed of the slope of the radial profile in 3 log stellar mass bins, 8-9 versus 9-10, 9-10 versus 10-11, and 8-9 versus 10-11. Differences are evaluated with the KS statistic, for galaxies above, on and below the MS.

In MS galaxies the 9-10 mass bin differs significantly from the 8-9 bin (Table 4.2), and Figure 4.14 shows the 9-10 bin is steeper (lower slope values, falling more steeply from the centre moving outwards) than the 8-9 bin.

A consistent result has not emerged for comparing the MS 10-11 stellar mass bin to the MS 8-9 and 9-10 bins, despite significant differences in Table 4.2. Figure 4.14 shows this is because in galaxies falling more steeply from the centre moving outwards (slopes < -0.5), the 10-11 mass group galaxies have steeper profiles than the other groups, but in the galaxies with less steep profiles (slopes > -0.5), the 10-11 mass bin galaxies have less steep profiles than the other bins.

In Above-MS galaxies there are no significant differences between the mass bins. In Below-MS galaxies the only significant difference is between the 8-9 bin and the 10-11 bin, at the p=0.04 level, with the slope falling more steeply in the 10-11 bin.

The effect of mass on the radial profile of star formation will be further examined in Subsection 4.5.

4.4.3 Slope of Profiles over 0.5 - 1.5 R_e

The star formation radial profile slope values are now compared for galaxies on, above and below the main sequence, in Figures 4.16 and 4.17.

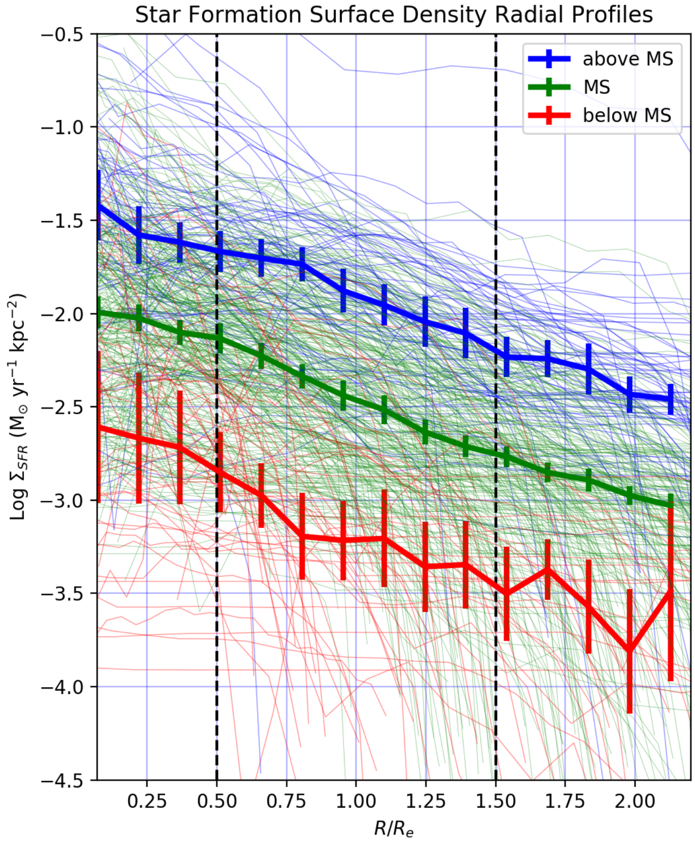

Figure 4.16: *These profiles with the range 0.5-1.5 R_e highlighted are reproduced from Figure 4.3, right pane. The red Below-MS slope appears a little more negative, but overall there is little difference in the profile slope in galaxies above, on and below the MS.*

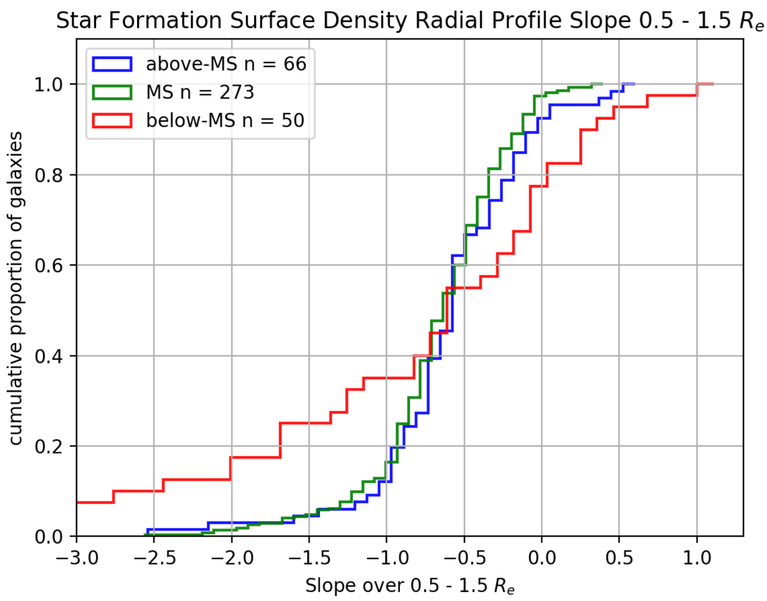

Figure 4.17: *The radial slope values of the Above-MS and MS groups are very similar, however the Below-MS group has a higher proportion of low slope values.*

A comparison of the values of the profile slope over 0.5 - 1.5 R_e for the Above-MS, MS and Below-MS groups is made.

There is no significant difference between the Above-MS and MS group (Above-MS v. MS, KS statistic = 0.108, p-value = 0.538). However the below MS group differs from the MS group having more galaxies with lower values (MS v. Below-MS, KS Statistic = 0.259, p-value = 0.0148). Finally in the Above-MS v. Below-MS comparison, the below-MS group has a higher proportion of low slope values, with borderline significance (KS Statistic = 0.264, p-value=0.050).

4.4.4 Galaxies with Central Suppression

Values of the slope over 0 - 0.5 R_e are called 'rising' if the fit to the profile has a slope value, minus the slope error that is greater than zero. In Figure 4.18 rising profile galaxies are not confined to the Below-MS group and may represent a similar proportion in the Above-MS, MS and Below-MS groups.

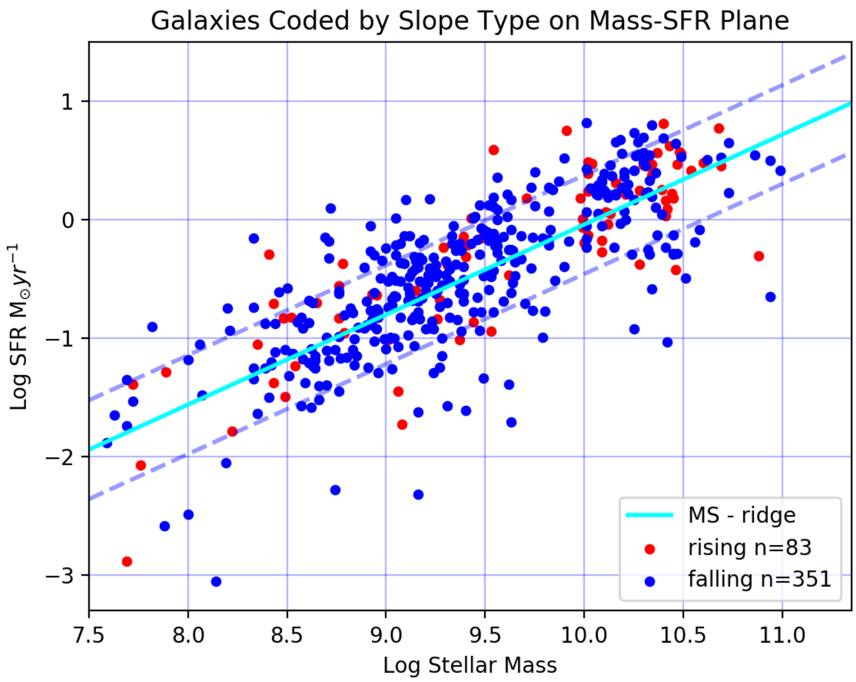

Figure 4.18: *The galaxies with a rising profile slope over 0 - 0.5 R_e are considered to have central suppression and are coded red.*

The galaxies with a rising profile are distributed rather evenly above/below/on the MS, however they appear to have higher galaxy stellar mass values than falling profile galaxies in Figure 4.18 and this is confirmed in Table 4.4 below.

Table 4.3: Slope of Radial Profiles over 0-0.5 R_e of Galaxy Sample

	Above-MS	MS	Below-MS	Total
Rising	11	64	8	83
Falling	57	252	42	351
Total	68	316	50	434
Percent rising	16.2	20.3	16.0	19.1

The frequency of rising and falling profiles are compared in the 3 groups. A substantial number of rising profiles (a marker of central suppression) are seen in all groups.

4.5 Properties of Galaxies with Rising or Falling Central Slope Values

This section addresses whether properties of galaxies with central suppression (rising central profile) differ from those with a falling central profile, or from Central NSF galaxies.

The sub-groups to be compared are rising, falling and Central NSF. Properties to be compared are galaxy stellar mass, g-i color, Sérsic index, bulge-total flux ratio, and environmental density. The statistics on the plots are shown in Table 4.4.

Galaxy Stellar Mass

Figure 4.19 shows the log stellar mass is significantly higher (p=1.283e-5) in galaxies with a rising profile, compared to the falling profile group (Table 4.4). This was also apparent in Figure 4.18.

A correlation of galaxy stellar mass and central slope is sought in Above-MS and MS galaxy groups. (Below-MS galaxies were not included because most Below-MS galaxies are unable to have a central slope value determined.) No correlation is present, Spearman correlation = -0.0042, p-value=0.9352)

The Central NSF galaxes have higher mass compared to the falling galaxies (p=9.923e-10), and to the rising galaxies (p=0.022).The higher mass of Central NSF galaxies was also apparent in Figure 4.4.

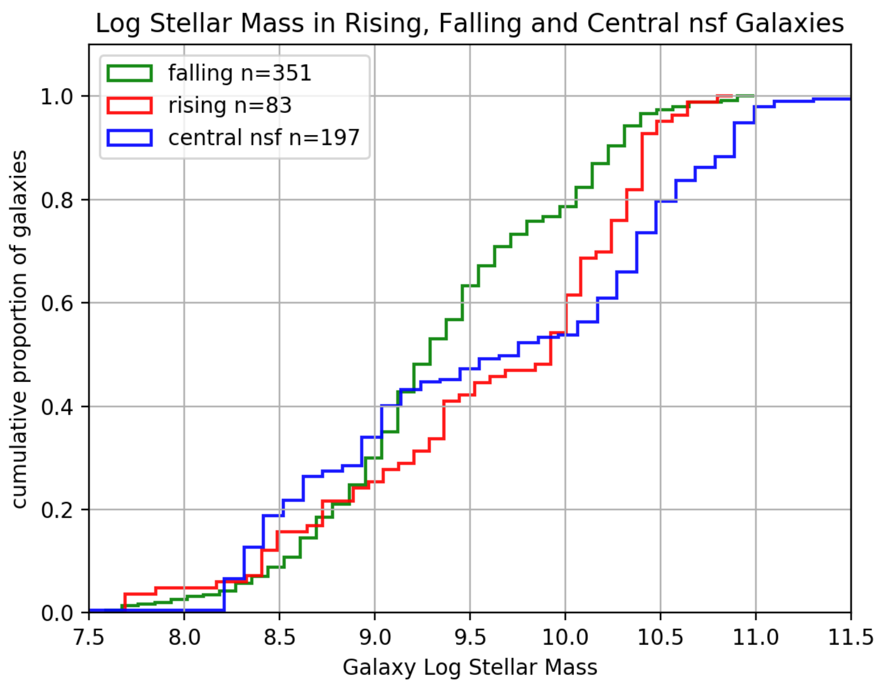

Figure 4.19: *The log stellar mass is compared in galaxies with profiles over 0-0.5 R_e that are rising, falling and Central NSF, for all galaxies (includes Above-MS, MS and Below-MS groups).*

$g - i$ Color

The $g-i$ color is significantly higher (redder) for rising profile than falling profile galaxies (p= 0.0078).

A correlation of $g - i$ color and central slope is sought in Above-MS and MS galaxy groups. (Below-MS galaxies were not included because most Below-MS galaxies are unable to have a central slope value determined.) No correlation is present, Spearman correlation = 0.0151, p-value = 0.7676).

Central NSF galaxies have a higher $g-i$ color value compared to falling profile galaxies (p=8.155e-16), and to rising profile galaxies (p=1.378e-5).

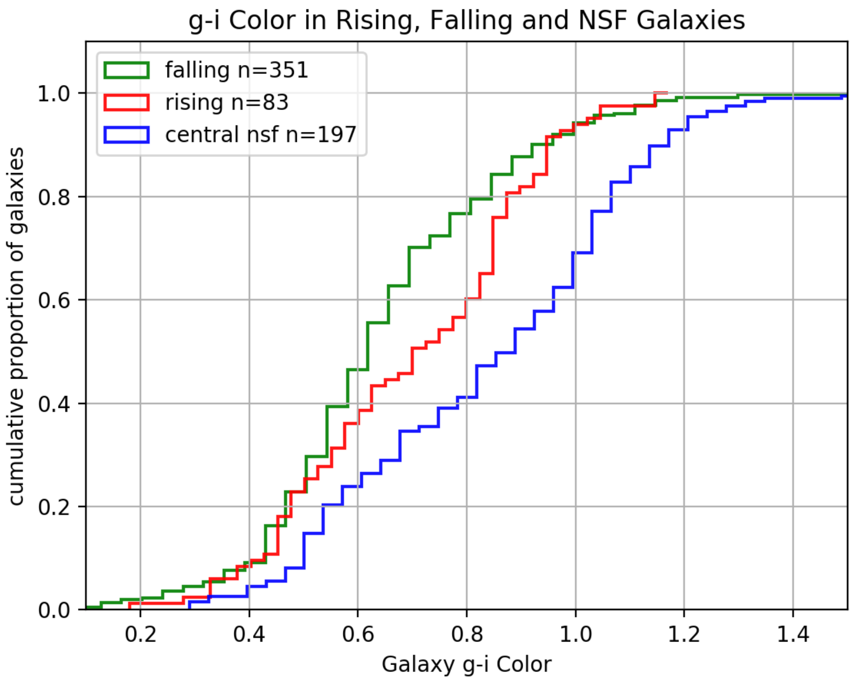

Figure 4.20: *The $g - i$ color is compared in galaxies with rising, falling and Central NSF galaxies.*

Sérsic Index

No difference has been detected in values between rising profile galaxies and falling profile galaxies (p=0.387).

Both the rising and falling groups have 60 per cent of galaxies with a Sérsic Index < 1.5, compared to 50 per cent of Central NSF galaxies.

Central NSF galaxies have higher Sérsic Index values compared to rising (p=0.015) and to falling profile galaxies (p=5.040e-6).

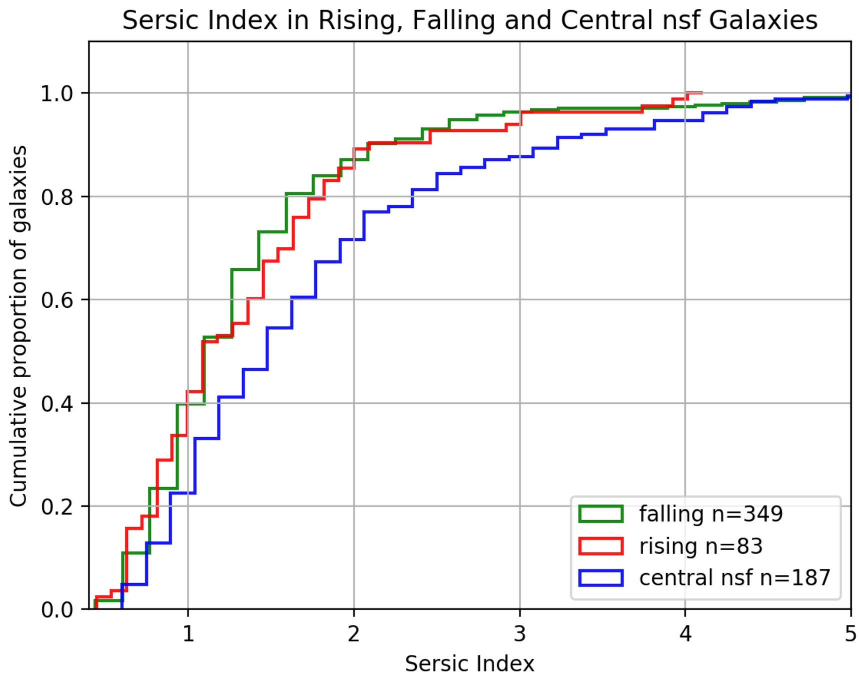

Figure 4.21: *The Sérsic Index is compared in galaxies with rising and falling radial profiles, and Central NSF galaxies.*

Bulge/Total Flux Ratio

The Bulge/Total Flux Ratio is compared in galaxies with central suppression (rising central profile), those with a falling central profile, and Central NSF galaxies. In Figure 4.22 there is no significant difference in bulge/total flux ratio between the rising and falling profile galaxy groups (p= 0.0834).

The Central NSF group has higher values compared to both the rising (p=0.0087) and the falling groups (p=0.043).

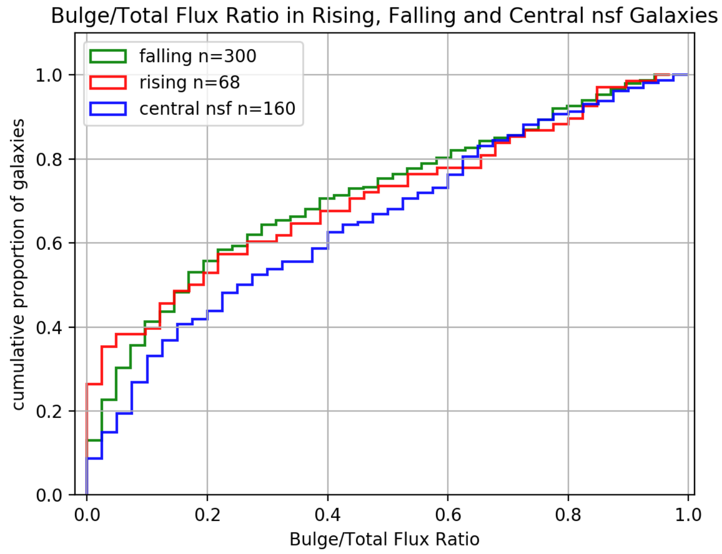

Figure 4.22: *The distributions of bulge/total flux ratio values are compared in galaxies in the rising, falling and Central NSF groups in a cumulative histogram.*

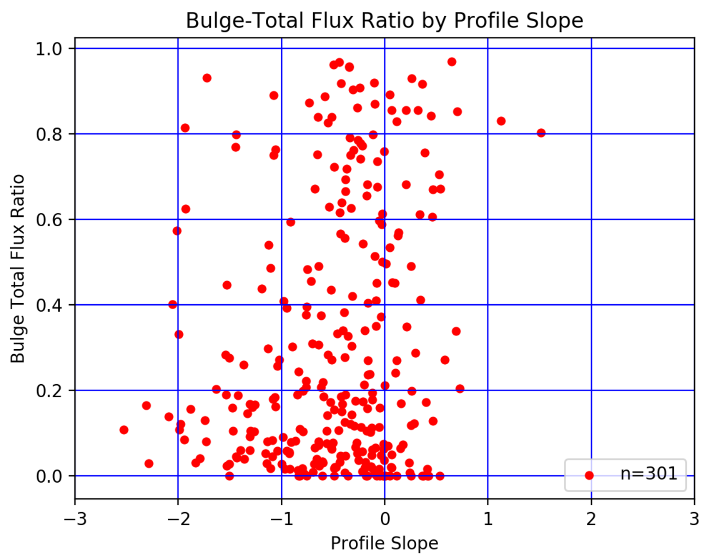

Figure 4.23: *The bulge-total flux ratio values are compared to profile slope values over 0-0.5 R_e in 482 galaxies in the Above-MS, MS and Below-MS groups.*

The bulge-total flux ratio values are compared to profile slope values over 0-0.5 R_e in 482 galaxies (in the Above-MS, MS and Below-MS groups) in Figure 4.23.

A positive correlation has been found at the p=0.04 significance level.

Spearman Correlation=0.1194, p-value=0.0385.

Environmental Surface Density

The environmental surface density is based on the distance to the Nth nearest neighbour among the density defining population in a velocity cylinder of:

1000 km/s, i.e. N / Pi * DistanceToNnn^2, as discussed in Section 2.6.3.

Three groups are compared: galaxies with central suppression (rising central profile), those with a falling central profile, and Central NSF galaxies.

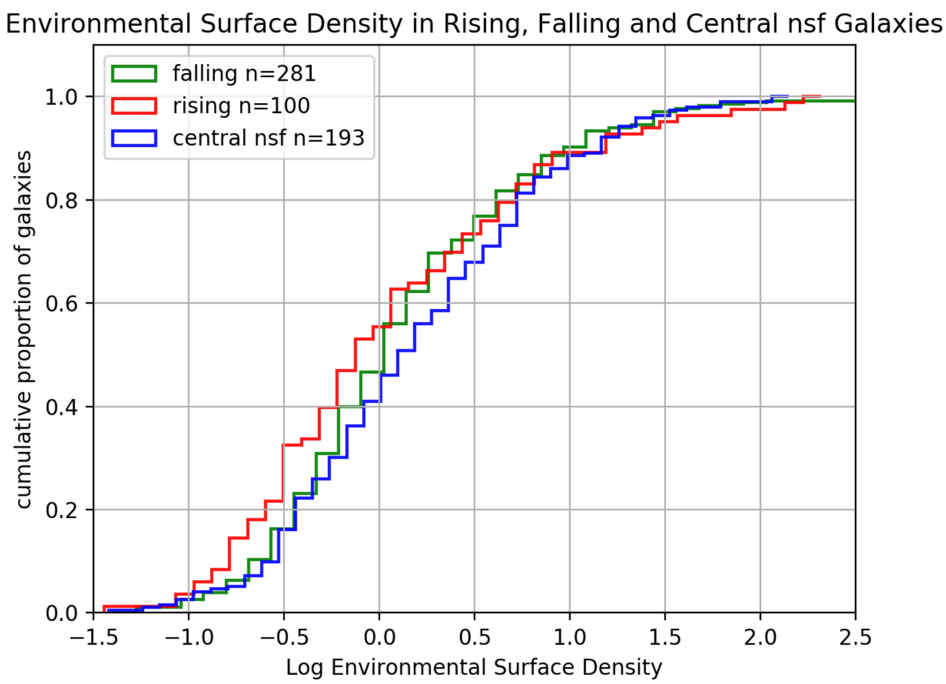

Figure 4.24: *The environmental surface density is compared in galaxies with rising, falling and Central NSF profiles over 0-0.5 R_e.*

There are no significant differences in environmental surface density between the 3 groups.

Comparing falling v. rising, p= 0.098; rising v. Central NSF, p =0.090; and falling v. Central NSF, p = 0.1115.

Table 4.4: Analysis of Properties of Galaxies with Rising and Falling Radial Profiles over 0-0.5 R_e

Property	fall v. rise		rise v. Central NSF		fall v. Central NSF	
	KS statistic	p-value	KS statistic	p-value	KS statistic	p-value
Mass	0.2937	1.283e-5	0.1936	0.022	0.2880	9.923e-10
g-i color	0.2001	0.0078	0.3135	1.3775e-05	0.3704	8.1548e-16
Sérsic Index	0.1086	0.3871	0.2026	0.0151	0.2274	5.0400e-6
Bulge/Total Flux Ratio	0.1663	0.0834	0.2342	0.0087	0.1338	0.0434
Environ. Surface Density	0.1475	0.0979	0.1606	0.0898	0.1065	0.1115

Galaxy log stellar mass, g-i color, Sérsic Index, bulge/total flux ratio, and environmental surface density are compared in galaxies with rising and falling radial profiles, and Central NSF galaxies. The two-sample Kolmogorov–Smirnov test is used to compare the probability distribution of the samples.

4.6 Summary and Discussion

The galaxy sample consists predominantly of star forming galaxies in a low density environment, as noted in Methods Section 2.2. Of 633 galaxies in the Above-MS, MS and Below-MS groups, 197 do not meet the requirement that 60 percent of spaxels over 0-0.5 R_e are star forming; these galaxies are termed 'Central NSF' and radial profiles of star formation surface density cannot be obtained.

Radial profiles of star formation are produced for 436 star-forming galaxies, comprising 68 Above-MS galaxies, 317 MS, and 51 Below-MS. Overall, the profiles of SF fall exponentially, and have very similar gradients regardless of where a galaxy is located on the SFR-M plane. Thus galaxies falling below the main sequence of star formation have reduced star formation across the disk, and galaxies above the main sequence have higher values across the disk. This implies that the main reason for galaxies being below the SFR-MS is because their SFR is globally reduced. Whatever the quenching process is that drives this reduced SFR, it acts in such a way that SF remains largely coherent across the galaxy body.

The SFR profile shapes are quantitatively explored using a 2-part linear fit, deriving an 'inner' slope (0-0.5 Re), and an 'outer' slope (0.5-1.5 Re). Outer slopes are remarkably consistent across the sample, that is there is little variation in slope for above-MS, MS and Below-MS galaxies.

There is some evidence for a population of objects with inner slopes that differ from their large-scale slopes. Galaxies with a rising inner radial profile of star formation surface density have been identified in the Above-MS (16.2 per cent of galaxies), MS (20.3 per cent) and Below-MS (16.0 per cent) groups, indicative of a central suppression of SF with respect to the outer regions. Galaxies can be separated into rising and falling inner slopes. Most galaxies in the Above-MS and MS groups have a falling profile over 0-0.5 R_e.

Galaxies with a rising inner slope are found at all locations in the SFR-M plane, while Central NSF galaxies are concentrated below the ridgeline.

Comparing inner rising, inner falling and Central NSF galaxies, it is found that:

- Inner rising galaxies are found at higher masses than inner falling, and are close to the mass distribution of Central NSF.
- There is mild evidence for inner rising galaxies having distinctly redder colours than their falling counterparts, but not as red as Central NSF galaxies
- In terms of Sérsic index, B/T and environment, inner rising and inner falling galaxies are not significantly different
- The Central-NSF galaxies, however, show mild differences in the distribution of these three parameters, having steeper Sérsic indices, higher B/T ratios, and being preferentially in higher density environments
- Overall, there is no clear connection between the inner profile slope and other global parameters. In terms of mass and colour, inner rising profiles appear connected to Central NSF galaxies. In terms of morphology and environment, they are indistinguishable from 'normal' inner falling profile galaxies. They may form some intermediary between these two extremes.

Chapter 5

DISCUSSION AND CONCLUSIONS

This chapter presents a reflection on the main findings presented in this thesis, and compares these with relevant works in the literature, both observational and theoretical. The discussion focuses on the two main empirical findings, namely the large-scale similarity in the relative distribution of star formation within the sample; and the existence of a subset of galaxies that show a relative suppression of star formation in their central regions, creating a positive ('rising') star formation profile slope. These behaviours are considered in terms of contemporary ideas around the quenching of galaxies. Finally, a summary is provided, together with an indication of future work.

The rising profile is taken as an indicator of central suppression of star formation and is evidence of a central quenching process, however the evidence linking central suppression to overall galaxy quenching is weak. Another main finding, that star formation is generally coherent (as defined in Section 1.2.4) favors a mechanism such as strangulation or cosmic web detachment as a quenching mechanism. This study has been unable to distinguish between quenching from the inside out such as the 'compaction' scenario, and strangulation as a primary quenching mechanism, as only a small non-representative fraction of the Below-MS galaxies are able to have a radial profile measured.

5.1 Does star formation vary coherently within galaxies across the SFR-Mass plane?

In the study sample, star formation is enhanced (or depressed) at all galactic radii by a similar proportion at, above or below the main sequence (MS). Thus the profile gradients are remarkably similar whether a galaxy is above, on, or below the MS. Significant differences in profile have not been demonstrated between Above-MS, MS and Below-MS galaxies, nor have differences in profile by galaxy stellar mass group been demonstrated. In section 4.3, Figure 4.6 presented the observed radial profiles of SFR density for the 436 sample galaxies, divided across mass and location with respect to the SFR MS. The overall slopes show a remarkable degree of similarity. This was further quantified in subsection 4.4.3, where a linear fit was used to quantify the profile slope between 0.5-1.5 R_e (hereafter 'outer' slopes). This showed that the profiles follow a tight distribution of slope values, and which do not depend strongly on mass or distance from the SFR MS.

Nelson et al. (2016) argue that if the primary physical processes driving star formation in galaxies above the MS are AGNs or central starbursts, then Hα would be enhanced in the center but not at larger radii. Conversely, if there was a quenching process such as 'inside-out' quenching (for examples Genzel et al. 2014, and Tacchella et al. 2015), then galaxies below the MS may have Hα primarily reduced in the centre. But this is not what the radial profiles indicate. In most galaxies in the current SAMI study, as well as Nelson et al. (2016), the star formation is spatially coherent. A caveat is that the radial profiles for the central NSF galaxies, and the galaxies in the Sub-MS subgroup have not had radial profile slope measurements in this study.

Coherent star formation points to the presence of a galaxy-wide throttle or controller of star formation, that operates in addition to well-established quenching mechanisms that act locally, e.g. the bulge at the centre, or ram pressure stripping at the galaxy periphery. There is recent theoretical and observational support for such a galaxy-wide controller of star formation. Peng et al. (2015) report an analysis of the stellar metallicity in local galaxies based on 26,000 spectra, that reveals strangulation is the primary mechanism responsible for quenching star formation, and rules out alternative mechanisms such as gas removal through outflows or stripping (as discussed in Subsection 1.2.4). These authors study the chemical evolutionary paths of model galaxies with and without the inflow of gas to demonstrate strangulation is needed to explain the higher metallicities of quiescent galaxies.

Strangulation and quenching of galaxies may be explained using a model of cosmic web detachment (Aragon-Calvo et al. 2019). The model has star-forming galaxies connected to a web of primordial filaments from which they accrete gas. The removal of the feeding filaments connected to the galaxy (cosmic web detachment), that occurs when galaxies merge or collide with other gas filaments or walls leads to strangulation and quenching.

Kraljic et al. (2018) note that in cosmic web detachment the turbulent regions inside filaments prevent galaxies from maintaining the connection to their filamentary flows and thereby prevent replenishment of their gas reservoir.

5.2 Rising radial profile of star formation surface density over 0-0.5R_e

In addition to the large-scale coherent picture discussed in the previous subsection, some of the sample SF profiles indicate a significant change of slope in their central regions, on a scale that may be relevant for tracing bulge-, bar-, or nucleus-related phenomena. This is explored via linear fits to the central SFR density profile over the 0-0.5 R_e radial range (see section 4.4.4), finding that 16-20% of galaxies show evidence of a positive central gradient (or 'rising' profile). Galaxies with a rising profile may be assumed to have central suppression of star formation, although a vigorous starburst at a distance from the nucleus could also create this profile (Tacchella et al. 2018). Thus it is possible in the low mass galaxies with a rising profile, the profile is due to starburst at a distance from the nucleus, and not due to central suppression. The Below-MS (16.0 percent) value is a lower limit as 63 percent of Below-MS galaxies are central NSF galaxies, for which a measure of the SF radial profile slope is not obtained (see below); however the Hα radial profile suggests that many have central suppression.

The frequency of central suppression in the galaxy sample is unexpected as Nelson et al. (2016) find the absolute SFR (based on the measurement of Hα) is always centrally peaked, in a sample of star forming galaxies across the entire SFR–M* plane at z$\sim$1, and is not centrally depressed or even flat. This applies to galaxies above, on and below the MS. These authors state the radial surface brightness profile shape for Hα in log(flux)-linear(radius) space appear to be nearly linear, indicating that they are mostly exponential or near exponential, and they conclude there is substantial ongoing star formation in the centers of galaxies at all masses.

A possible explanation for the apparent lack of centrally suppressed / centrally rising profiles in the Nelson et al. (2016) study is that, unlike the current study, those authors create mean Hα maps by stacking the Hα maps of individual galaxies with similar M* and/or SFR in order to measure the average spatial distribution. Orr et al. (2017) in a simulation from the FIRE (Feedback in REalistic Environments) project investigate how stacking may obscure variation in individual radial profiles of star formation 5.1. This simulation may explain how the stacking may have led Nelson et al. (2016) to conclude the SFR is always centrally peaked, and is not centrally depressed, and thereby overlook a proportion of galaxies with a rising radial profile (central suppression) over the central area. In this thesis the median profiles show consistent exponential decline with radius, but the analysis finds that 15-20 percent of the galaxies have central suppression.

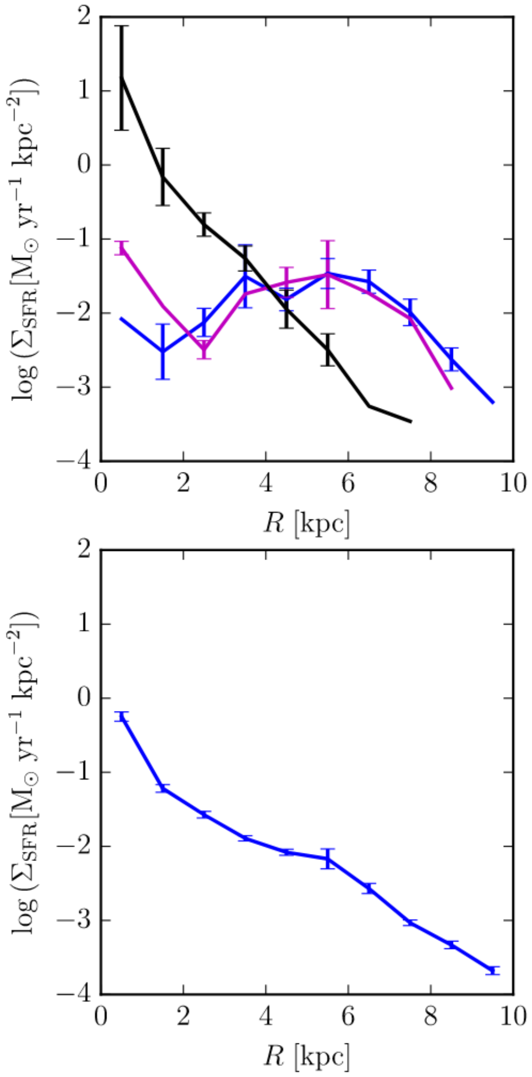

Figure 5.1: *The stacking effect on radial profiles: extract from Fig. 1, Orr et al (2017). The effect of stacking images on the SFR surface density radial profile is examined in simulations from the Feedback in Realistic Environments (FIRE) project. The above panel displays unstacked profiles, and the bottom panel, stacked. These authors conclude the SFR profiles of individual galaxies are much more complex than the stacked profiles.*

Another study has reported a rising radial profile over the inner galaxy in a proportion of MS galaxies around the redshift of peak SFR in the Universe: Tacchella et al. (2018) studied radial profiles of star formation surface density in 10 star forming galaxies (described as typical star forming galaxies on the MS at redshift 2.0 - 2.4). Their Fig. 8 (extracted in Figure 5.2) includes 2 galaxies with a rising central profile.

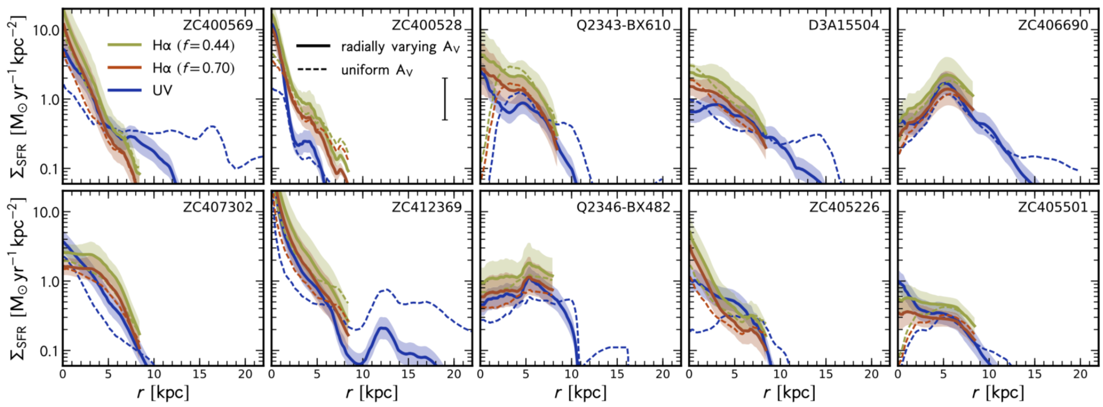

Figure 5.2: *Extract from Fig.8, Tacchella et al. (2018). In the top row galaxy 5 (ZC406690), and bottom row galaxy 3 (Q2346-BX482) display a rising SF radial profile (the red line) over the inner galaxy.*

The finding of central suppression of star formation in Above-MS and MS galaxies is consistent with proposed quenching mechanisms such as bar quenching and compaction associated with nuclear starbursts, that may lead to central suppression while star formation continues elsewhere in the disk (Tacchella et al. 2016; Ellison et al. 2017; see also Sections 1.1.7 and 1.2.1).

The finding of a (roughly) consistent fraction of galaxies with a rising inner profile is consistent with cyclic central star formation. Several authors propose that cyclic central star formation associated with intermittent central suppression of star formation is common in starforming galaxies (Krumholz et al. 2017; Tacchella et al. 2018; Sormani et al. 2019). Based on a dynamical model of the Milky Way central molecular zone Krumholz et al. (2017) argue cycles of bursty (intermittent) star formation and winds are ubiquitous in the nuclei of barred spiral galaxies, with bursts occurring at $\sim 20 - 40$ Myr intervals, and periods of quiescence in between. A quick calculation (based on the redshift range of the thesis sample of 10.63 Gyr to 11.34 Gyr, and an assumption that the burst and quiescence phases have equal duration) suggests the rising profile phase occurring 20 percent of the time means that phase cannot last much longer than 140 Myr, otherwise rising phases would occur more often. The cycle may cease above a threshold halo mass when fresh gas supply is suppressed by a hot halo allowing the long-term maintenance of quenching (Zolotov et al. 2015); this applies only for halos above logM ~11.6, corresponding to a stellar mass of around logM~10 (assuming the halo mass- galaxy mass relation of Behroozi & Silk (2018)).

Is there evidence a rising profile may be a signature of a quenching process? The values of 2 known quenching indicators (galaxy stellar mass and $g - i$ color) are both significantly higher in galaxies with a rising profile compared to the falling profile group. This is consistent with the finding of Lin et al. (2019) that high-stellar-mass galaxies have a higher rate of inside-out quenching compared to low-stellar-mass ones, irrespective of the galaxy environment. However neither galaxy stellar mass nor $g - i$ color are significantly correlated with profile slope in the Above-MS and MS galaxies (Section 4.4.4). The inability to measure the central radial profile in a majority of galaxies in the Below-MS and Sub-MS groups has prevented a clear answer to this question. It is possible that the correlation of mass, and $g - i$ with rising profile in the Below-MS group may be driven by selection bias, rather than something intrinsic, and a more complete treatment of the region further below the MS would be needed (requiring higher resolution data in the galaxy central zone, and a decomposition of ionizing sources for the emission lines).

Galaxies falling below the main sequence of star formation have different emission line ratios to those on it, manifest by a high frequency of a diagnosis of non starforming spaxels. The central NSF galaxies are defined as having <60 percent central (over 0-0.5 R_e) spaxels that are star forming, and some have a rising radial profile of **Hα luminosity** over 0-0.5 R_e (Figure 4.5, right panel). Central NSF galaxies are mostly located below the MS ridgeline in the SFR-M* plane, while galaxies with a rising profile of star formation surface density may be found both above and below the main sequence ridgeline. It is possible the overall lower star formation in the Below-MS group may lead to unmasking of the non-starforming diagnostic ratios, although there is little published evidence for this.

5.3 Bulge-to-total Flux Ratio

The bulge-to-total flux ratio (B/T) is available for analysis in most SAMI galaxies due to collaboration with the GAMA Survey II (Kennedy et al. 2016), as discussed in Subsection 2.6.2. The importance of bulge growth in quenching is emphasised by many authors (Martig et al. 2009; Genzel et al. 2014; Bluck et al. 2014, 2019; Tacchella et al. 2015), as discussed in Subsection 1.2.3, where bulge-related quenching mechanisms are discussed. Bluck et al. (2019) reported the B/T ratio correlated more closely with the distance from the star forming main sequence, than stellar mass.

The results presented in Section 4.5 confirm that quenched galaxies have bigger bulges than MS galaxies with the Sub-MS group having higher bulge-to-total flux ratio values than the other groups (p value = 0.0003). The Below-MS group also has higher values than the MS group, with the result significant at the p = 0.04 level. There is a positive correlation between the B/T ratio and central radial profile slope, significant at the p = 0.04 level (Figure 4.23). There is no significant difference in the B/T ratio between the rising and falling profile galaxy groups over 0 - 0.5 R_e (p = 0.16) (Figure 4.22).

Many authors consider bulges lead to less efficient star formation and quenching; the growth of central mass concentration in a bulge - whereby the inner disk is converted into a spheroid - is thought to stabilize a gas disk against fragmentation into dense clumps, and subsequent star formation (Crocker et al. 2012; Martig et al. 2013; Tacchella et al. 2015). This view is supported by the finding that quenched galaxies have a larger bulge fraction. This survey distinguishes quenching-in-progress galaxies (called Below-MS) and quenched galaxies (Sub-MS). In Figure 3.7 the Sub-MS group have a highly significant larger bulge fraction (p = 0.0003) than the MS group, unfortunately radial profiles of star formation are not able to be constructed in this group in this study.

Pan et al. (2013) find evidence of bulge components in about 90 percent of green valley disk galaxies. Galaxies with a prominent bulge represent about 60 - 70 percent in the green valley disk sample, and only ~35 percent in the blue cloud disk sample. These authors conclude the presence of bulge in the majority of green valley galaxies suggests that star formation quenching in this population possibly accompanies or is connected with bulge formation. Pan et al. (2013) use different methodologies both for identification of quenching-in-progress (green valley) galaxies, namely NUV-r color, and for bulge fraction; to measure bulges they employ a bulgeness parameter B_{ZEST} in the ZEST morphological classification whereby disk galaxies are placed in four bins and the authors state this roughly correlates with the bulge-to-disk ratio.

Galaxies with small bulges may temporarily have a dip in total SF and fall below the MS, but may recover their place on the MS if gas supply allows, and only the large-bulge galaxies become permanently quenched (Fang et al. 2013). These authors use the inner stellar mass surface density within a radius of 1 kpc to quantify the growth of the bulge, and note galaxies with bulges may rejuvenate, up to a bulge size limit. Several authors discuss a rejuvenation pathway, whereby green valley galaxies may be red galaxies in which SF has been reignited (Fang et al. 2013; Pan et al. 2013), and the quenching models such as compaction and bar-driven quenching involve a cycle of central suppression followed by nuclear starbursts. To rejuvenate, red galaxies might obtain gas supply either from gas-rich minor mergers or from gradual accretion, then start low level star formation activity and return to the green valley. They might move to the red sequence again after the gas is exhausted.

While galaxies moving off the MS do have bigger bulges, this thesis provides little evidence that enlarging bulges initiate the quenching process. Large bulges are only found in the quenched Sub-MS galaxies at high masses. In morphological quenching the steep potential well gives the bulge a Toomre Q parameter above unity and stabilizes gas in the bulge against star formation (Martig et al. 2009). Morphological quenching predicts cold gas in early-type galaxies to be comparable to gas fractions in normal star-forming galaxies; however Cheung et al. (2012) review multiple studies to show the absolute gas content of early-type galaxies is low compared to starforming galaxies. They find that in order to achieve quenching, it is necessary to reduce the fractional gas content, by either expelling gas or preventing new gas from falling in, neither of which are achieved with morphological quenching.

Other authors have challenged the importance of a bulge in quenching (Fabello et al. 2011; Catinella et al. 2010). Fabello et al. (2011) find no evidence that galaxies with a significant bulge component are less efficient at turning their available gas reservoirs into stars, in a HI stacking analysis that estimates the average HI gas fractions M_{HI}/M_{*} in 1833 SDSS early-type galaxies. They find the HI content of a galaxy is not influenced by its bulge. Catinella et al. (2010) report the atomic gas fraction M_{HI}/M_{*} decreases strongly with stellar mass, stellar surface mass density and NUV - r colour, but is only weakly correlated with the galaxy bulge-to-disc ratio.

In the present study the finding that the B/T ratio did not significantly differ between the rising and falling profile galaxy groups over 0 - 0.5 R_e may indicate (a) either the reduced SF efficiency expected with bulge growth has not had a notable effect on the distribution/radial profiles of star formation; or (b) there may be increased gas concentration in the galaxy centre that compensates for the reduced efficiency.

5.4 Environmental Surface Density

This thesis uses environmental surface density as an index of environmental density from the SAMI-GAMA Environment-Measures catalogue, as discussed in Subsection 2.6.3. No association of environmental surface density with a rising central profile is found. This is expected given the low environmental density associated with the sample.

However in dense environments an association of more centrally concentrated star formation (associated with falling radial profiles of star formation from the centre moving outwards) is reported, consistent with the outside-in quenching of star formation (Schaefer et al. 2017; Finn et al. 2018). Environmental factors may play a role in galaxy evolution and quenching in dense environments, by preventing gas from reaching galaxies or by removing gas reservoirs, as discussed in Section 1.2.10. The mechanisms include ram pressure stripping, strangulation and harassment (Bekki, Couch & Shioya 2002; Fujita 2004; Kawata & Mulchaey 2008; Peng, Maiolino & Cochrane 2015; Schaefer et al. 2019). Main-sequence galaxies located in groups or clusters have the specific star formation rate (sSFR) lower by 0.1 - 0.3 dex when compared to that of field galaxies (Lin et al. 2019). Further the fraction of star-forming galaxies tends to decrease with increasing environmental density, even at fixed stellar mass (Peng et al. 2010; Finn et al. 2018). However Lin et al. (2019) report that both inside-out and outside-in quenching coexist in both dense and less-dense environments and that inside-out quenching dominates in the more massive halos, even in dense environments.

5.5 Hα as a Star Formation Indicator in AGN/LINERS

In Section 2.5 it is noted the nebular Hα recombination line is a widely used tracer of recent star formation, and in SAMI galaxy studies the estimation of the SFR of a galaxy is generally based on its Hα emission. This section examines the limitations and possible errors resulting from the use of Hα as a star formation indicator in AGN/LINERS. Studies of the distribution of SF that interpret Hα as star formation may give misleading results in certain locations and galaxies such as the centres of massive galaxies (Madau & Dickinson 2014, p.434). Regions of galaxies with extended Hα emission with EW$_{H\alpha}$ < 3 are consistent with photoionization by old stars (Cid Fernandes et al. 2011; Delgado et al. 2016). Galaxies on the red sequence display line emission with line ratios generally inconsistent with those expected from star formation; their spectra are characterized by strong low-ionization transitions (e.g. [OI] λ6300, [SII] $\lambda\lambda$6717,31) and display the characteristic line ratios of low-ionization nuclear emission-line regions (LINERs) (Belfiore et al. 2016). LINER-like emission may be extended on kpc scales and is not confined to nuclear regions in galaxies especially in early-type galaxies; the extended LINER-like emission is consistent with photoionization by hot evolved stars such as post-asymptotic giant branch stars (pAGB). Belfiore et al. (2016) note stellar population models demonstrate that pAGB stars are the main source of the ionizing photon background in galaxies once star formation has ceased, and EW$_{H\alpha}$ of 0.5 - 2.0 can be generated by the pAGB stellar component (Belfiore et al. 2016).

Does the presence of an AGN or LINER invalidate the use of Hα flux to measure star formation in the central regions of galaxies where there are many non-starforming spaxels? If a proportion or even all of the central Hα emission is not derived from massive young stars, then the Hα radial profile slope may be artificially lowered (falling more steeply from galaxy centre moving outwards).

The problem of how to distinguish the emission lines powered by the central engine from those powered by hot young stars in the host galaxy is addressed by several authors (Ho et al. 1997; Tommasin et al. 2008; Theios et al. 2016). Observed H_α flux (and the $EW_{H\alpha}$) in the central area of a galaxy may be related to ionizing radiation from an AGN accretion disk or from old stellar populations and post-AGB stars. Theios et al. (2016) uses narrowband interference filter imaging of a representative sample of Seyfert galaxies (in which the nonstellar nuclear emission does NOT strongly dominate over the host galaxy) to separate quantitatively the emission lines powered by black hole accretion in their centers from those powered by young star throughout the host galaxies. They find a correlation between the nuclear Hα luminosity and the Hα luminosity of the host galaxy, and there is an absence of galaxies with high nuclear luminosity and low star formation rates. They conclude there is a correlation between AGN activity and star formation. Similarly in a study of circumnuclear SF regions versus the bolometric luminosities of AGN, Ruschel-Dutra et al. (2017) show a correlation between AGN activity and circumnuclear star formation; they report galaxies are not found where there is strong central emission from an AGN, but no circumnuclear starbursts; that is, they report no examples of AGN with $L_{SB} << L_{AGN}$. Such a AGN-central starburst connection means an AGN is unlikely to produce central H_α emission where there is no SF, however if central SF is present the AGN may inflate the amount. There are theoretical predictions for an AGN-central starburst connection (Kawakatu & Wada 2008; Neistein & Netzer 2014), and star formation luminosities are correlated with the bolometric luminosity of AGN for galaxies with $L_{AGN} \geq 10^{42}$ erg s^{-1}.

Theios et al. (2016) similarly raise this issue: in galaxies with an AGN, nuclear fluxes within 2.9 arcsec should be dominated by the AGN, because integrated spectra of the central region usually show emission line ratios indicative of nonstellar photoionization. In less luminous AGN, these line ratio diagnostics indicate ‘composite’ spectra comprising mixes of AGN and H II region lines. Some of the nuclear Hα fluxes therefore may include a contribution from H II regions in and around the galactic nucleus.

The possibility that AGN contribute to the Hα emission and thereby falsely inflate SFR estimates at the galaxy centre cannot be fully ruled out but the error of overlooking inside-out quenching due to masking of central quenching seems unlikely in the presence of a correlation between AGN activity and circumnuclear star formation.

Davies et al. (2014) analyse the relationship between star formation and AGN activity as a function of radius. Optical IFU data from the CALIFA survey is studied in four AGN host galaxies. Spaxels in each galaxy are colour-coded by the distance of the spaxels along the starburst-AGN mixing sequence on the [N II]/Hα versus [OIII]/Hβ diagnostic diagram. These authors report clear rings of gas ionized with decreasing contributions from the AGN as radius increases. The fractional contribution of the star formation and the AGN activity to the line emission of each spaxel in each galaxy has been calculated, by a numerical calibration of the starburst-AGN mixing sequences. Models of the theoretical starburst-AGN mixing lines are adopted that use weighted combinations of HII region and AGN NLR nebular emission spectra. Star formation and the AGN are each responsible for at least 25 percent of the global Hα, [OII] and [OIII] luminosities in all galaxies which indicates there is a need to correct for any AGN contribution when calculating SFRs using Hα or [OII]. These authors note current and future IFU surveys both locally and at high redshift are increasingly providing statistically significant samples of IFU data to investigate the relationship between star formation and AGN activity across cosmic time, and propose their techniques and models are a 'first stepping stone' to understanding how black holes and host galaxies evolve.

Comparisons of the radial profile of SF when measured by Hα based methods and UV-based methods have shown agreement between the methods irrespective of the presence of an AGN. In 10 galaxies at z ~2 on the SF Main Sequence (displayed above, Figure 5.2), Tacchella et al. (2018) find close agreement in radial profiles of sSFR and SFR between Hα-based methods and UV-based methods, and also show obscuration by dust is not responsible for the low sSFR at the centre of some galaxies. Catalan-Torrecilla et al. (2015) obtain integrated Hα, ultraviolet (UV) and infrared (IR)-based SFR measurements for 272 galaxies from the CALIFA survey using single-band and hybrid tracers. These authors show that in local galaxies the extinction-corrected Hα luminosity agrees with the hybrid SFR estimators based on either UV or Hα plus IR luminosity, whether AGN are present or not and conclude the extinction-corrected Hα luminosity derived from IFS observations can be used to measure SFR.

Nelson et al. (2016) consider whether there can be gradients in the SFR/Hα ratio that are produced in four ways: dust, AGNs, winds, and metallicity, and which have opposing effects. Dust will increase the SFR/Hα ratio by obscuring the ionizing photons from star-forming regions. AGNs, winds, and higher metallicity will reduce the SFR/Hα ratio, as they add ionizing photons that do not trace star formation. These authors conclude one may be 'relatively confident' interpreting Hα as star formation at low masses, low SFRs, and for radial profiles outside of the center; but may be 'less confident' for the centers of the radial profiles of massive or highly star-forming galaxies.

Two further studies that compare measurements of SFR based on Hα emission to measurements using other methods conclude the extinction-corrected Hα luminosity closely correlates with alternative methods based on for example a FUV+22 μm hybrid tracer (Catalan-Torrecilla et al. 2015; Tacchella et al. 2017).

5.6 Conclusions and Future Work

Integral field spectroscopy allows the construction of radial profiles of star formation in the disks of star forming galaxies. The profiles are here used in the testing of various mechanisms that have been proposed for galaxy quenching and evolution. A goal was to determine whether processes local to each galaxy (such as a central process) or global environmental factors such as strangulation are the prime drivers of quenching.

A sample of star forming galaxies from the SAMI Galaxy Survey are used, noting that only galaxies with a majority of spaxels in the central area that are star forming are suitable for construction of a radial profile. Galaxies have been classified as main sequence, Above-, and Below- main sequence based on their location in relation to the star formation main sequence ridgeline.

The radial profiles of star formation in the 3 groups demonstrate coherent star formation (discussed in Section 1.2.4), and it is argued this is consistent with several proposed quenching mechanisms including strangulation or cosmic web detachment. This study has been unable to distinguish between quenching from the inside out such as the 'compaction' scenario, and strangulation as a primary quenching mechanism. While most galaxies display coherent star formation, a substantial minority (16-20%) of galaxies show evidence of a positive central gradient (or 'rising' central radial profile)and may be assumed to have central suppression of star formation.

Rising central radial profiles of star formation are considered an indicator of central suppression of star formation and some authors link them to inside-out quenching. That central suppression may occur in Above-MS and MS galaxies is consistent with a theory of cyclic central star formation (Section 1.1.7). The evidence linking rising central radial profiles to quenching in this study is weak (as discussed in Section 5.2), because only a small non-representative fraction of the Below-MS galaxies are able to have a radial profile measured.

A weak positive correlation between increasing bulge size and central radial profile slope has been detected; the Below-MS group has larger bulges than the MS group, significant only at the p = 0.04 level. The finding that the bulge/total flux ratio did not significantly differ between the rising and falling profile galaxy groups over 0 - 0.5 R_e does not support a major role of bulges in the initiation of central suppression of star formation.

5.6.1 Future Work

The finding that some galaxies on, above and below the main sequence have rising central radial profiles of star formation requires further confirmation. More galaxies are becoming available for study both in the SAMI Galaxy Survey and other integral field spectroscopy surveys. A larger sample of galaxies will permit a better estimate of the proportion of starforming galaxies with central suppression, that can assist in testing evolutionary theories such as cyclic central star formation. It will be important to study the central area at high resolution in galaxies with a rising profile, with a telescope such as ESO MUSE [1] to ensure radial profiles of star formation in a representative sample of below main sequence galaxies are obtained.

A goal of this study was to determine whether processes within each galaxy (such as a central process) or global environmental factors such as the lack of access to external gas accretion are the prime drivers of quenching. There is growing evidence that both occur, but the global process dominates the main observed effect of e.g. evolution on the SFR-M plane. A recent analysis by Bluck et al. (2020) of 3500 local galaxies with SDSS-IV MaNGA-DR15 finds that quenching is ‘fundamentally a global process’ but that star formation is governed locally by processes within each galaxy and region of the galaxy. Even in galaxies in a dense environment with evidence of outside-in quenching, there may be a concurrent inside-out quenching process occurring (Lin et al. 2019).

[1]ESO MUSE is the Multi Unit Spectroscopic Explorer (MUSE), a high-resolution integral-field spectrograph for the Very Large Telescope (VLT) of the European Southern Observatory (ESO).

Simulations continue to drive interest in radial profiles of star formation. Using samples from the Illustris and EAGLE large cosmological simulations, Starkenberg et al. (2019) find centrally concentrated star formation for galaxies in the Green Valley at all galaxy stellar masses and therefore suggest that quenching occurs from the outside-in. These authors identify "a fundamental mis-match" between their radial sSFR profiles of galaxies in the Illustris and EAGLE simulations, and the observations of Belfiore et al. (2018). This mismatch creates an opportunity in future work for a collaborative effort to reconcile observations and simulations of radial profiles.

The role of bulges in quenching remains unresolved. A study of the radial profile of gas concentration in SAMI galaxies is in progress, that may allow a future assessment of star formation efficiency in galaxies with various bulge fractions, and a direct test of the morphological quenching model.

Chapter 6

REFERENCES

Abazajian K.N et al., 2003, AJ, 126, 2081

Abazajian K.N. et al., 2009, ApJS, 182, 543

Aghanim N. et al., Planck Collaboration, 2018, Preprint (arXiv:1807.06209v2)

Akeson R. et al, 2019, Preprint (arXiv:1902.05569)

Alam S., Zu Y., Peacock J. A., Mandelbaum R., 2019, MNRAS, 483, 4501

Alatalo K. et al., 2011, ApJ, 735, 88

Allen J.T. et al., 2015, MNRAS, 446, 1567

Alpaslan M. et al., 2016, MNRAS, 457, 2287

Aragon-Calvo M.A., Szalay A.S., 2013, MNRAS, 428, 3409

Aragon-Calvo M.A., Neyrinck M.C., Silk J., 2019, The Open Journal of Astrophysics, 2019, vol. 2, issue 1, id. 7. Preprint (arXiv:1607.07881v3)

Bacon R. et al., 2001, MNRAS, 326, 23

Baldry I.K, Glazebrook K., Brinkmann J., Ivezic Z., Lupton R.H., Nichol R.C., Szalay A.S., 2004, ApJ, 600, 681

Baldwin J. A., Phillips M. M., Terlevich R., 1981, PASP, 93, 5

Behroozi P., Silk J., 2018, MNRAS, 477, 5382

Bekki K., Couch W.J., Shioya Y., 2002, ApJ, 577,651

Belfiore F. et al., 2016, MNRAS, 461, 3111

Belfiore F. et al., 2017a, MNRAS, 466, 2570

Belfiore F. et al., 2017b, MNRAS, 469, 151

Belfiore F. et al., 2018, 477, 3014

Bell E. F. et al., 2004, ApJ, 608, 752

Bell E.F. et al., 2012, ApJ, 753, 167

Bianconi M., Marleau F.R., Fadda D., 2016, A&A, 588, A105

Birnboim Y., Dekel A., 2003, MNRAS, 345, 349

Birnboim Y., Dekel A., Neistein E., 2007, MNRAS, 380, 339

Blanton M. R., 2006, ApJ, 648, 268

Bloom J. et al., 2017, MNRAS, 465, 123

Bluck A.F.L., Mendel J.T., Ellison S.L., Moreno J., Simard L., Patton D.R., Starkenburg E., 2014, MNRAS, 441,599

Bluck A. F. L. et al., 2019, MNRAS, 485, 666

Bluck A.F.L., Maiolino R., Sanchez S.F., Ellison S.L.,Thorp M.D., Piotrowska J.M., Teimoorinia H., Bundy K.A., 2020, MNRAS, 492, 96

Bond J. R., Kofman L., Pogosyan D., 1996, Nature, 380, 603

Bower R.G., McCarthy I.G., Benson A.J., 2008, MNRAS, 390, 1399

Brennan R. et al., 2015, MNRAS, 451, 2933

Brennan R. et al., 2017, MNRAS, 465, 619

Brinchmann, J., Charlot, S., White, S. D. M., et al. 2004, MNRAS, 351, 1151

Brook C.B., Kawata D., Martel H., Gibson B.K., Bailin J., 2006, ApJ, 639, 126

Brough S. et al., 2017, ApJ, 844, 59

Bruzual G. A., Charlot S., 1993, ApJ, 405, 538

Bryant J.J. et al., 2015, MNRAS, 447, 2857

Bundy K., et al., 2015, ApJ, 798, 7

Calzetti D., 2001, PASP, 113, 1449

Caon N., Capaccioli M., D'Onofrio M., 1993, MNRAS, 265,1013

Cappellari M., Copin Y., 2003, MNRAS, 342, 345

Cappellari M., Emsellem E., 2004, PASP, 116, 138

Cappellari, M. et al., 2011, MNRAS, 413, 813

Cappellari M. et al., 2013, MNRAS, 432, 1862

Cardelli J. A., Clayton G. C., Mathis J. S., 1989, ApJ, 345, 245

Catalan-Torrecilla C. et al., 2015, A&A, 584, A87

Catalan-Torrecilla C. et al., 2017, ApJ, 848, 87

Catinella B. et al., 2010, MNRAS, 403, 683

Cattaneo A. et al., 2009, Nature, 460, 213

Cautun C., van de Waygaert R., Jones B.J.T, Frenk C.S., 2014, MNRAS, 441, 2923

Cecil G. et al., 2016, MNRAS, 456, 1299

Chabrier G., 2003, PASP, 115, 763

Chang C. et al., 2019, MNRAS 482, 3696

Cheung E. et al., 2016, Nature, 533, 504

Cheung E. et al., 2012, ApJ, 760,131

Churchill C.W., Kacprzak G.G., Steidel C.C., Spitler L.R., Holtzman J., Neilsen N.M., Trujillo-Gomez S., 2012, ApJ, 760, 68

Cicone C. et al., 2014, A&A, 562, A21

Cid Fernandes, R., Stasinska, G., Mateus, A., Vale Asari, N. 2011, MNRAS, 413, 1687

Ciotti L., 1991, A&A, 249, 99 Colless M. et al., 2001, MNRAS, 328, 1039

Cortese L. et al., 2014, ApJL, 795, L37

Cortese L. et al., 2016, MNRAS, 463, 170

Crocker A. et al., 2012, MNRAS, 421,1298

Croom S.M. et al., 2012, MNRAS 421, 872

Croton D.J. et al., 2006, MNRAS, 365, 11

Daddi, E., Dickinson, M., Morrison, G., et al. 2007, ApJ, 670, 156

Darvish B., Sobral D., Mobasher B.. Scoville N.Z., Best P., Sales L.V., Smail I., 2014, ApJ, 796, 51

Davies R.L., Kewley L.J., Ho I.-T., Dopita M.A., 2014, MNRAS, 444, 3961

Davies L.J.M. et al., 2016, MNRAS, 455, 4013

Davis M. et al., 2007, ApJL, 660, L1

Dekel A., & Burkert A., 2014, MNRAS, 438, 1870

Del Popolo A., Le Delliou M., 2017, Galaxies, 2017, 5, 17

Delgado R.M. et al., 2016, A&A, 590, A44 (2016)

Dressler A., 1980, ApJ, 236, 351

Driver S.P., Norberg P., Baldry I. K., Bamford S. P., Hopkins A. M., Liske J., Loveday J., Peacock J.A., 2009, A&G, 50, 5.12

Driver S.P. et al., 2011, MNRAS, 413, 971

Elbaz, D., Daddi, E., le Borgne, D., et al. 2007, A&A, 468, 33

Ellis R.S., 2008, in: First Light in the Universe, Saas-Fee Advanced Course 36, Swiss Society for Astrophysics and Astronomy Eds D. Schaerer, A. Hempel and D. Puy, Springer, Berlin

Ellison S.L., Sanchez S.F., Ibarra-Medel H., Antonio B., Mendel J.T., Barrera-Ballesteros J., 2018, MNRAS, 474, 2039

Elmegreen D.M., Elmegreen B.G., Ravindranath S., Coe D.A., 2007, ApJ, 658, 763

Fabello S., Catinella B., Giovanelli R., Kauffmann G., Haynes M.P., Heckman T,M., Schiminovich D., 2011, MNRAS, 411, 993

Faber S.M. et al., 2007, ApJ, 665, 265

Fang J.J., Faber S.M., Koo D.C., Dekel A., 2013, ApJ, 776, 63

Ferrarese L., Merritt D.A., 2000, ApJ, 539, 9

Finn R.A. et al., 2018, ApJ, 862, 149

Fogarty L.M.R., Scott N., Owers M.S., 2015, MNRAS, 454, 2050

Forster Schreiber N.M. et al., 2014, ApJ, 787, 38

Fujita Y., 2004, PASJ, 56, 29

Furlong M. et al., 2015, MNRAS, 450, 4486

Gabor J.M., Dave R., Finlator K., Oppenheimer B.D., 2010, MNRAS, 407, 749

Gadotti D.A., 2009, MNRAS, 393, 1531

Garrison-Kimmel S., Boylan-Kolchin M., Bullock J.S., Kirby E.N., 2014, MNRAS, 444, 222

Gavazzi G. et al., 2015, A&A, 580, A116

Gawiser E., Silk J., 2000, Phys.Rept., 333. 245

Geha M., Blanton M.R., Masjedi M., West A.A., 2006, ApJ, 653, 240

Geha M., Blanton M.R., Yan R., Tinker J.L., 2012, ApJ, 757:85

Genzel R., Eisenhauer F., Gillssen S., 2010, RvMP, 82, 3121

Genzel R. et al., 2011, ApJ, 733, 101

Genzel R. et al., 2014, ApJ, 785, 75

Goddard D. et al., 2017, MNRAS, 466, 4731

Gonzalez Delgado R.M. et al., 2016, A&A, 590, A44

Governato F. et al., 2010, Nature, 463, 203

Governato F. et al., 2012, MNRAS, 422, 1231

Graham A.W., Worley C.C., 2008, MNRAS, 388,1708

Green A. et al., 2018, MNRAS, 475, 716

Gunawardhana M.L.P. et al., 2011, MNRAS, 415, 1647

Gunn J.E., Gott J.R., 1972, ApJ, 176, 1

Guo Y. et al., 2012, ApJ, 757,120

Guo Y. et al., 2015, ApJ, 800, 39

Guth A.H., 1981, Phys Rev, D 23, 347

Ho I.-T. et al., 2014, MNRAS, 444, 3894

Ho I.-T. et al., 2016a, Astrophy Space Sci, 2016a, 361,280

Ho I.-T. et al., 2016b, MNRAS, 457,1257

Ho L.C., 2008, ARAA, 46, 475

Holden, B. P., van der Wel, A., Rix, H.-W., Franx, M. 2012, ApJ, 749, 96

Hopkins A.M. et al. 2013, MNRAS, 430, 2047

Hubble E. P., 1926, ApJ, 64, 321

Ivezic Z. et al, 2019, ApJ, 873, 111

Ishibashi W., Fabian A.C., 2012, MNRAS, 427, 2998

Ishibashi W., Auger M.W., Zhang D., Fabian A.C., 2014, MNRAS, 443, 1339

Jahnke K., Maccio A. V., 2011, ApJ, 734, 92

Kauffmann G. et al., 2003a, MNRAS, 341, 54

Kauffmann G. et al., 2003b, MNRAS, 346, 1055

Kawakatu N., Wada K., 2008, ApJ, 681, 73

Kawata D., Mulchaey J.S., 2007, ApJ, 672, L103

Kawata D. et al., 2014, MNRAS, 438, 1208

Kelvin L.S. et al., 2012, MNRAS, 421, 1007

Kelvin L.S. et al., 2014, MNRAS, 439, 1245

Kennedy R. et al., 2016, MNRAS, 460, 3458

Kennicutt R. C. Jr., 1989, ApJ, 344, 685

Kennicutt R. C. Jr., 1998, ARA&A, 36, 189

Kennicutt R. C. Jr., Evans N.J., 2012, Annu. Rev. Astron. Astrophys., 50, 531

Kerr F.J., Lynden-Bell D., 1986, MNRAS, 221, 1023

Kewley L. J., Dopita M. A., Sutherland R. S., Heisler C. A.,Trevena J., 2001, ApJ, 556, 121

Kewley L. J., Groves B., Kauffmann G.,, Heckman T., 2006, MNRAS, 372, 961

Khochfar S. et al., 2011, MNRAS, 417,845

Kim K., Oh S., Jeong H., Aragon-Salamanca A., Smith R., and Yi S.K., 2016, ApJS, 225, 6

Knabenhans M. et al., 2019, MNRAS, 484, 5509

Kormendy J., 2013, In Secular Evolution of Galaxies, XXIII Canary Islands Winter School of Astrophysics, ed. J. Falcon-Barroso & J.H. Knapen, Cambridge: Cambridge Univ. Press, p. 1. Preprint (arXiv:1311.2609v1)

Kraljic K. et al., 2018, MNRAS, 474, 547

Krumholz M. R., Kruijssen J. M. D., Crocker R. M., 2017, MNRAS, 466, 1213

Lanfranchi G.A., Matteucci F., 2007, A&A, 468(3), 927

Lang, P. et al., 2014, ApJ, 788, 11

Lange R. et al, 2016, arXiv, 1607.01096v1

Lara-Lopez M.A. et al., 2013, MNRAS, 434, 451

Le Fevre O. et al., 2005, A&A, 439, 845

Li C. et al., 2015, ApJ, 804, 125

Libeskind N.I., Knebe A., Hoffman Y., Gottlober S., Yepes G., 2011, MNRAS, 418, 336

Libeskind N.I. et al., 2018, MNRAS, 473, 1195

Lin L. et al., 2017, ApJ, 851, 18

Lin L. et al., 2019, ApJ, 872:50

Lisenfeld U., Ferrara A., 1998, ApJ, 496, 145

Liske J. et al., 2015, MNRAS, 452, 2087

Loveday J. et al., 2015, MNRAS, 451, 1540

Lovell M.R., Eke V., Frenk C.S., 2012, MNRAS, 420, 2318

Maier C. et al., 2016, A&A, 590, A108

McElroy R., Croom S.M., Pracy M., Sharp R., Ho I.T., Medling A. M., 2015, MNRAS, 446, 2186

McGaugh S.S., Schombert J.M., de Blok W.J.G., Zagursky M.J., 2010, AJ, 708, L14

McIntosh D.H. et al., 2014, MNRAS, 442, 533

McKinnon R., Torrey P., Vogelsberger M., 2016, 457, 3775

McNamara B.R. et al., 2014, ApJ, 785, 44

McNamara B.R., Russell H.R., Nulsen P.E.J., Hogan M.T., Fabian A.C., Pulido F., Edge A.C., 2016, ApJ, 830, 79

Madau P., Dickinson M., 2014, ARA&A, 52, 415

Mahajan S., et al., 2015, MNRAS, 446, 2967

Mahoro A., Povic M., Nkundabakura P., 2017, MNRAS, 471,3226

Markwardt C. B., 2009, in Bohlender D. A., Durand D., Dowler P., eds, ASP Conf. Ser. Vol. 411, Astronomical Data Analysis Software and Systems XVIII. Astron. Soc. Pac., San Francisco, p. 251

Martig M., Bournaud F., Teyssier R., Dekel A., 2009, ApJ, 707, 250

Martig M. et al., 2013, MNRAS, 432,1914

Mashchenko S., Couchman H.M.P., Wadsley J., 2006, Nature, 442, 539

Mayer L. et al., 2001, ApJ, 559,754

Mayer L., Kazantzidis S., Mastropietro C. Wadsley J., 2007, Nature, 445, 738

Medling A. et al., 2018, MNRAS, 475, 5194

Mendel J. T., Simard L., Ellison S. L., Patton D. R., 2013, MNRAS, 429, 2212

Metuki O., Libeskind N.I., Hoffman Y., Crain R.A., Theuns T., 2015, MNRAS, 446, 1458

Moffett A.J et al., 2019, MNRAS, 489, 2830

Mosleh M., Tacchella S., Renzini A., Carollo C.M., Molaeinezhad A., Onodera M., Khosroshahi H.G., Lilly S., 2017, ApJ, 837, 2

Munoz-Mateos J.C., Gil de Paz A., Boissier S., Zamorano J., Jarrett T., Gallego J., B. F. Madore B.F., 2007, ApJ, 658, 1006

Navarro J.F., 2018, Dwarf Galaxies: from the Deep Universe to the Present Proceedings IAU Symposium No. 344, 2018; preprint (arXiv:1809.07431v2)

Neistein E., Netzer H., 2014, MNRAS, 437, 3373

Nelson E. J. et al., 2016, ApJ, 828, 27

Noeske K.G. et al., 2007, ApJ, 660, L43

Ogiya G., Burkert A., 2015, MNRAS, 446, 2363

Ogiya G., Mori M., 2014, ApJ, 793, 46

Orr M. E. et al., 2017, ApJL, 849:L2

Osterbrock D.E. & Ferland G.J. 2006, Astrophysics of Gaseous Nebulae and Active Galactic Nuclei (AGN). University Science Books 2006

Owers et al., 2019, ApJ, 873, 52

Pan Z., Kong X., Fan L., 2013, Apj, 776, 14

Papastergis E., Shankar F., 2016, A&A, 591, A58

Papovich C. et al., Astro2020: Decadal Survey on Astronomy and Astrophysics, science white papers, no. 266; Bulletin of the American Astronomical Society, Vol. 51, Issue 3, id. 266. Preprint (arXiv:1903.04524v1)

Pawlowski M.S. et al., 2014, MNRAS, 442, 2362

Pedraz S., Gorgas J., Cardiel N., Sanchez-Blazquez P., Guzman R., 2002, MNRAS, 332, L59

Peeples M.S., Werk J.W, Tumlinson J., 2014, ApJ, 786, 54

Peng Y.-j. et al., 2010, ApJ, 721, 193

Peng Y., Maiolino R., Cochrane R., 2015, Nature, 521, 192

Perez-Montero E. et al., 2013, A&A, 549, A25

Perez-Montero E. et al., 2016, A&A, 595, A62

Pierce C. M. et al., 2010, MNRAS, 408, 139

Pontzen A., Tremmel M., Roth N., Peiris H.V., Saintonge A., Volonteri M., Quinn T., Governato F., 2017, MNRAS, 465, 547

Reiss I., Mushkin J., Keshet U., 2017, preprint (arXiv:1705.05376v3)

Riess A. G., et al., 2016, ApJ,826, 56

Renzini A., Peng Y.-J., 2015, ApJL, 801, L29

Robotham A.S.G., Davies L.J.M., Driver S.P., Koushan S., Taranu D.S., Casura S., Liske J., 2018, MNRAS, 476,3137

Rocha M., Peter A.H.G, Bullock J.S., Kaplinghat M., Garrison-Kimmel S., Onorbe J., Moustakis L.A., 2013, MNRAS, 430, 81

Rodighiero G. et al., 2011, ApJ, 739, L40

Rupke D.S.N., Veilleux S., 2011, ApJL, 729, L27

Ruschel-Dutra D., Espinosa J.M.R., Martin O., Pastoriza M., Riffel R., 2017, MNRAS, 466, 3353

Russell H.R. et al., 2016, MNRAS, 458, 3134

Rys A., Falcon-Barroso J., van de Ven G., in Highlights of Spanish Astrophysics VII, Proceedings of the X Scientific Meeting of the Spanish Astronomical Society held on July 9 - 13, 2012, in Valencia, Spain. J. C. Guirado, L. M. Lara, V. Quilis, and J. Gorgas (eds.). Preprint (arXiv:1210.3592v1)

Saintonge A. et al., 2012, ApJ, 758, 73

Salim S. et al., 2005, ApJ, 619, L39

Salim S. et al., 2007, ApJS, 173, 267

Salmon B. et al., 2015, ApJ, 799, 183

Salpeter E.E., 1955, ApJ, 121,161

Sanchez Almeida, J., Elmegreen B.G., Munoz-Tunon C., Elmegreen D.M., 2014, A&ARv, 22, 71

Sanchez S.F. et al., 2012, A&A, 538, A8

Schaefer A.L. et al., 2017, MNRAS, 464, 121

Schaefer A.L. et al., 2019, MNRAS, 483, 2851

Schaye J. et al., 2015, MNRAS, 446, 521

Scott N. et al., 2018, MNRAS, 481, 2299

Sellwood J.A., 2014, RvMP, 86, 1

Sérsic J. L., 1963, Bol. Asociacion Argentina Astron. La Plata Argentina, 6, 41

Sérsic J. L., 1968, Atlas de Galaxias Australes. Univ. Cordoba, Cordoba

Sharp R. et al., 2015, MNRAS, 446, 1551

Silk J., 2003, MNRAS, 343, 249

Snedden A., Coughlin J., Phillips L.A., Mathews G., Suh I., 2016, MNRAS, 455, 2804

Sobral, D., Best, P.N., Smail, I. Geach J.E., Cirasuolo M., Garn T., Dalton G.B., 2011, MNRAS, 411, 675

Sormani M.C., Barnes A.T., 2019, MNRAS, 484, 1213

Speagle J.S., Steinhardt C.L., Capak P.L., Silverman J.D., 2014, ApJS, 214, 15

Spindler A., et al., 2018, MNRAS, 476, 580

Spinoso D., Bonoli S., Dotti M., Mayer L., Madau P., Bellovary J., 2017, MNRAS, 465, 3729

Springel V., Frenk C.S., White S.D.M, 2006, Nature, 440, 1137

Sturm E. et al., 2011, ApJL, 733, L16

Tacchella S. et al., 2015, Science, issue 6232, 348, 314

Tacchella S. et al., 2016, MNRAS 457, 2790

Tacchella S. et al., 2018, ApJ, 859, 56

Taylor E.N et al., 2011, MNRAS, 418, 1587

Taylor E.N. et al., 2015, MNRAS, 446, 2144

Taylor P., Kobayashi C., 2016, MNRAS, 463, 2465

Taylor P., Kobayashi C., 2017, MNRAS, 471, 3856

Teyssier R. et al., 2013, MNRAS, 429, 3068

Theios R.L., Malkan M.A., Ross N.R., 2016, ApJ, 822, 45

Thorp M.D., Ellison S.L , Simard L., Sanchez S.F., Antonio B., 2019, MNRAS, 482, L55

Tombesi F., Sambruna R.M., Reeves J.N., Braito V., Ballo L., Gofford J., Cappi M., Mushotzky R.F., 2010a, ApJ, 719, 700

Tombesi F., Cappi M., Reeves J.N., Palumbo G.G.C., Yaqoob T., Braito V., Dadina M., 2010b, A&A, 521, A57

Tombesi F., Melendez M., Veilleux S., Reeves J.N., Gonzalez-Alfonso E., Reynolds C.S., 2015, Nature, 519, 436

Tomczak A.R. et al., 2014, ApJ, 783, 85

Tonry J. L., Blakeslee J. P., Ajhar E. A., Dressler A., 2000, ApJ, 530, 625

Treister E. et al., 2009, ApJ, 693, 1713

Tremonti C.A. et al., 2004, ApJ, 613, 898

Trujillo I., Graham A.W., Caon N., 2001, MNRAS, 326, 869

Trujillo-Gomez S., Klypin A., Colin P., Ceverino D., Arraki K.S., Primack J., 2015, MNRAS, 446, 1140

Vandenbroucke B., Verbeke R., De Rijcke S., 2016, MNRAS, 458, 9123

van Dokkum, P.G. et al., 2014, ApJ, 791, 45

van de Sande J. et al., 2017, ApJ, 835, 104

van den Bosch et al., 2008, MNRAS, 387, 79

van der Wel, A. et al. 2014, ApJ, 792, L6

van Zee L., Skillman E.D., Haynes M.P., 2004, AJ, 128, 121

Vogelsberger M., Zavala J., Simpson C., Jenkins A., 2014, MNRAS, 444, 3684

Wake D.A., van Dokkum P.G., Franx M., 2012, ApJL, 751, L44

Weinberg D.H., Bullock J.S., Governato F., de Naray R.K., Peter A.H.G., 2015, PNAS, 112, 12249

Weinmann S.M., Kauffmann G., van den Bosch F.C., 2009, MNRAS, 394, 1213

Weisz D.R. et al., 2011, ApJ, 739, 5

Weisz D.R. et al., 2012, ApJ, 744, 44

Werner N. et al., 2014, MNRAS, 439, 2291

Wetzel A.R., Hopkins P.F., Kim J-H., Faucher-Giguere C., Keres D., Quataert E., 2016, Apj, 827, L23

Whitaker, K. E. et al., 2011, ApJ, 735, 86

Whitaker K. E. et al., 2014, ApJ, 795, 104

White, S.D.M., Frenk, C.S., 1991, ApJ, 379, 52

Worthey G., Ottaviani D. L., 1997, ApJS, 111, 377

Wuyts, S. et al., 2011, ApJ, 742, 96

Wyder T.K. et al., 2007, ApjS, 173, 293

Yniguez B. et al., 2014, MNRAS, 439, 73

York D.G. et al., 2000, AJ, 120, 1579

Zhou et al., 2017, MNRAS,470, 4573

Zolotov A. et al., 2015, MNRAS, 450, 2327

Zubovas K., King A., 2016, MNRAS, 462, 4055

Chapter 7

APPENDIX

7.1 PUBLICATIONS IN ASTROPHYSICS

Gregory Goldstein is listed as co-author in the following publications. He is first author in publication number 9.

1. The SAMI Galaxy Survey: Energy sources of the turbulent velocity dispersion in spatially-resolved local star-forming galaxies. Zhou L. et al., 2017, MNRAS, 470, 4573.

2. The SAMI Galaxy Survey: Spatially Resolving the Main Sequence of Star Formation. Medling A.M. et al., 2018, MNRAS, 475, 5194.

3. The SAMI Galaxy Survey: Mass as the Driver of the Kinematic Morphology - Density Relation in Clusters. Brough S. et al., 2017, ApJ, 844, 59.

4. The SAMI Galaxy Survey: Revisiting Galaxy Classification Through High-Order Stellar Kinematics. van de Sande J. et al., 2017, ApJ, 835, 104.

5. The SAMI Galaxy Survey: Asymmetry in Gas Kinematics and its links to Stellar Mass and Star Formation. Bloom J.V. et al., 2017, MNRAS, 465, 123.

6. The SAMI Galaxy Survey: Spatially resolving the environmental quenching of star formation in GAMA galaxies. Schaefer A.L. et al., 2017, MNRAS, 464, 121.

7. Star-Forming, Rotating Spheroidal Galaxies in the GAMA and SAMI Surveys. Moffett A.J et al., 2019, MNRAS, 489, 2830.

8. High Angular Resolution X-Ray Observations Of The Galactic Supernova Remnant G266.2 1.2 (Rx J0852.0 4622). T. G. Pannuti, J. W. Keohane, G. E. Allen, M. D. Filipovic, M. Stupar, **Gregory Goldstein**. "X-Ray and Radio Connections” (eds. L.O. Sjouwerman and K.K Dyer) Published electronically by NRAO, http://www.aoc.nrao.edu/events/xraydio, Held 3-6 February, 2004 in Santa Fe, New Mexico, USA, (E4.14) 6 pages. Bibliographic Code: 2005xrrc.procE4.14P

9. Variation In Emission And Absorption Lines And Continuum Flux By Orbital Phase In Vela X-1. **Gregory Goldstein**, Huenemoerder, D., Blank, D., 2004, The Astronomical Journal, 127,2310-2321

10. An ATCA radio-continuum study of the Small Magellanic Cloud - I. Source catalogues at 1.42, 2.37, 4.80 and 8.64 GHz. M. D. Filipovic, T. Bohlsen, W. Reid, L. Staveley-Smith, P. A. Jones, K. Nohejl and **Gregory Goldstein**, 2002, MNRAS, 335, 1085-1090.